PALLADIUM AND PLATINUM NANOCRYSTALS: FACILE SYNTHESIS AND THERMAL STABILITY

A Dissertation
Presented to
The Academic Faculty

by

Madeline Vara

In Partial Fulfillment
of the Requirements for the Degree
of Doctor of Philosophy in the
School of Chemistry and Biochemistry

Georgia Institute of Technology

May 2018

PALLADIUM AND PLATINUM NANOCRYSTALS: FACILE SYNTHESIS AND THERMAL STABILITY

Approved by:

Dr. Younan Xia, Advisor
Department of Biomedical Engineering
Georgia Institute of Technology

Dr. Angus P. Wilkinson
School of Chemistry and Biochemistry
Georgia Institute of Technology

Dr. Z. John Zhang
School of Chemistry and Biochemistry
Georgia Institute of Technology

Dr. Ronghu Wu
School of Chemistry and Biochemistry
Georgia Institute of Technology

Dr. Zhiqun Lin
School of Materials Science Engineering
Georgia Institute of Technology

Date Approved: November 27, 2017

Dedicated to my parents, Margaret Rietman and John Vara, for their constant love and support throughout this journey.

ACKNOWLEDGEMENTS

The journey to this final stage in my graduate career could not have been possible without the constant help and support of many others in my life. First and foremost, I would like to deeply thank my graduate advisor, Professor Younan Xia. His guidance and expertise was critical to my development as a scientist and to how I approach chemistry, and I have learned a tremendous amount from him. I would also like to thank Professors Angus Wilkinson, Ronghu Wu, John Zhang, and Zhiqun Lin for serving on my dissertation committee, and for all of their advice and support.

A very special thank you goes to my colleagues and compatriots both current and former, who have helped mentor me, engage me, and challenge me to further develop my own skills. In particular, I would like to thank Xue Wang, Aleksey Ruditskey, Legna Figueroa-Cosme, Kyle D. Gilroy, Zachary D. Hood, and Alyssa Blake for always encouraging me to keep progressing and moving forward, and for reminding me to always keep life in perspective. Additionally, I would to thank Dr. Miaofang Chi, Dr. Jane Howe, Professor Dong Qin, Professor Jiri Janata, and Professor Lawrence Bottomly for guiding and mentoring me at various points during my time here at Georgia Tech. I will always remember the things they have taught me.

Finally, I would like to recognize my family: my sister and brother, Clare and Ned Vara, and my parents, Margaret Rietman and John Vara. Without their constant and unwavering love and support on this journey, I truly do not know where I would be in life. I thank them for always being there for me.

TABLE OF CONTENTS

LIST OF TABLES

Page

LIST OF FIGURES

LIST OF SYMBOLS AND ABBREVIATIONS

A_n	surface area term for the n^{th} crystal facet
AA	ascorbic acid
CV	cyclic voltammogram
DFT	density functional theory
DI	deionized
ECSA	electrochemical surface area
EDX	energy dispersive X-ray
EG	ethylene glycol
FAO	formic acid oxidation
fcc	face-centered cubic
j	the observed current density
JCPDS	joint committee on powder diffraction standards
HAADF	high-angle annular dark-field

HRTEM	high-resolution transmission electron microscopy
ICP-MS	inductively-coupled plasma mass spectrometry
k	rate constant
NaAsc	sodium ascorbate
ORR	oxygen reduction reaction
PEMFC	polymer electrolyte membrane fuel cell
PVP	poly(vinyl pyrrolidone)
RHE	reversible hydrogen electrode
SA	specific activity
STEM	scanning transmission electron microscopy
TEM	transmission electron microscopy
UPD	underpotential deposition
UV-vis	ultraviolet-visible
V_{dep}	rate of atom deposition
V_{dif}	rate of adatom surface diffusion
XRD	X-ray diffraction
ΔG	Gibbs free energy

$\varepsilon_{surface}$	surface free energy
ε_{volume}	volume free energy
γ	specific surface free energy

SUMMARY

Colloidal metal nanocrystals have shown promising potential toward improving vital catalytic reactions needed to sustain modern society. Much of this improved performance from nanocatalysts is derived from the ability to explicitly control the size, shape, composition, and structured of the nanocrystals. This control has in turn been developed from an improved fundamental understanding of the kinetic and thermodynamic parameters that affect colloidal nanocrystal nucleation and growth. The aim of this dissertation is to develop facile and improved techniques for the synthesis of noble-metal nanaocrystals based upon mechanistic insights (with a focus on Pd), and to systematically study the thermal durability of Pt-based nanocatalysts by leveraging the power of *in situ* electron microscopy. I begin by developing a photochemical synthesis conducted at room temperature for the generation of Pd cubes decorated with atomic steps and terraces. In my next study, I demonstrate a room temperature, one-pot synthesis of Pd concave cubes with an average tip-to-tip length of 18 nm by leveraging the room temperature reduction kinetics with an appropriately strong reducing agent. Next, I conduct a systematic study on the thermal stability of Pd@Pt_{4L} nanoscale cubes and octahedra through *in situ* high-resolution electron microscopy, and correlate the results with theoretical calculations. Finally, I carry out a study to investigate the thermal durability of Pt-based nanocages using *in situ* electron microscopy to evaluate their potential use in catalytic applications at elevated temperatures. The insights developed from this dissertation will help to promote rational design of high-performance nanocatalysts, and lay the foundations for predictive evaluation of their use at elevated temperatures.

CHAPTER 1

INTRODUCTION

1.1 Colloidal Metal Nanocrystals

The history of metal nanoparticles can be dated as far back to the ancient Romans, who unknowingly produced Au nanoparticles in glass, such as those in the Lycurgus Cup to create beautiful red and green colors [1]. Similarly, the popular Roman dye "Purple of Cassius" was a mixture of stannic oxide and Au nanoparticles formed by reacting stannic acid with chloroauric acid [2]. During the Middle Ages in Europe, the yellow color in many stained-glass windows was created by Ag nanoparticles present in the glass [3]. Nonetheless, there were no scientific foundations or analytic methods available at those times for people to understand the nanoscale phenomena of what they were creating. It was not until Michael Faraday in 1857 that colloidal nanoparticles were first deliberately and knowingly produced. Faraday readily synthesized spherical Au nanoparticles, calling them divided metals, or colloidal metal salts. Since his groundbreaking work, there has been a dramatic explosion in both fundamental research and the understanding of colloidal nanoparticles, thanks in large part to advances in analytical techniques and theoretical and computational modeling abilities. Interest in nanoparticles has more recently focused on nanocrystals, which are typically defined as nanoparticles with dimensions under 100 nm, and a well-defined lattice structure.

The last few decades in particular have witnessed a tremendous growth in nanocrystal research, applications, and technology. This has been fueled largely by the unique properties and phenomenon exhibited by materials on the nanoscale, which can be considered a bridge between the atomic/molecular scale and the mesoscale. Specifically, materials in the sub-100 nm size regime and approaching molecular size (down to 1 nm) have properties that can differ tremendously from either their bulk or atomic counterparts.

For example, colloidal Au and Ag nanocrystals display a unique optical phenomenon known as surface plasmon resonance, which causes distinct visible light absorption. Colloidal Au nanocrystals in solution such as those synthesized by Faraday are well known for their "wine red" color, while colloidal Ag nanocrystals cause the solution to appear bright gold, both of which are colors associated with neither the respective bulk metals nor the metal salts. Tuning the size and shape of Au or Ag nanocrystals allows the surface plasmon resonance to be tuned as well. These unique shape and size-dependent properties extend beyond optics and to electronic, magnetic, and quantum effects, thus making nanocrystals an exciting and promising new frontier in the research for next-generation materials for a wide variety of applications and devices that go far beyond dyes or glass-staining.

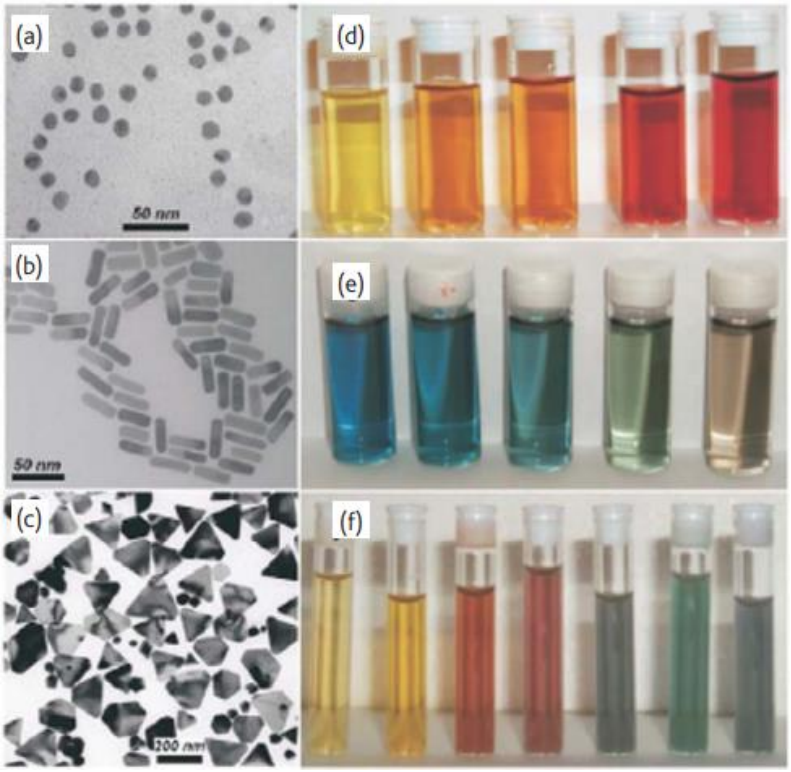

Figure 1.1. TEM images of (a) Au spheres, (b) Au rods, and (c) Ag prisms. On the right, photographs of the colloidal solutions of the metal nanocrystals, with color altered by (d) alloying with Ag or (e, f) changing the size of the nanocrystals. (Reprinted with permission from [29]. Copyright 2007 Elsevier.)

1.1.1 Synthesis of Metal Nanocrystals

The synthesis of colloidal metal nanocrystals has advanced along with an understanding of the factors and variables that direct and control the shape, size, and morphology of the final products. For a typical solution-based synthesis, metal nanocrystals are formed by reducing a metal precursor (usually a salt) in solution with a reducing agent. The process of nanocrystal formation in solution is often simplified by following the classical LaMer model [4, 5]. In this model, a critical supersaturation of metal atoms is needed in the solution. Once this critical level is reached, homogeneous nucleation occurs, generating colloidal metal seeds (referred to as a burst nucleation event). As metal atoms are consumed and the concentration of available precursor drops in the solution below the threshold necessary for nucleation, further nucleation is terminated and the remaining precursor is consumed for the overgrowth of the existing seeds. In addition to the metal precursor and the reducing agent, colloidal stabilizers such as polymers are also typically added to stabilize the resultant nanocrystals in suspension, preventing aggregation from occurring [6].

The synthesis of colloidal nanocrystals relies on two differnt kinetic pathways to control both shape and size: *i*) the nucleation of seeds from solution, which determines the internal structure of the nanocrystal (*e.g.* single-crystal, multiply-twinned, stacking-fault-lined); and *ii*) the overgrowth of seeds into a final structure. Thermodynamic studies on nanocrystal formation have demonstrated a size dependence for the generated structure, with icosahedra being the preferred structure at very small sizes, single crystals the favored structure above certain size thresholds, and decahedra favored in a window between the icosahedra and single crystals [7]. However, in a colloidal synthesis, kinetic factors such as the reducing agent, solvent, and other additives will all impact the reduction rate of metal precursors to metal atoms, which will in turn largely control nucleation and the resultant structures [8]. A recent study demonstrated a rate dependence on the type of seed that is generated in solution [9]. The trend found that very slow reduction and nucleation favors

the formation of crystals with stacking faults. Moderately slow reduction favors the nucleation of multiply-twinned structures such as icosahedra and decahedra. Fast reduction and nucleation favors the formation of single-crystal seeds.

To grow the initial seeds into more complex, non-thermodynamically favored structures, colloidal synthesis must rely on tuning the kinetically controlled parameters for growth. A common kinetic control developed in literature is the use of a facet-selective "capping agent". A capping agent is defined as a molecule that exhibits a strong binding preference onto a particular crystal facet of a given metal, resulting in preferential coverage, or "capping" of that facet during synthesis, and thus limiting the growth in that facet direction due to passivation. For example, bromide has been well established in literature as a {100} facet capping agent for palladium. Thus, a typical strategy to form cubes (a crystal enclosed by {100} facets) is to employ excess bromide in a synthesis. This results in the coverage of {100} facets on the Pd seeds with Br^-, and preferentially growth along the corners in the ⟨111⟩ direction, and thus the formation of cubes [10]. Similar strategies have employed for a variety of different materials and structures, allowing for the controllable synthesis of a myriad of crystal shapes and sizes across a wide platform of metals, such as cubes, octahedra, right bipyramids, decahedra, icosahedra, and plates [6, 10-12].

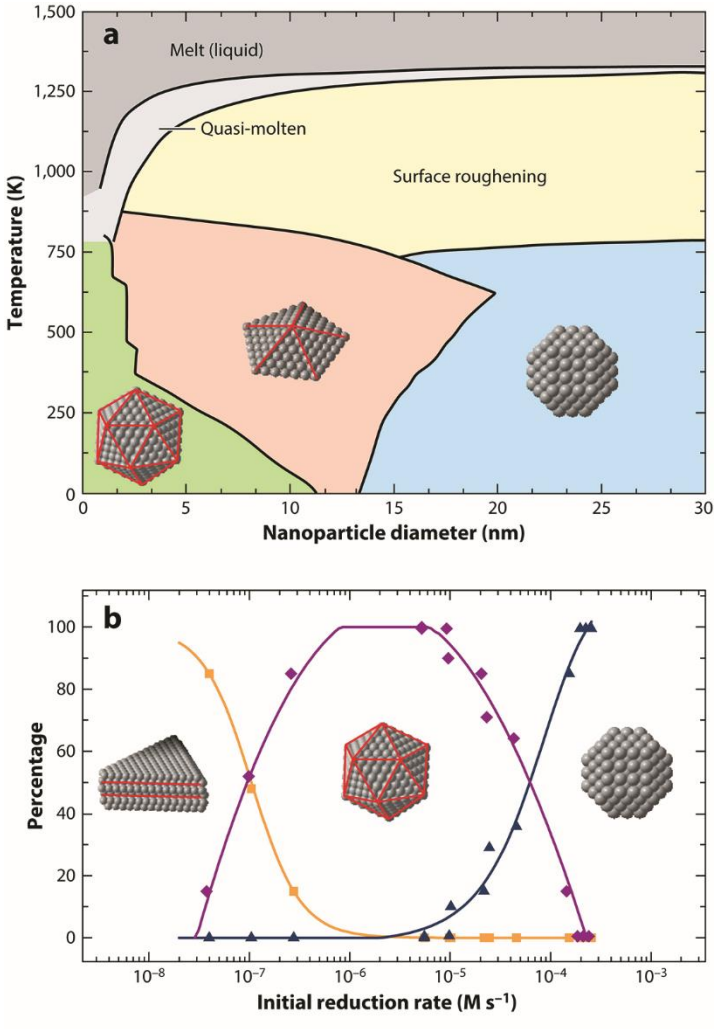

Figure 1.2. Thermodynamic and kinetic approaches, respectively, to obtaining different seed structures for nanocrystal synthesis. (A) Phase diagram of Au seeds as functions of temperature and nanoparticle size. (B) Plot displaying the percentage of Pd nanocrystal structures as a function of the initial reduction rate. Yellow data points correspond to plates with stacking faults, black to multiple-twinned icosahedra, and blue to single-crystal cuboctahedra. (Reprinted with permission from [8]. Copyright 2017 Wiley-VCH.)

Kinetic controls can be further fine-tuned after desired seeds are formed to generate even more complex compositions and morphologies. This is typically done through tuning one of two parameters: *i)* the reduction rate, or atom deposition rate (V_{dep}), which controls the rate at which new metal atoms may be added to existing seeds, or the formation of new seeds; and *ii)* the adatom surface diffusion rate (V_{dif}), which controls the rate at which newly added surface atoms to seeds can conformally diffuse across the surface [13]. This strategy

has been used generate particles such as penta-twinned rods, or high-index geometry structures such as tetrahexahedra or octopods [10, 14-17]. In these cases, by leveraging the effects of capping agents combined with both reduction and surface diffusion kinetics, kinetically controlled products and be readily and reproducible synthesized.

The same strategy can also be extended to control the formation of bimetallic nanocrystals [18]. For example, in the case of Pd@Rh core-frame or Pd@Pt core-shell nanocubes, the seed particle is a Pd cube [19, 20]. By slowly adding Rh or Pt precursor at a slow rate under fast reduction conditions, new metal atoms can be generated, but at a concentration too low for new nucleation. The new Rh or Pt metal atoms can then deposit onto the available corner and edge sites which are not passivated by bromide. By modulating the temperature, the V_{dif} can be dramatically increased or decreased, allowing for or preventing the diffusion and conformal coating of Rh/Pt adatoms before more new atoms are deposited. By tuning the V_{dep} versus the V_{dif}, frames or conformal shells with atomic layer controlled thickness can be readily produced. This strategy can then be easily translated to different templates and materials to achieve the desired morphology or composition.

In addition to varying the atom deposition and diffusion rates, nanocrystal synthesis can also be controlled by changing the favored reduction pathway [21]. The reduction of metal precursors can occur through either homogeneous solution reduction (used to generate seeds or deposit new metal atoms onto preexisting seeds), or through autocatalytic surface reduction on the face of an existing seed (results in purely growth and no new nucleation). The ability to control which pathway is favored during a reaction can prevent unwanted secondary nucleation from occurring and promote the growth of specific structures. The growing understanding of the wide variety of kinetic parameters that influence both nanocrystal nucleation and growth has enabled the synthesis many highly complex geometries that would not have been attainable only a decade ago.

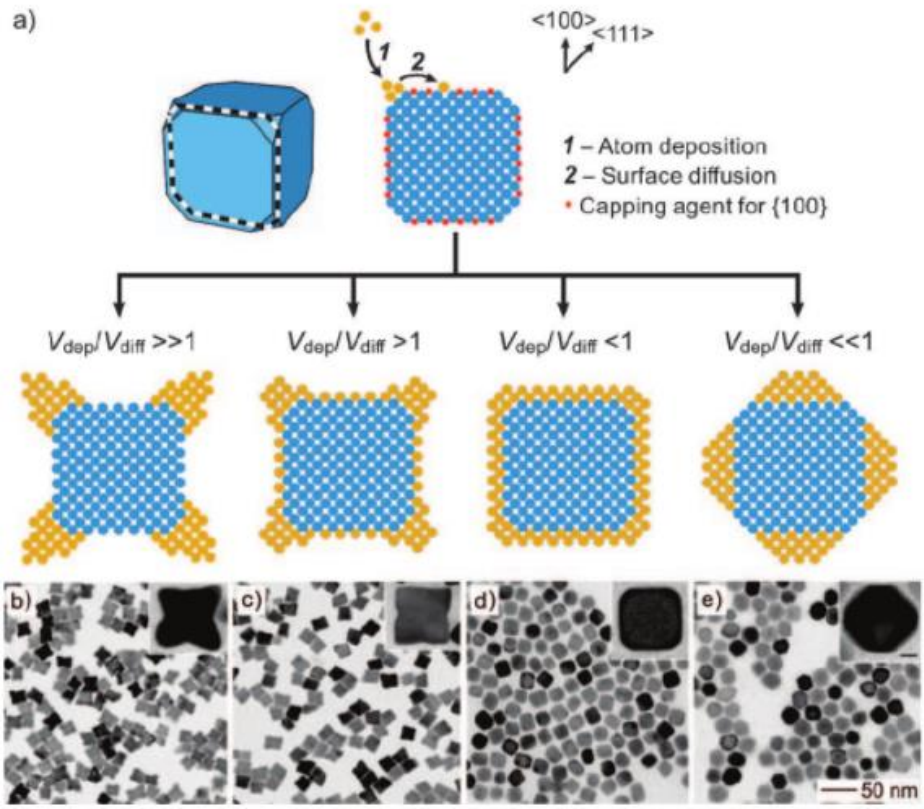

Figure 1.3. (A) Kinetic effects of tuning the rate of V_{dep} relative to V_{dif} using a palladium cube as a template, where the {100} facets are selectively capped with bromide to prevent atom deposition on the faces. As V_{dif} is increased by increasing temperature, the dominant products formed change from (B) octopods (0 °C), to (C) concave cubes (22 °C), to (D) rounded cubes (50 °C), to (E) octahedra (75 °C). (Reprinted with permission from [8]. Copyright 2017 Wiley-VCH.)

Applications of Metal Nanocrystals

Metal nanocrystals are used in a wide array of applications that both enable and improve the quality of modern life. These include electronics and information storage [22-27], photonics for medical imaging and sensing, drug delivery and cancer theranostics [28-32], energy storage and conversion [33-36], and environmental protection [35]. Perhaps one of the most critical applications for nanocrystals has been their use in high-performance catalysis [37-40], where the inherently high surface area makes nanocrystals ideal catalysts. A wide variety of catalytic reactions that are vital to modern society currently require the use of precious and rare metals such as Pd and Pt. Additionally, as demand increases for

such metals, supply is not expected to significantly increase due to the low abundance of such precious metals in the earth's crust. It is therefore critical to develop next generation nanocatalysts that maximize both catalytic activity and durability in order to minimize the use of these precious metals.

Beyond size and surface area considerations, structure-property function plays a critical role in evaluating nanocrystal catalytic performance [41-43]. Because of the difference in coordination number and "dangling bonds" between surface atoms located on different facets of the same crystal, the localized electronic structure will also change based on the nanocrystal facet, and on the atom sites along face, edge, or corner. For face-centered cubic (*fcc*) nanocrystals, the free energy associated with low-index facets (in vacuum) is as follows: $\gamma_{\{110\}} > \gamma_{\{100\}} > \gamma_{\{111\}}$ [44]. High-index facets have higher free energy terms, and low coordination atoms such as those situated on edges or corners have even higher energy than atoms along faces. For this reason, the binding energy of molecules to the surface atom sites can vary tremendously even across the same metal. When a nanocrystal is synthesized to be enclosed by facets that have a favorable binding to promote a given catalytic reaction, dramatic enhancements can be achieved. For example, Somorjai's group found while examining Pt catalysts that nanocrystals enclosed by {100} facets promoted solely the production of cyclohexene from the hydrogenation of benzene, whereas Pt nanocrystals enclosed by {111} facets produced both cyclohexane and cyclohexene [45]. Liu and co-workers studied the effect of Pd {100} facets (as cubes) versus Pd {111} facets (as octahedra) on the aerobic oxidation of 5-hydroxymethyl-2-furfural, and coupled with density functional theory calculations found a lower energy barrier pathway for octahedra, resulting in a turnover frequency 2.6 times higher than that of the cubes [46]. Similarly, Xia and coworkers investigated the role of shape control in Pd on formic acid oxidation activity, and determined that {100} facets had substantially enhanced activity over {111} facets on single-crystal catalysts, but that twin-defect nanocrystals improved activity even further [47].

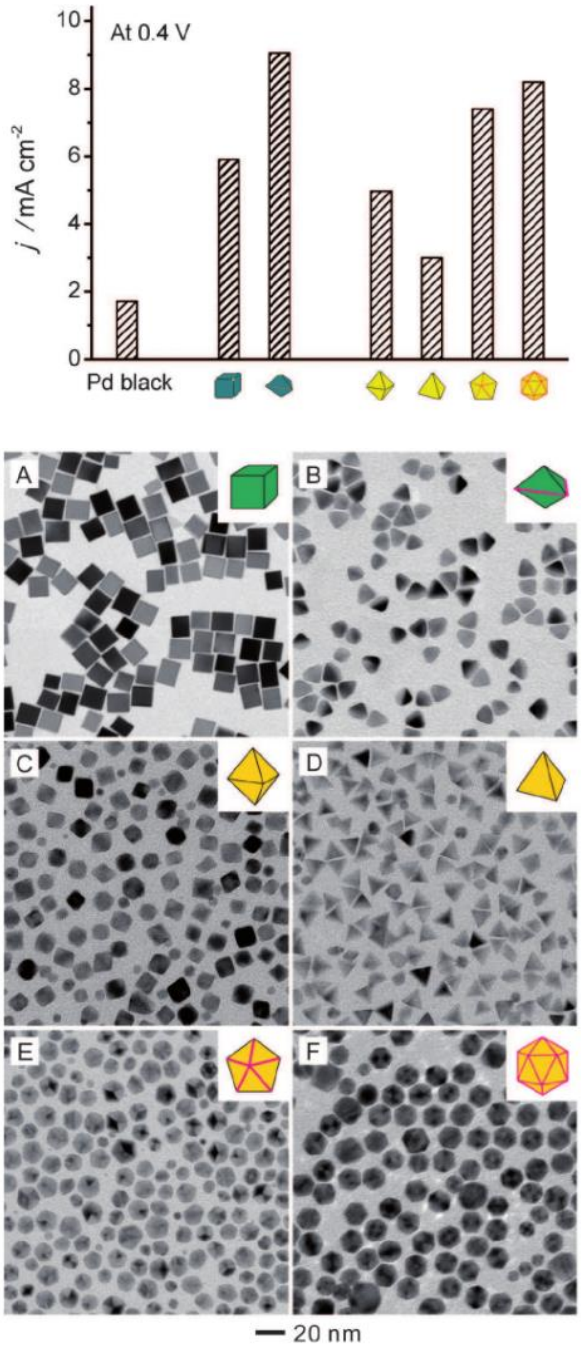

Figure 1.4. Comparison of the activity for formic acid oxidation between various Pd nanocrystals and against commercial Pd black. TEM images and corresponding models of the Pd nanocrystals tested: (A) cubes; (B) right bipyramids; (C) octahedra; (D) tetrahedra; (E) decahedra; and (F) icosahedra. (Reprinted with permission from [47]. Copyright 2017 Wiley-VCH.)

One of the most critical catalytic reactions of current and growing interest is the oxygen reduction reaction (ORR) for the polymer electrolyte membrane fuel cell (PEMFC) [48]. The PEMFC is of strong interest for the automotive industry as there is a large push to move away from oil-based products and internal combustion engines, and toward greener and renewable power sources that are environmentally friendly. In a PEMFC, H_2 and O_2 fuel are split apart at the anode and cathode, respectively, and then recombine to produce energy to power the vehicle, and water as a byproduct. However, the O_2 splitting reaction at the cathode of the PEMFC has very sluggish reaction kinetics. Therefore, to drive oxygen splitting at an appreciable rate as required to power a car, a high-performance catalyst is required. To this end, Pt has emerged as the current standard catalyst employed by the industry for the ORR. Nonetheless, vast improvements to the performance (both activity and durability) of current Pt catalysts is necessary in order to make PEMFCs a commercially viable technology [48, 49]. Technical targets set by the U.S. Department of Energy require Pt loading for fuel cell reactors to be reduced down to 0.125 mg cm^{-2} from current values of 0.4–1.0 mg cm^{-2}.

Using the ORR as a spotlight example, an increasing amount of fundamental research in the last decade has been conducted on Pt-based catalysts, with the goal of enhancing both activity and durability toward the ORR. The ORR makes for an excellent model reaction to test and evaluate next generation catalysts, and advancements made for Pt catalysts and the ORR can also presumably be translated to other critical Pt and noble-metal reactions. Strategies toward enhancing catalytic performance include not only size and shape control, but also tuning the nanocrystal composition (*i.e.* bimetallics) and morphology (*i.e.* alloy, intermetallic, core-shell) [50-57]. Breakthroughs in the synthesis of novel shapes and morphologies have led to recent record-breaking activity measurements for ORR as well as many other catalytic applications, with continued improvements to both activity and durability still anticipated.

1.2 Transmission Electron Microscopy

Arguably the most critical tool toward characterizing and understanding the fundamentals of nanomaterials has been electron microscopy. Transmission electron microscopy (TEM) can image materials stable under the electron beam down to the nanometer scale, producing a two-dimensional projection of the nanocrystals, and thus allowing for direct imaging of both individual nanocrystal sizes and shapes, as well as population studies. Two different imaging modalities are of main interest when working with very small (sub-20 nm) metal nanocrystals: TEM, and high-angle annular dark field scanning TEM (HAADF-STEM). Both imaging techniques offer different benefits when using them to analyze nanocrystals, through different processes that occur during bombardment of a sample with an electron beam.

In conventional TEM, imaging is possible through the principle of transmission or direct absorption of electrons by a material. When characterizing a metal nanocrystal sample (typically drop casted onto a thin carbon-coated copper grid of 10-20 nm in thickness), the metal atoms in the nanoparticle are considered extremely electron-dense compared to the underlying carbon support. Using an electron beam with an accelerating voltage of 120 kV as an example, the electrons are focused into a coherent beam with a crossover point set to the nanocrystal sample itself. Because of the large difference in electron density between carbon and the metal atoms of the nanocrystals, electrons that strike the carbon support largely pass through, while electrons that strike the metal atoms are largely absorbed or scattered in comparison. The image produced by this transmitted electron beam therefore forms as a high contrast image, with metal atoms and structures appearing very dark, and carbon or the background appearing very light. This projected imaging allows for the characterization of exact nanocrystal size and shape, both on an individual basis and on a population basis.

HAADF-STEM relies on the principle of electron scattering for imaging. In this case, when the electron beam hits the sample, the metal atoms have a much stronger capability

to scatter the electrons at a high angle relative to the incident beam compared to the carbon. By placing a ring detector below the sample, the scattered electrons can be measured, generating a reverse contrast image wherein the metal nanocrystals show as bright white, and the background is black due to lack of scattered electrons. Critically, this process also directly correlates to the atomic mass: heavier atoms (higher *Z*-number) possess an increasingly stronger capability for efficient high-angle electron scatter. For this reason, HAADF-STEM is considered to be a *Z*-contrast imaging modality. Using the case of Pd@Pt core-shell nanocrystals as an example, Pt has a much higher *Z*-number than Pd, so using HAADF-STEM, an image can clearly demonstrate the presence of core-shell morphology or not. For core-shell separation, HAADF-STEM shows a substantially brighter shell (indicating the presence of predominantly Pt) and a much dimmer core (indicating the presence of predominantly Pd). If the nanocrystals are alloyed instead, then the HAADF-STEM image would show no brightness contrast.

Another process that can also be monitored from electron bombardment of a nanocrystal substrate is the production of X-rays. When a high-energy electron from the beam strikes an atom (especially heavier atoms such as metals), it can excite an electron in one of the inner valence orbitals up to higher orbital. When this excited electron then decays back to a lower orbital, it releases an X-ray. The X-rays possess distinct wavelengths for different elements, and can be monitored using an energy dispersive X-ray spectroscopy (EDX) detector in the microscope. EDX allows for the elemental mapping and analysis of nanocrystal samples, which (when coupled with TEM and HAADF-STEM imaging) can be used to fully confirm nanocrystal size, shape, morphology, and composition. The ability to also use these multiple analytical techniques in parallel with one another further highlights why electron microscopy is so central to nanocrystal characterization and development.

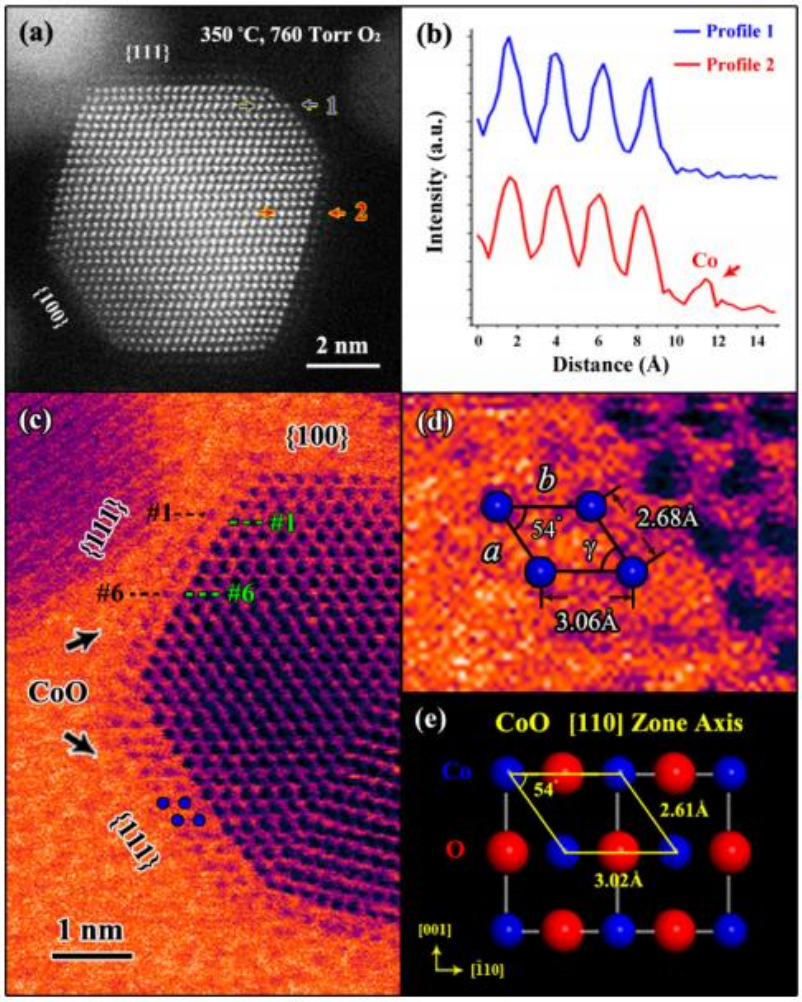

Figure 1.5. (a) Atomic-resolution and *in situ* observation of a PtCo nanocrystal under heating and an oxidative environment. (b) Intensity profile of the atomic columns corresponding to the blue and red arrows in (a). (c) Colored bright field STEM image and corresponding atomic image and models (d, e) demonstrating the formation of CoO layer on the surface has formed at the heated and oxidative conditions. (Reprinted with permission from [69] with permission. Copyright 2017 American Chemical Society.)

Additionally, large breakthroughs have been made over the past few decades in promoting the technology for aberration-corrected microscopes. Aberration-corrected TEM is a technique that adjusts for the aberrations naturally present in the electron beam from the magnetic lenses, allowing for even higher resolution imaging, down to ~0.6 Å. Using aberration-corrected microscopes enables the atomic-resolution characterization of nanocrystals, and opens up a myriad of atomistic-based analyses. This now commercialized

technique makes it possible to directly image and confirm a variety of structural and morphological characteristics on a per-particle basis, including lattice spacing, facet expression, surface structure (*e.g.* presence of steps, kinks, and terraces), and crystal defects (*e.g*. stacking faults, and single or multiple-twin boundaries) [58, 59]. For this reason, high resolution TEM (HRTEM) has become a critical characterization tool in analyzing and understanding nanocrystal size, shape, composition, and morphology.

However, a major drawback to electron microscopy analysis has historically been the *ex situ* nature of the imaging itself, run in isolated ultra-high vacuum environments under high electron dosage. Given the analytical limitations of atomistic-level analysis, it is critical to develop new methods by which to determine mechanistic insights for nanocrystal formation, synthesis, and behavior under different heterogenous environments such as those used in catalysis. To this end, the past decade has seen tremendous evolution in the development of commercial *in situ* electron microscopy techniques. Multiple companies currently offer various *in situ* or "environmental" TEM holders, each geared toward different real-time studies, including nanocrystal heating, nanocrystal liquid cells, and nanocrystal gaseous cells [60-62]. For the first time, this has allowed researchers to actively study the atom-level changes to nanocrystals in real time, such a nanocrystal growth, alloying, and surface and crystal reconstruction [63-70].

The advances in microscopy have resulted in a recent and tremendous growth of *in situ* nanocrystal studies, with critical insights toward fundamental mechanisms that could not otherwise be proven or derived. Electron microscopy analyses are still limited by factors such as the impacts of electron beam dosage on samples, the inability to directly mimic exact catalytic or synthetic environments, and the inability to easily image non-heavy metal elements [71-74]. Nonetheless, electron microscopy continues to remain perhaps the most important analytical method for characterizing and understanding nanocrystal-based systems, offering cutting edge, sub-angstrom direct imaging capabilities that can now be readily coupled to *in situ* testing and elemental analysis.

1.3 Scope of This Work

The focus of this dissertation is two-fold: *i*) to develop new methods for the facile, reproducible, and scalable syntheses of metal nanocrystals, and *ii*) to utilize *in situ* electron microscopy techniques to evaluate and understand the potential use of such nanocrystals for applications at elevated temperatures. Substantial enhancements to the controlled synthesis and performance of nanocatalysts has been made over the last few decades. However, many synthetic protocols remain limited to small, benchtop reactions that are not amenable to industrial scale-up, and most catalytic evaluation relies on a trial-and-error approach, with limited investigations focusing on stability and durability. This dissertation aims to explore synthetic routes and mechanistic pathways that may be more amenable to scale-up and manufacturing, and to examine trends and structure-property relationships that can predictably determine the thermal durability of nanocatalysts of interest.

In Chapter 2, I report on a photochemical, room-temperature method for the synthesis of 12-nm edge length Pd nanocubes decorated with atomic steps and terraces on the surface. Palladium single-crystal seeds were generated using a strong UV-vis light source to excite the Pd(II) complex, allowing it to be reduced even at room temperature. The impacts of room temperature on the mechanisms for Pd(II) reduction and Pd nanocrystal growth were carefully investigated. Finally, the effect of low coordination surface sites (*e.g.* atomic steps and terraces) on formic acid oxidation were tested by comparing the Pd nanocubes with steps and terraces against Pd cubes with smooth {100} faces and Pd cubes with truncated corners.

In Chapter 3, I develop a one-pot method for the synthesis of Pd concave cubes at room temperature. The generation of single-crystal seeds and the subsequent overgrowth was controlled at room temperature by pairing a reducing agent of appropriate reducing power (sodium ascorbate) to the metal salt precursor ($PdBr_4^{2-}$). A kinetic study of the synthesis further revealed that the concave structures were obtained due to two separate

kinetic events: solution reduction (which generated the single-crystal seeds), followed by surface reduction (which generated the final morphology through autocatalytic reduction). The switch between these two kinetic pathways provided the mechanism for the one-pot method. Simultaneously, the room-temperature conditions enabled the generation of low-coordination surface atoms due to the inherently low adatom surface diffusion rate from the corners to the bromide-capped {100} facets.

In Chapter 4, I report on a systematic study of Pd@Pt_{4L} core-shell cubes and octahedra under *in situ* heating using high-resolution HAADF-STEM. Using this method, I was able to characterize the thermal stability of this class of nanocatalysts in real time, and evaluate changes to both shape and core-shell structure (*e.g.* facet expression and alloying, respectively) when heated. Comparison of the two structures revealed that octahedra retained shape at higher temperatures, but alloyed at lower temperatures compared to cubes. Coupled to density functional theory calculations, it was found that the cubes readily deformed and lost their facets at a lower temperature than the octahedra due to a lower energy barrier to edge atom movement on {100} facet-enclosed structures versus {111} facet-enclosed structures. Conversely, it was determined that the octahedra alloyed at a lower temperature than the cubes because of a greater tendency to form subsurface vacancies during the formation of {111} facets, leading to preferential subsurface substitution and alloying.

In Chapter 5, I perform a study on the thermal stability Pt cubic, octahedral, and icosahedral nanocages (with an average wall thickness of *ca*. 6 atomic layers) using *in situ* heating coupled with atomic-resolution TEM and HAADF-STEM. The Pt nanocages were all synthesized from Pd@$Pt_{5\text{-}6L}$ core-shell templates by etching away the Pd core, making them ideal catalysts with a high surface area and Pt dispersion. A systematic evaluation of the Pt-based nanocages showed the same breakdown process under thermal stress: wherein nanocages evolved into nanoframes before fragmenting into smaller pieces. More specifically, deformation occurred through enlargement of the holes left from Pd etching

and migration of atoms toward the edges of the particles. The transformation into nanoframes from nanocages could be thermodynamically rationalized by the trend to reduce the exposed surface area. It was found that the cubic nanocages exhibited the highest thermal stability, followed by the octahedral and the icosahedral samples. The location of the etching pores appeared to affect the observed stability, indicating that finer control over etching could enhance stability for hollow nanostructures.

1.5 References

[1] Freestone, I.; Meeks, N.; Sax, M.; Higgitt, C. *Gold Bull.* **2007,** *40*, 270-277.

[2] Habashi, F. *Eur. Chem. Bull.* **2016,** *5*, 416-419.

[3] Duncan, K. A.; Johnson, C.; McElhinny, K.; Ng, S.; Cadwell, K. D.; Zenner Petersen, G. M.; Johnson, A.; Horoszewski, D.; Gentry, K.; Lisensky, G.; Crone, W. C. *J. Chem. Ed.* **2010,** *87*, 1031-1038.

[4] LaMer, V. K.; Dinegar, R. H. *J. Am. Chem. Soc.* **1950,** *72*, 4847-4854.

[5] Polte, J. *CrystEngComm* **2015,** *17*, 6809-6830.

[6] Yin, Y.; Alivisatos, A. P. *Nature* **2005,** *437*, 664-670.

[7] Barnard, A. S.; Young, N. P.; Kirkland, A. I.; van Huis, M. A.; Xu, H. *ACS Nano* **2009,** *3*, 1431-1436.

[8] Xia, Y.; Gilroy, K. D.; Peng, H.-C.; Xia, X. *Angew. Chem. Int. Ed.* **2017,** *56*, 60-95.

[9] Wang, Y.; Peng, H.-C.; Liu, J.; Huang, C. Z.; Xia, Y. *Nano Lett.* **2015,** *15*, 1445-1450.

[10] Xiong, Y.; Xia, Y. *Adv. Mater.* **2007,** *19*, 3385-3391.

[11] Tao, A. R.; Habas, S.; Yang, P. *Small* **2008,** *4*, 310-325.

[12] Xia, Y.; Xiong, Y.; Lim, B.; Skrabalak, S. E. *Angew. Chem. Int. Ed.* **2009,** *48*, 60-103.

[13] Xia, Y.; Xia, X.; Peng, H.-C. *J. Am. Chem. Soc.* **2015,** *137*, 7947-7966.

[14] Ming, T.; Feng, W.; Tang, Q.; Wang, F.; Sun, L.; Wang, J.; Yan, C.. *J. Am. Chem. Soc.* **2009,** *131*, 16350-16351.

[15] DeSantis, C. J.; Peverly, A. A.; Peters, D. G.; Skrabalak, S. E. *Nano Lett.* **2011,** *11*, 2164-2168.

[16] Graham, L.; Collins, G.; Holmes, J. D.; Tilley, R. D. *Nanoscale* **2016,** *8*, 2867-2874.

[17] Jansons, A. W.; Plummer, L. K.; Hutchison, J. E. *Chem. Mater.* **2017,** *29*, 5415-5425.

[18] Gilroy, K. D.; Ruditskiy, A.; Peng, H.-C.; Qin, D.; Xia, Y. *Chem. Rev.* **2016,** *116*, 10414-10472.

[19] Xie, S.; Lu, N.; Xie, Z.; Wang, J.; Kim, M. J.; Xia, Y. *Angew. Chem. Int. Ed.* **2012,** *51*, 10266-10270.

[20] Xie, S.; Choi, S.-I.; Lu, N.; Roling, L. T.; Herron, J. A.; Zhang, L.; Park, J.; Wang, J.; Kim, M. J.; Xie, Z.; Mavrikakis, M.; Xia, Y.,. *Nano Lett.* **2014,** *14*, 3570-3576.

[21] Yang, T.-H.; Peng, H.-C.; Zhou, S.; Lee, C.-T.; Bao, S.; Lee, Y.-H.; Wu, J.-M.; Xia, Y.,. *Nano Lett.* **2017,** *17*, 334-340.

[22] Okinaka, Y.; Hoshino, M.,. *Gold Bull.* **1998,** *31*, 3-13.

[23] Murray, C. B.; Sun, S.; Doyle, H.; Betley, T. *MRS Bull.* **2001,** *26*, 985-991.

[24] Rao, R. A.; Steimle, R. F.; Sadd, M.; Swift, C. T.; Hradsky, B.; Straub, S.; Merchant, T.; Stoker, M.; Anderson, S. G. H.; Rossow, M.; Yater, J.; Acred, B.; Harber, K.; Prinz, E. J.; White, B. E.; Muralidhar, R.,. *Solid-State Electron.* **2004,** *48*, 1463-1473.

[25] Jeong, S.; Woo, K.; Kim, D.; Lim, S.; Kim, J. S.; Shin, H.; Xia, Y.; Moon, J.,. *Adv. Funct. Mater.* **2008,** *18*, 679-686.

[26] Chang, T.-C.; Jian, F.-Y.; Chen, S.-C.; Tsai, Y.-T. *Mater. Today* **2011,** *14*, 608-615.

[27] Panthani, M. G.; Korgel, B. A. *Ann. Rev. Chem. Biomol. Eng.* **2012,** *3*, 287-311.

[28] Paul, A. *Nat. Biotechnol.* **2003,** *22*, 47.

[29] Jain, P. K.; El-Sayed, I. H.; El-Sayed, M. A. *Nano Today* **2007,** *2*, 18-29.

[30] Junghanns, J.-U. A. H.; Müller, R. H. *Int. J. Nanomedicine* **2008,** *3*, 295.

[31] Wang, X.; Yang, L.; Chen, Z.; Shin, D. M. *CA Cancer J. Clin.* **2008,** *58*, 97-110.

[32] Wicki, A.; Witzigmann, D.; Balasubramanian, V.; Huwyler, J. *J.Control. Release* **2015,** *200*, 138-157.

[33] Nozik, A. J.; Miller, J. *Chem. Rev.* **2010,** *110*, 6443-6445.

[34] Linic, S.; Christopher, P.; Ingram, D. B. *Nat. Mater.* **2011,** *10*, 911-921.

[35] Hu, X.; Li, G.; Yu, J. C. *Langmuir* **2010,** *26*, 3031-3039.

[36] Sun, Q.-C.; Ding, Y. C.; Sagar, D. M.; Nagpal, P. *Prog. Surf. Sci.* **2017**, *in press*

[37] Somorjai, G. A. *Chem. Rev.* **1996,** *96*, 1223-1236.

[38] Li, Y.; Somorjai, G. A. *Nano Lett.* **2010,** *10*, 2289-2295.

[39] Zhou, K.; Li, Y. *Angew. Chem. Int. Ed.* **2012,** *51*, 602-613.

[40] Wu, Y.; Wang, D.; Li, Y. *Chem. Soc. Rev.* **2014,** *43*, 2112-2124.

[41] Lee, K.; Kim, M.; Kim, H. *ChemInform* **2010,** *41*.

[42] Xie, S.; Choi, S.-I.; Xia, X.; Xia, Y. *Curr. Opin. Chem. Eng.* **2013,** *2*, 142-150.

[43] You, H.; Yang, S.; Ding, B.; Yang, H. *Chem. Soc. Rev.* **2013,** *42*, 2880-2904.

[44] Vitos, L.; Ruban, A. V.; Skriver, H. L.; Kollár, J. *Surf. Sci.* **1998,** *411*, 186-202.

[45] Bratlie, K. M.; Lee, H.; Komvopoulos, K.; Yang, P.; Somorjai, G. A. *Nano Lett.* **2007,** *7* , 3097-3101.

[46] Lei, D.; Yu, K.; Li, M.-R.; Wang, Y.; Wang, Q.; Liu, T.; Liu, P.; Lou, L.-L.; Wang, G.; Liu, S. *ACS Catal.* **2017,** *7*, 421-432.

[47] Choi, S.-I.; Herron, J. A.; Scaranto, J.; Huang, H.; Wang, Y.; Xia, X.; Lv, T.; Park, J.; Peng, H.-C.; Mavrikakis, M.; Xia, Y *ChemCatChem* **2015,** *7*, 2077-2084.

[48] Gasteiger, H. A.; Kocha, S. S.; Sompalli, B.; Wagner, F. T. *App. Catal. B: Environ.* **2005,** *56*, 9-35.

[49] Birss, V.; El Sawy, E.; S., K.; Keyvanfar, P.; Li, X.; Young, J., *Handbook of Industrial Chemistry and Biotechnology*. Springer: 2017.

[50] Greeley, J.; Stephens, I. E. L.; Bondarenko, A. S.; Johansson, T. P.; Hansen, H. A.; Jaramillo, T. F.; Rossmeisl, J.; Chorkendorff, I.; Nørskov, J. K. *Nat. Chem.* **2009,** *1*, 552.

[51] Wang, D.; Xin, H. L.; Hovden, R.; Wang, H.; Yu, Y.; Muller, D. A.; DiSalvo, F. J.; Abruña, H. D. *Nat. Mater.* **2013,** *12*, 81-87.

[52] Chen, C.; Kang, Y.; Huo, Z.; Zhu, Z.; Huang, W.; Xin, H. L.; Snyder, J. D.; Li, D.; Herron, J. A.; Mavrikakis, M.; Chi, M.; More, K. L.; Li, Y.; Markovic, N. M.; Somorjai, G. A.; Yang, P.; Stamenkovic, V. R. *Science* **2014,** *343*, 1339-1343.

[53] Huang, X.; Zhao, Z.; Cao, L.; Chen, Y.; Zhu, E.; Lin, Z.; Li, M.; Yan, A.; Zettl, A.; Wang, Y. M.; Duan, X.; Mueller, T.; Huang, Y. *Science* **2015,** *348*, 1230-1234.

[54] Park, J.; Zhang, L.; Choi, S.-I.; Roling, L. T.; Lu, N.; Herron, J. A.; Xie, S.; Wang, J.; Kim, M. J.; Mavrikakis, M.; Xia, Y. *ACS Nano* **2015,** *9*, 2635-2647.

[55] Zhang, L.; Roling, L. T.; Wang, X.; Vara, M.; Chi, M.; Liu, J.; Choi, S.-I.; Park, J.; Herron, J. A.; Xie, Z.; Mavrikakis, M.; Xia, Y. *Science* **2015,** *349*, 412-416.

[56] Li, M.; Zhao, Z.; Cheng, T.; Fortunelli, A.; Chen, C.-Y.; Yu, R.; Zhang, Q.; Gu, L.; Merinov, B. V.; Lin, Z.; Zhu, E.; Yu, T.; Jia, Q.; Guo, J.; Zhang, L.; Goddard, W. A.; Huang, Y.; Duan, X. *Science* **2016,** *354*, 1414-1419.

[57] Vej-Hansen, U. G.; Escudero-Escribano, M.; Velázquez-Palenzuela, A.; Malacrida, P.; Rossmeisl, J.; L. Stephens, I. E.; Chorkendorff, I.; Schiøtz, J. *Electrocatalysis* **2017,** *8*, 594-604.

[58] Pennycook, S. J.; Varela, M.; Hetherington, C. J. D.; Kirkland, A. I. *MRS Bull.* **2006,** *31*, 36-43.

[59] Tanaka, N. *Sci. Technol. Adv. Mater.* **2008,** *9* (1), 014111.

[60] Yuk, J. M.; Park, J.; Ercius, P.; Kim, K.; Hellebusch, D. J.; Crommie, M. F.; Lee, J. Y.; Zettl, A.; Alivisatos, A. P. *Science* **2012,** *336*, 61-64.

[61] Ferreira, P. J.; Mitsuishi, K.; Stach, E. A. *MRS Bull.* **2008,** *33*, 83-90.

[62] Joshua, D. S.; Andrei, K. *Nanotechnology* **2012,** *23*, 505704.

[63] Liao, H.-G.; Zheng, H. *J. Am. Chem. Soc.* **2013,** *135*, 5038-5043.

[64] Odahara, G.; Otani, S.; Oshima, C.; Suzuki, M.; Yasue, T.; Koshikawa, T. *Surf. Sci.* **2011,** *605*, 1095-1098.

[65] Yuk, J.; Park, J.; Ercius, P.; Kim, K.; Hellebusch, J.; Crommie, F.; Lee, J.; Zettl, A.; Paul, A. *Lawrence Berkeley National Laboratory* **2013**.

[66] Xin, H. L.; Niu, K.; Alsem, D. H.; Zheng, H. *Microsc. Microanal.* **2013,** *19*, 1558-1568.

[67] Xu, W.; Bowes, P. C.; Grimley, E. D.; Irving, D. L.; LeBeau, J. M. *App. Phys. Lett.* **2016,** *109*, 201601.

[68] Avanesian, T.; Dai, S.; Kale, M. J.; Graham, G. W.; Pan, X.; Christopher, P. *J. Am. Chem. Soc.* **2017,** *139*, 4551-4558.

[69] Dai, S.; Hou, Y.; Onoue, M.; Zhang, S.; Gao, W.; Yan, X.; Graham, G. W.; Wu, R.; Pan, X. *Nano Lett.* **2017,** *17*, 4683-4688.

[70] Grogan, J. M.; Schneider, N. M.; Ross, F. M.; Bau, H. H. *Nano Lett.* **2014,** *14*, 359-364.

[71] Stahlberg, H.; Walz, T. *ACS Chem. Bio.* **2008,** *3*, 268-281.

[72] Hansen, T. W.; Wagner, J. B.; Dunin-Borkowski, R. E. *Mater. Sci. Technol.* **2010,** *26*, 1338-1344.

[73] Schneider, N. M.; Norton, M. M.; Mendel, B. J.; Grogan, J. M.; Ross, F. M.; Bau, H. H. *The Journal of Physical Chemistry C* **2014,** *118*, 22373-22382.

[74] Ross, F. M. *Science* **2015,** *350*, 1490

CHAPTER 2

A PHOTOCHEMICAL, ROOM-TEMPERATURE SYNTHESIS OF CUBE-LIKE PALLADIUM NANOCRYSTALS WITH HIGHLY TERRACED FACES

2.1 Introduction

Palladium is an essential catalytic material for a variety of industrially important reactions ranging from hydrogenation and dehydrogenation to organic cross-coupling [1-4]. Most of these applications benefit from the availability of Pd nanocrystals with well-controlled facets because of their inherently high surface area to volume ratios and the presence of surface structures engineered to suit different chemical reactions. Over the past two decades, an array of methods has been developed for controlling the facets expressed on noble-metal nanocrystals, allowing for the design of heterogeneous catalysts with enhanced activity and/or selectivity. These methods can be broadly divided into two major categories: *i*) one-pot synthesis in which an organometallic or salt precursor is decomposed and/or reduced to generate metal atoms, followed by their nucleation and growth into nanocrystals [5-8] and *ii*) seed-mediated growth, a two-step process wherein seeds are formed in one synthesis and then used in a second process to obtain nanocrystals with a specific shape [9-12]. Both approaches benefit from the addition of a capping agent to direct the development of a specific type of facet on the surface. Seed-mediated growth is particularly versatile and viable in generating nanocrystals with complex shapes enclosed by high-index facets. However, multiple steps are often necessary to achieve a tight control over the faceting process.

Most of the synthetic methods reported in literature require the use of an elevated temperature to decompose a precursor or activate its reduction. Thermally-activated processes may experience complications arising from the inhomogeneous distribution of

reagents (*e.g.*, the reducing agent or precursor) upon their introduction, as well as the intrinsic temperature gradient in the reaction medium caused by the release, intake, and transfer of heat by molecular species involved in the synthesis. It would thus be highly desirable to develop a room-temperature method to eliminate these concerns while still maintaining a tight control over the faceting process. In browsing the literature, I only found a small number of reports on the one-step synthesis of Pd nanocrystals at room temperature, the majority of which demonstrated little or no control over the shape (or size) of the nanocrystals [13-15]. Part of the problem can be attributed to the limited choice of reduction reactions that can be conducted at room temperature with tunable and controllable kinetics to meet the requirements for both nucleation and growth steps. One particularly attractive solution to this problem is built around photochemical reduction. Compared with a thermally activated process, photochemical reduction offers many potential advantages, including homogeneous distribution of reactants throughout the reaction medium, convenient and precise control of energy input, and the ability to maximize the absorption of reactive species by tuning the wavelength of light [16, 17]. Photochemical reduction can also be conducted at ambient temperature without having to employ an otherwise harsh or hazardous strong reducing agent to generate metal atoms. To my knowledge, most of the research thus far into photochemical synthesis of noble-metal nanocrystals has mainly focused on Au and Ag by leveraging the localized surface plasmon resonance excitation of their nanocrystals in the visible region [17-20].

In searching the literature, I was only able to identify a few reports on the use of photochemical reduction for the synthesis of Pd nanomaterials [21-25]. Most of the papers [21-24], however, only reported photochemical deposition of Pd films or small particles on oxide substrates such as silica, quartz, or titania. The reactions were not maintained at room temperature for these syntheses, and in the limited cases where electron microscopy characterization was provided to support the claims, the Pd nanoparticles appeared to be less than 5 nm in size, with no apparent control over the shape or faceting. Only one of the

papers reported the synthesis of colloidal Pd nanocubes and nanorods by irradiating an aqueous mixture of $(NH_4)_2PdCl_4$, cetyl trimethyl ammonium bromide, and ascorbic acid with 260 nm light for 4 h [25]. However, the authors did not mention if the reaction system was maintained at room temperature during UV-vis irradiation, nor did they investigate the mechanism(s) responsible for reduction and particle formation. As shown by the high-resolution transmission electron microcopy (HRTEM) images, the Pd nanocubes had a cubic shape and were covered by smooth side faces, suggesting the possible elevation of reaction temperature during the UV irradiation.

Here I report a photochemical route that can be conducted in one pot, at room temperature, and in an aqueous solution for the facile synthesis of Pd nanocubes enriched with atomic steps and terraces on the side faces. My strategy for controlling the synthesis is multifold, including the use of three major components: *i*) Br^- as both a selective capping agent toward the {100} facets and as a coordination ligand toward Pd(II) ions; *ii*) UV-vis light to activate the Pd(II) precursor; and *iii*) ascorbic acid as a chemical reductant. Under optimized conditions, I am able to overcome the energy barrier to initiate reduction at room temperature, and controllably generate Pd nanocubes decorated with atomic steps and terraces that cannot otherwise be obtained using a synthesis conducted at an elevated temperature.

2.2 Results and Discussion

Figure 2.1 shows a general schematic of my synthesis, which involves the use of both AA and UV-vis light to reduce Pd(II) species to Pd(0) atoms at room temperature. The Pd(0) atoms then nucleate to generate single-crystal seeds, followed by their continuous growth into nanocrystals enclosed by {100} facets owing to the presence of Br^- as a selective capping agent toward Pd(100). Many different pathways have been reported in the literature to account for the photochemical reduction of transition metal ions, including but not limited to direct photochemical reduction through irradiation, as well as reduction

through the use of a molecular sensitizer. In particular, many photochemical methods rely on the use of an organic dye or chromophore that will decompose to generate radicals upon irradiation at an appropriate wavelength. These highly reactive radical species can readily reduce transition metal ions into atoms, driving the formation of nanoparticles [17,26,27]. Initially, I believed this reduction mechanism might be involved in my synthesis as AA could potentially be cleaved to form an ascorbyl radical [28]. However, the synthesis was conducted in water and in the presence of O_2 from air. Molecular oxygen is known to be an excellent radical scavenger that can easily quench radicals, thus making a radical-based reduction pathway unlikely. To verify this argument, I measured the UV-vis absorption spectra of all the individual components involved in my synthesis (Figure 2.2). While AA does possess a sharp absorption peak below 300 nm, the borosilicate glass vial used to house the reaction solution should be able to block all irradiation below 300 nm. Therefore, I could discard a reduction mechanism based on the ascorbyl radical. Instead, the reduction pathway critical to the success of this synthesis relies on the coupling between AA and UV-vis irradiation, which is highly dependent on what Pd(II) species is actually present in the reaction solution.

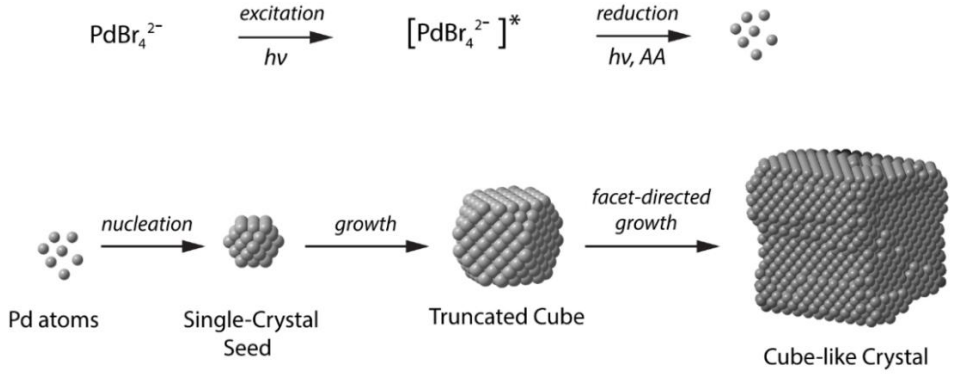

Figure 2.1. Schematic illustration showing the formation of Pd nanocubes enriched with atomic steps and terraces at room temperature through a photochemical process. The $PdBr_4^{2-}$ precursor is energized to an excited state by the UV-vis light and then reduced to Pd atoms by ascorbic acid (AA). The Pd atoms nucleate to generate single-crystal seeds, followed by their evolution into truncated cubes and then cubic nanocrystals with atomic steps and terraces on the side faces. (Reprinted with permission from [53]. Copyright 2016 American Chemical Society.)

Bromide is well-known for selectively capping Pd{100} facets, and has been extensively used to promote the formation of {100}-dominated nanocrystals such as cubes by effectively blocking the deposition of Pd new atoms on {100} facets, and thereby promoting ⟨111⟩ growth instead. However, the role of Br^- in my synthesis is two-fold, starting before Pd nanocrystals are even formed. In an aqueous solution containing halide salts, Pd(II) can form a square-planar complex coordinated by halides (Cl^- or Br^-, in my reaction solution) or by water [29-31]. The respective *d*-band and ligand-metal charge transfer absorption peaks for $PdBr_n(H_2O)_{4-n}^{2-n}$ and $PdCl_n(H_2O)_{4-n}^{2-n}$ (where $n \leq 4$) have been well established in the literature, and are distinct for each hydrated species [32,33]. Due to the difference in the respective stability constants, the exact ligands present in the coordination complex will have a strong impact on the reduction kinetics [32,34,35]. A more highly Br^--substituted complex will yield a slower reduction rate because of the increase in bonding strength and compound stability. For example, $PdCl_4^{2-}$ can be readily reduced in the presence of AA within a few minutes, even at room temperature. In contrast, my reaction mixture could not be reduced at all while sitting at room temperature in the absence of UV-vis irradiation. To this end, it was critical to identify the predominant Pd(II) species present in the reaction solution. Figure 2.3 shows a UV-vis absorption spectrum of the reaction solution in the absence of AA; all of the peaks correspond to $PdBr_4^{2-}$. Due to the high concentration of excess Br^- present in the solution, all of the Pd(II) species became $PdBr_4^{2-}$ through a quick ligand exchange process. It was $PdBr_4^{2-}$ that served as a salt precursor for the actual reduction and subsequent nanocrystal nucleation and growth, even when the initial precursor added into the reaction system was Na_2PdCl_4. If there was not sufficient excess of Br^- present in the reaction solution to fully substitute the Cl^- ligand, it would change the stability constant of Pd(II) complex and the reduction kinetics, potentially resulting in uncontrolled nucleation and loss of control over facet expression.

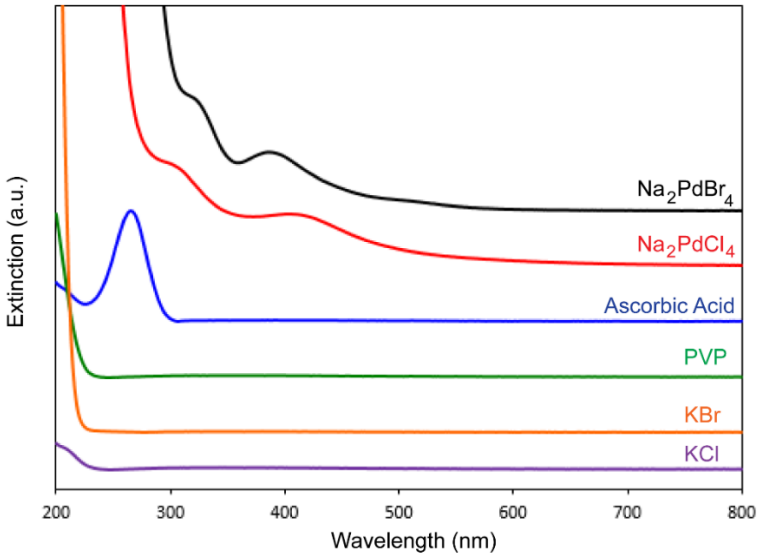

Figure 2.2. UV-vis spectra recorded from aqueous solutions of all the reactants involved in the photochemical synthesis. Notably, only the Pd(II) species absorb photons in the region above 300 nm. The spectra were recorded using quartz cuvettes, whereas the photochemical syntheses were conducted in borosilicate glass vials with an absorption cutoff around 300 nm. (Reprinted with permission from [50]. Copyright 2016 American Chemical Society.)

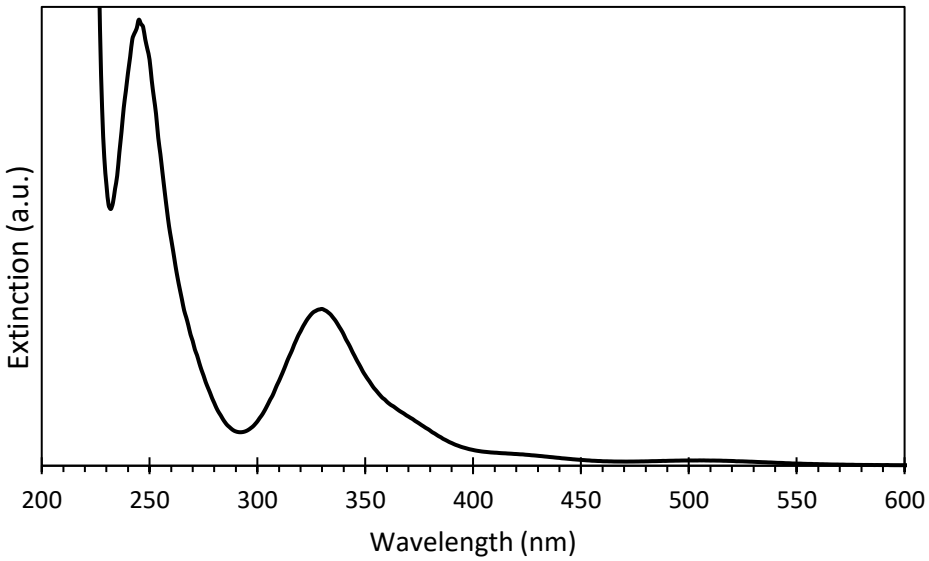

Figure 2.3. UV-vis spectrum of the Pd(II) speciation present in a typical reaction solution before the addition of ascorbic acid. All peaks present (246, 331, 366, 425, and 510 nm) correspond specifically to $PdBr_4^{2-}$, and not to any chloro- or hydrated Pd(II) species. The other expected $PdBr_4^{2-}$ peak at 274 nm is largely obscured due to its weak molar absorptivity (ε) relative to the 246 nm peak it is satellite to (5x difference in ε). Absorption spectrum was acquired in a quartz cuvette. (Reprinted with permission from [50]. Copyright 2016 American Chemical Society.)

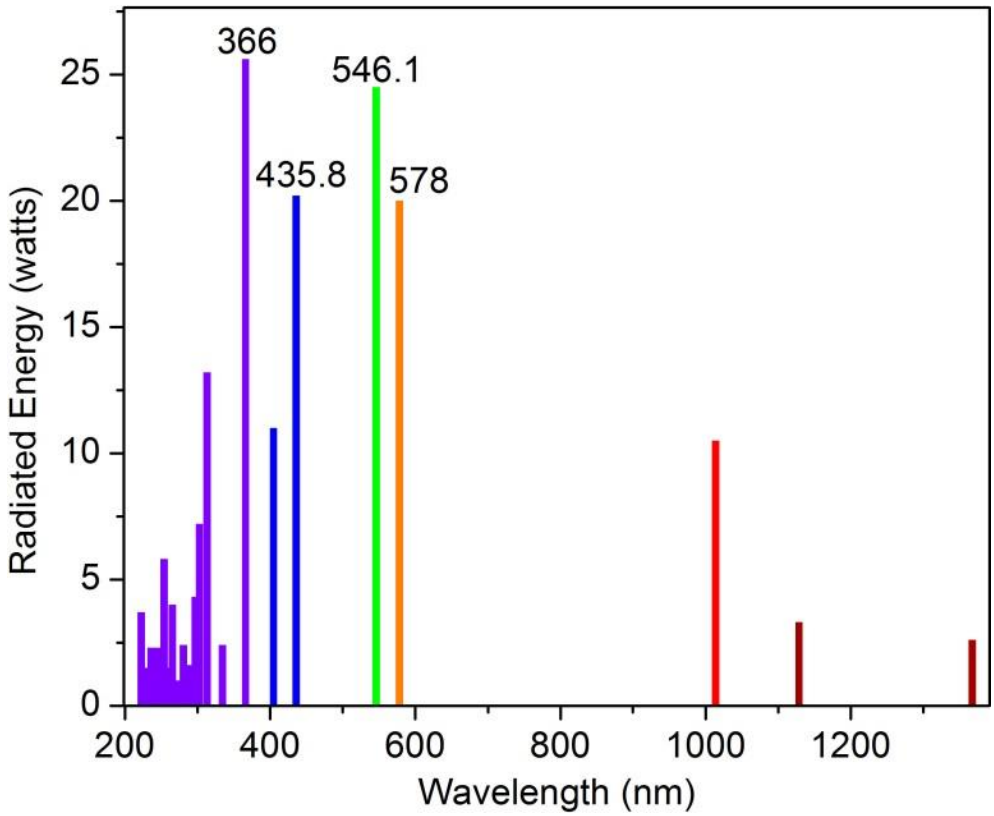

Figure 2.4. The energy distribution spectra of a quartz mercury vapor arc lamp (medium pressure) used in my photochemical synthesis. (Reprinted with permission from [53]. Copyright 2016 American Chemical Society.)

To achieve control over both nucleation and growth, it is critical to develop a reduction process that is fast enough in the initial stage to ensure the formation of single-crystal seeds but also sufficiently slow to allow for facet-controlled growth. As stated previously, $PdBr_4^{2-}$ is a stable compound that cannot be readily reduced by AA at room temperature. While there are other stronger reducing agents that can act at room temperature (*i.e.*, $NaBH_4$ and hydrazine), they can reduce $PdBr_4^{2-}$ too quickly and eliminate any facet control in the growth stage. Additionally, many of these reducing agents are hazardous to work with. I addressed this issue by employing a combination of AA and UV-vis light. Upon irradiation by a medium-pressure Hg arc lamp with strong outputs between 300–600 nm (see Figure 2.4), the $PdBr_4^{2-}$ complexes can absorb an adequate number of photons to reach

an excited state and generate $[PdBr_4^{2-}]^*$. At this excited state, the Pd(II) precursor can be readily reduced by AA even at room temperature to generate Pd(0) atoms. To ensure that the reduction is not caused by the higher energy photons alone, I confirmed that the reaction did not occur in the presence of UV-vis irradiation unless AA was also present. This observation verifies that the synthesis was based on the direct reduction of $[PdBr_4^{2-}]^*$ by AA. Only under these conditions could controlled nucleation and facet-directed growth occur at room temperature.

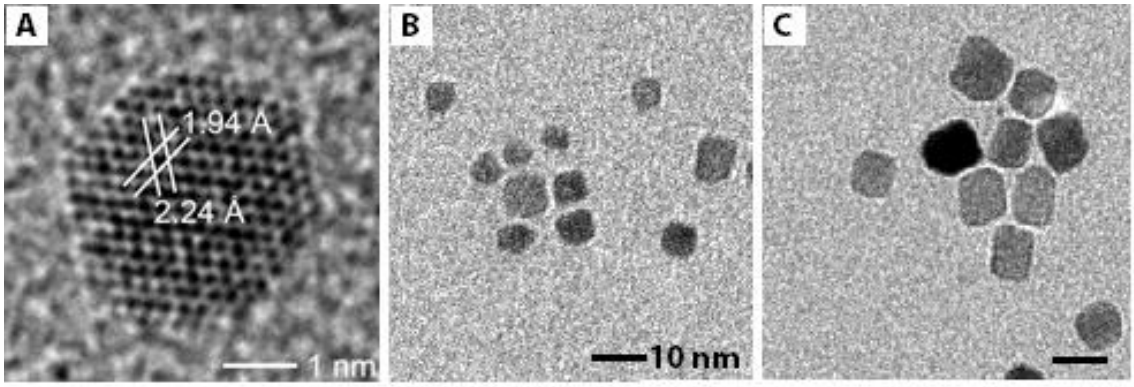

Figure 2.5. TEM images of nanoparticles from a typical photochemical-assisted synthesis taken at various time points after UV-vis irradiation: (A) atomic resolution TEM image of a single-crystal seed formed after 10 min of irradiation; (B) small cuboctahedral and truncated cubes after 45 min of irradiation; and (C) Pd cubic nanocrystals beginning to display an asymmetric shape after 2 h of irradiation due to the presence of atomic steps and terraces on the {100} faces. The scale bar is the same in (B) and (C). (Reprinted with permission from [53]. Copyright 2016 American Chemical Society.)

Once the Pd(0) atoms had reached a high enough concentration, they would undergo a classical nucleation process. Atomic resolution TEM from a typical reaction after 10 min of UV-vis irradiation revealed the presence of small, single-crystal seeds (Figure 2.5A). After 45 min of irradiation, the nucleates began to undergo facet-directed growth, generating small cuboctahedral crystals due to the presence of Br^- to cap the {100} faces (Figure 2.5B). Upon 2 h of irradiation, the cuboctahedra further grew into larger cubes, more closely resembling the nanocrystals in a product collected after a full, 3-h synthesis

(Figure 2.5C). However, in contrast to the relatively sharp cubes produced through thermal routes [36], the Pd nanocrystals formed in the present method, while cube-like, were also notably irregular and non-uniform, demonstrating the dominance of an asymmetric growth mode (Figure 2.6A), even though the XRD pattern confirmed the formation of pure Pd crystals (Figure 2.6B).

HRTEM was used to resolve the exact morphology of the final Pd nanocrystals produced through the photochemical method. Figure 2.7A shows a high-resolution image of a typical Pd nanocrystal. While the corners are truncated and rounded rather than being sharp, the side faces of the nanocrystals are of particular interest. Atomic resolution images (Figure 2.7B, C) of the areas enclosed by red boxes in Figure 2.7A reveal that the side faces are not comprised of the smooth {100} facets expected for a perfect nanocube, but instead form an irregular, almost concave structure that cannot be readily assigned to a single, high-index facet. Rather, the faces along the edges of the nanocrystal are composed of a series of random atomic steps and terraces at a decline normal to the (100) face.

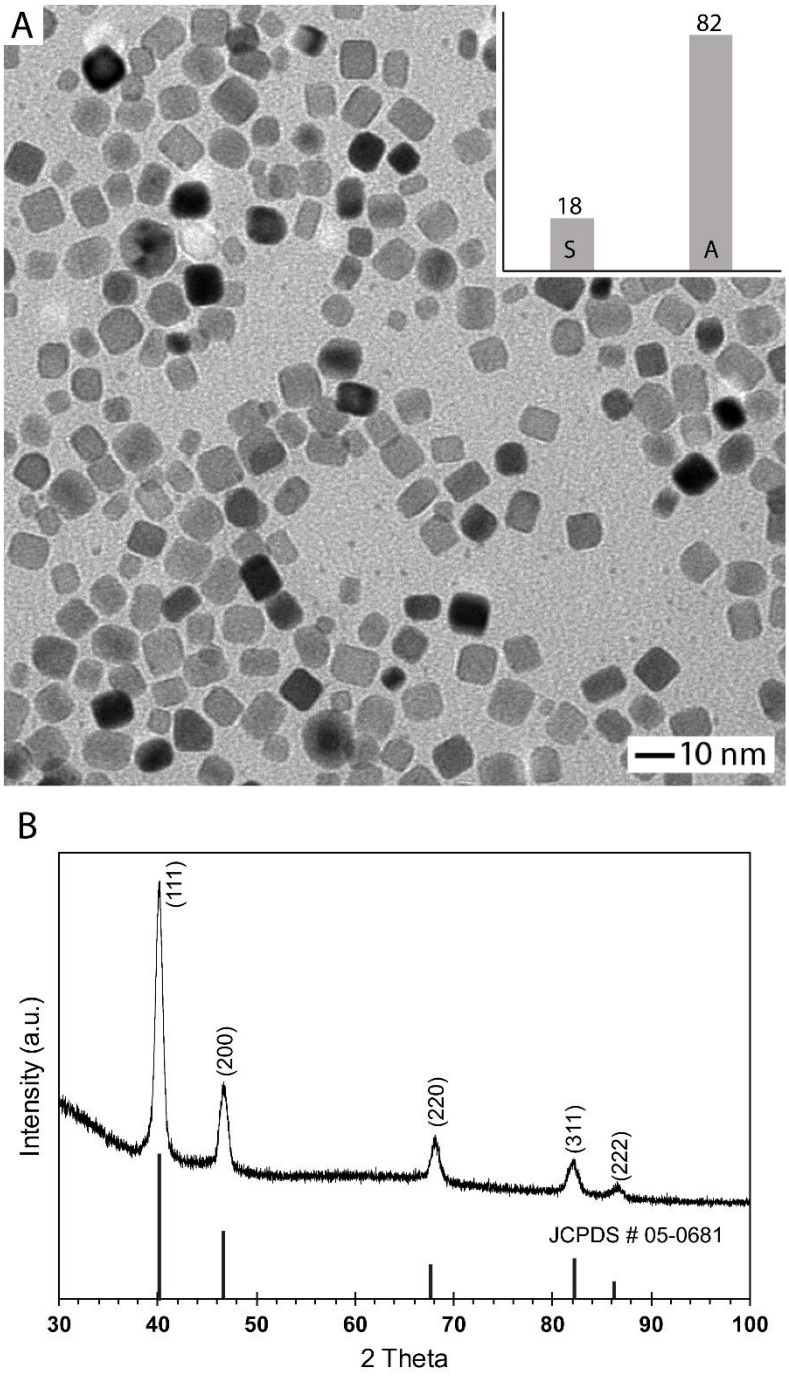

Figure 2.6. (A) TEM image of the Pd nanocrystals obtained from a typical photochemical synthesis, indicating a mixture of regular, symmetric cubes "S" with smooth side faces and asymmetric, cube-like particles "A" enriched with atomic steps and terraces. The distributions in the inset were calculated by examining 300 particles in a typical sample. Since the statistics were based on TEM images, the 18% should be considered as an upper limit for the symmetric cubes. (B) XRD pattern of a typical nanocrystal sample, matching a pure *fcc* Pd spectrum (JCPDS card No. 05-0681). (Reprinted with permission from [53]. Copyright 2016 American Chemical Society.)

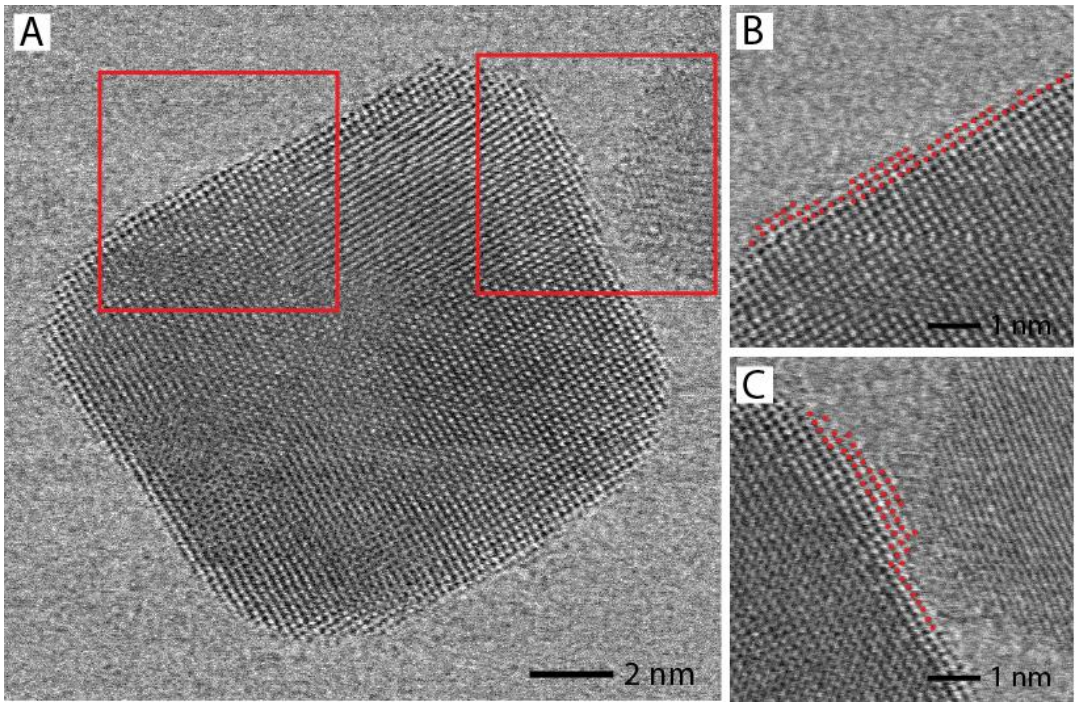

Figure 2.7. (A) HRTEM image of a typical Pd nanocrystal produced using the photochemical route. (B, C) Atomic-resolution TEM images of the faces marked by red boxes in (A), demonstrating the enrichment of atomic steps and terraces on the side faces. (Reprinted with permission from [53]. Copyright 2016 American Chemical Society.)

The observed asymmetric growth pattern can be better understood by examining the reaction conditions of the photochemical synthesis as compared to the traditional thermal method, and the difference in the relative rates for atom deposition (V_{dep}) and adatom surface diffusion (V_{dif}) [37,38]. It has been demonstrated that the rate of atom deposition can be controlled by tuning the reduction rate of metal ions in a reaction solution [39-41]. In contrast, V_{dif} is strongly dependent on the temperature of a synthesis, as illustrated in Figure 2.8. At a temperature of 80 °C typically used for the thermal synthesis of Pd nanocubes, V_{dif} is adequate to transport the newly deposited Pd adatoms across the {100} facets as the cuboctahedral seeds continue to grow in size. At room temperature, however, V_{dif} is greatly reduced compared to the case at an elevated temperature used for the thermally-activated synthesis. In a recent study, it was demonstrated that this drastically reduced V_{dif} at room temperature directly inhibits the ability of the newly deposited Pd adatoms to diffuse across the surface of a seed, limiting the active sites for growth to some

of the corners and further inducing an asymmetric growth mode [42]. As a result, the photochemical process always favors asymmetric growth, resulting in the formation of asymmetric and truncated cubes as shown in a typical synthesis. Furthermore, the sluggish V_{dif} slows diffusion of new adatoms from the {111} corners where they are deposited to the Br^- capped {100} faces. This in turn results in the high percentage of atomic steps and terraces observed under atomic resolution TEM (Figure 2.7), rather than smooth {100} facets. To generate more uniform cubes with a symmetric growth mode, the photochemical reduction process would need to be conducted at an elevated temperature, promoting faster adatom surface diffusion relative to the deposition process.

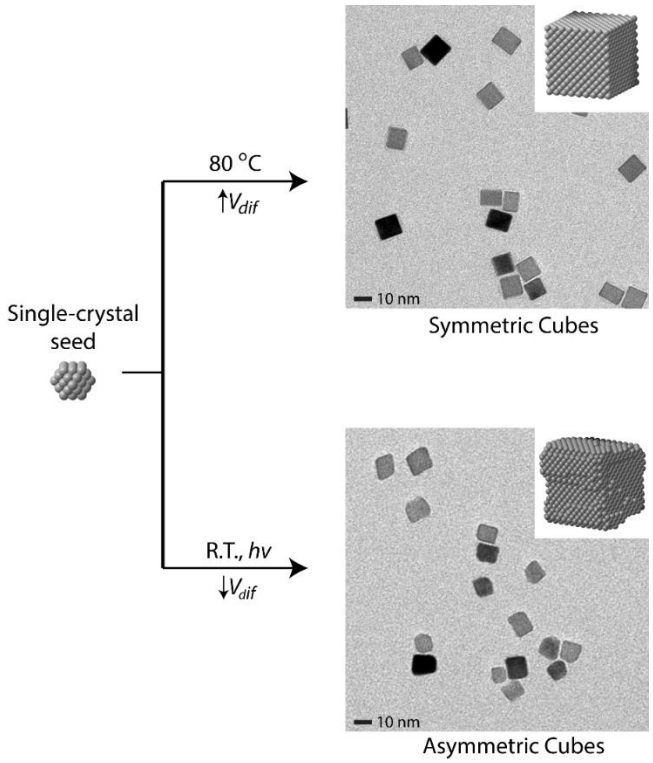

Figure 2.8. Schematic illustration demonstrating the effect of reaction temperature on the exact morphology taken by the Pd nanocrystals. At elevated temperatures, the rate of surface diffusion (V_{diff}) is high enough to move adatoms from the deposition sites across the {100} facets, producing symmetric cubes with sharp corners and smooth side faces. At room temperature, V_{diff} is substantially reduced, such that adatoms cannot readily diffuse across the side faces of a cube, resulting in the formation of Pd nanocubes enriched with atomic steps and terraces. (Reprinted with permission from [53]. Copyright 2016 American Chemical Society.)

I also investigated the effect of post-synthetic heat treatment on the asymmetric Pd cubes in an attempt to determine if the shape could be controllably altered under thermal annealing. It was found that the highly terraced faces on the original Pd particles could be transformed during thermal treatment under appropriate conditions (Figure 2.9). In an effort to understand the stability of these irregular facets, I heated the Pd nanocrystals with atomic steps and terraces to 80 °C in water, the typical temperature used to synthesize sharp Pd cubes. However, even after 3 h of heating, the original nanocrystals remained stable and maintained the same morphology, showing no sign of surface atom diffusion (Figure 2.9B). The nanocrystals were transferred into ethylene glycol and heated at 130 °C for 3 h. At this temperature, the nanocrystals underwent surface adatom diffusion and structural transformation; however, they evolved into spherical, Wulff-like structures with a mixture of various low-index facets (Figure 2.9C). The Wulff structure is a morphology that most single-crystal metals are known to adopt in order to minimize the total surface free energy when no capping agents are present to direct and stabilize growth. In an effort to generate sharp cubes, I conducted the same heating process at 130 °C for 3 h but in the presence of excess Br^-. With excess Br^- available to selectively cap the {100} facets and stabilize the cubic shape, I was able to induce surface transformation into truncated cubes (Figure 2.9D). The Pd adatoms initially present on the atomic steps and terraces were able to readily diffuse across the surface, forming cubes with rounded corners but smooth faces.

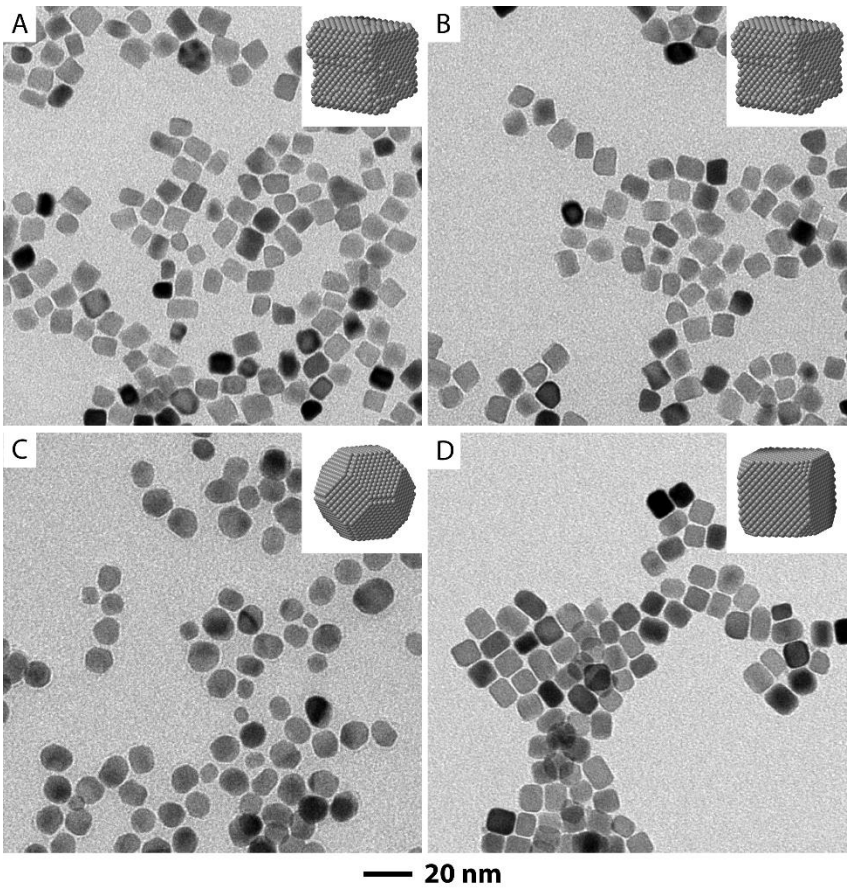

Figure 2.9. TEM images showing the effect of post-synthesis thermal annealing on the shape of the Pd cubes with atomic steps and terraces. (A) Initial nanocrystals synthesized through the standard photochemical protocol. (B) Nanocrystals from (A) after annealing in water at 80 °C for 3 h, showing preservation of shape and morphology. (C) Nanocrystals from (A) after annealing in ethylene glycol at 130 °C for 3 h, showing a loss of the initial cubic shape and atomic steps and terraces as surface diffusion of adatoms readily occurs, leading to the formation of multi-faceted Wulff structures with a lower total surface free energy. (D) Nanocrystals from (A) after annealing in ethylene glycol with excess KBr at 130 °C for 3 h, showing their transformation to truncated cubes with smooth faces. (Reprinted with permission from [53]. Copyright 2016 American Chemical Society.)

Many studies have suggested that the high surface energy associated with low-coordination atomic sites may contribute toward improved catalytic performance [43-45]. However, this structure-property relationship is not well defined, and is highly dependent on both the catalytic material and the targeted reaction. Computational modeling is often required to understand the energetics of the binding between the active sites and the catalytic reactants or intermediates [46-47]. In the case of low-coordination active sites,

the associated energy between the atomic site and the binding species may increase relative to the low index sites, leading to one of two results: the increased binding energy may favorably facilitate reactive species binding and improve the subsequent catalytic reaction, or it may cause the active site to "overbind" to reactant/intermediate species and fall into a thermodynamic sink [48-49]. Overbinding results in a dramatic decrease in the measured catalytic performance, similar to catalyst poisoning. Short of employing computationally expensive calculations, determining how high energy active sites will perform requires case-by-case testing. Therefore, to better evaluate the effect of the Pd cubes with atomic steps and terraces on potential applications, I evaluated the catalytic performance using FAO as a model reaction. Prior studies on Pd single crystal catalysts have shown a facet dependence for FAO, with cubes enclosed by {100} facets displaying enhanced activity over their octahedral counterparts enclosed by {111} facets [50]. For a standard comparison, I synthesized 12-nm Pd cubes (Figure 2.10A) with sharp corners and smooth faces through a traditional thermal method. I then compared the sharp 12-nm cubes to a typical sample of Pd cubes with atomic steps and terraces (Figure 2.10B), and to a sample of truncated cubes with smooth faces (Figure 2.10C) formed through the thermal transformation of the photochemical cubes.

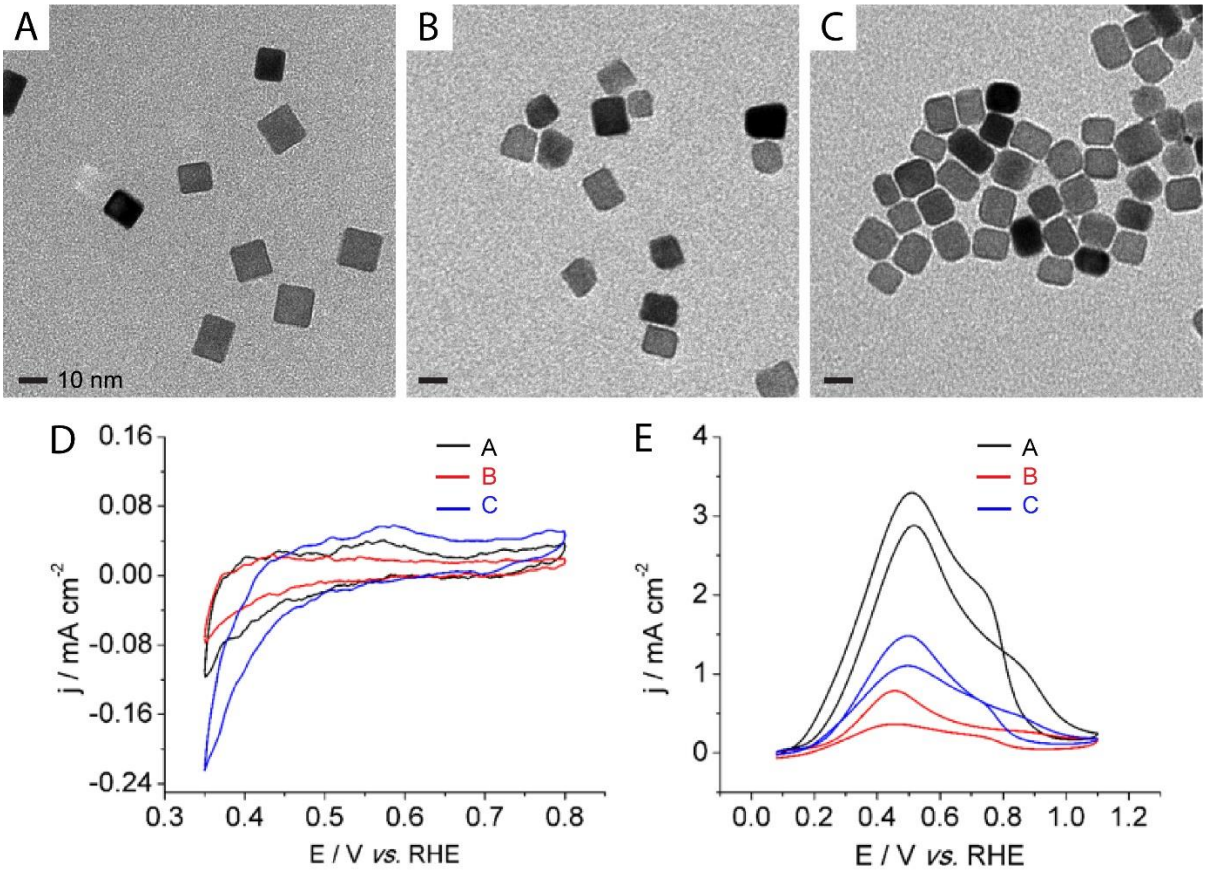

Figure 2.10. TEM images of different types of Pd nanocrystals that were used as catalysts for formic acid oxidation, and their catalytic results. (A) Pd nanocubes with sharp corners and smooth faces that were prepared using the traditional thermal method. (B) Pd nanocubes with atomic steps and terraces that were synthesized through the photochemical route. (C) Pd nanocubes with truncated corners and smooth faces that were obtained *via* thermal transformation of (B) at 130 °C in the presence of excess KBr. The scale bar is the same for A-C. (D) CVs of the catalysts obtained in a N_2-saturated aqueous solution containing H_2SO_4 and $CuSO_4$. Scanning speed = 20 mV s^{-1}. The currents were normalized to the geometric area of the glassy carbon electrode (0.196 cm^2). (E) CVs of the catalysts obtained in a N_2-saturated solution containing 0.1 M $HClO_4$ and 0.5 M HCOOH. Scanning speed = 50 mV s^{-1}. The currents were normalized to the electrochemical surface areas of the corresponding catalysts derived from the charges for the underpotential deposition of Cu. (Reprinted with permission from [53]. Copyright 2016 American Chemical Society.)

Table 2.1 Comparison of formic-acid oxidation activities for catalysts based on different types of Pd nanocrystals shown in Figure 1.10, A-C. (Reprinted with permission from [53]. Copyright 2016 American Chemical Society.)

Catalyst	Specific ECSA (m^2 g^{-1}_{Pd})	SA at 0.4 V (mA cm^{-2})	MA at 0.4 V (A mg^{-1}_{Pd})	Anodic peak potential (V)	SA at anodic potential (mA cm^{-2})	MA at anodic potential (A mg^{-1}_{Pd})
1	11.38 ± 1.10	1.93 ± 0.15	0.22 ± 0.01	0.52 ± 0.01	2.90 ± 0.29	0.33 ± 0.01
2	13.38 ± 2.39	0.67 ± 0.10	0.09 ± 0.002	0.46 ± 0.01	0.79 ± 0.13	0.11 ± 0.003
3	7.43 ± 1.02	1.10 ± 0.17	0.08 ± 0.001	0.50 ± 0.01	1.48 ± 0.26	0.11 ± 0.001

The results of the electrochemical measurements are shown in Figure 2.10D and E. Figure 2.10D shows the cyclic voltammograms (CVs) of the three catalytic samples for Cu underpotential deposition. The ECSAs of the catalysts were determined from the charges associated with stripping a UPD monolayer of Cu from the catalyst surfaces. The specific ECSAs were then calculated by normalizing the measured ECSAs to the mass of Pd in each sample; all calculated values are summarized in Table 2. Figure 2.10E shows the cyclic voltammograms of the catalysts for FAO, normalized to their respective ECSAs. As the anodic peak potential for FAO can shift depending on the surface structure of the nanocrystals involved, I calculated and compared the specific activities (SAs) at the respective anodic peak potentials for each sample. The FAO measurements yielded a clear trend in the calculated SAs. The 12-nm Pd sharp cubes yielded the highest SA (2.90 mA cm^{-2} at anodic peak potential). In contrast, the Pd cubes with atomic steps and terraces demonstrated the poorest SA (0.79 mA cm^{-2} at anodic peak potential, 3.6 times lower than the sharp cubes). Finally, the thermally transformed photochemical cubes with smooth faces but truncated corners yielded a calculated SA that was higher than the terraced cubes, but lower than the cubes with sharp corners (1.48 mA cm^{-2} at anodic peak potential, 1.9 times higher than the terraced cubes and 1.9 times lower than the sharp cubes). This trend can be rationalized by the differences in the surface and electronic structures between the three catalytic samples. Contrary to literature that has reported enhanced FAO activity on

some nanocrystals with high index facets [51,52], here I believe the high proportion of low-coordinated surface atoms from the atomic steps and terraces is directly responsible for the large drop in the measured peak anodic SA as compared to the sharp cubes.

Interestingly, when the photochemically-synthesized catalysts are placed into oxidative environments (oxygen saturated electrolyte, or held at FAO oxidative potentials), there appear to be no dramatic or immediate changes to the irregular surface structure (Figure 2.11), even after an hour of oxidative stress. This suggests that the persistent low coordination sites present on the faces are largely responsible for the significant decrease in observed FAO activity. Rather than enhancing the performance, the altered electronic structure of these high energy sites instead appears to decrease the catalytic activity. I believe this is due to overbinding of the active sites with the formic acid or a reactive intermediate, resulting in dramatically reduced catalytic conversion and the apparent drop in catalytic performance. With this in mind, I can therefore attribute the enhancement in SA seen in the thermally transformed cubes to the sharpening of the cubic faces into true {100} facets devoid of atomic steps, ledges, and low-coordination sites. Conversely, though this transformation improves the SA relative to the photochemically-synthesized cubes, the true cubes with sharp corners still demonstrate the best catalytic performance. In agreement with earlier studies, this can be rationalized due to the highly truncated corners in the thermally-transformed sample [50]. While the smooth {100} facets enhance activity, the presence of highly truncated corners and therefore a mixture of both {100} and {111} facets on the nanocatalysts reduces the anodic SA relative to the true, sharp cubes. This lends credit to the experimentally observed pattern wherein single crystal Pd catalysts with the highest proportion of {100} facets exhibit the highest activity toward FAO. These results demonstrate a clear correlation between the surface structure of nanocrystals and their measured catalytic performance, with important implications for future work done on nanocatalysts with a high proportion of low-coordination active sites.

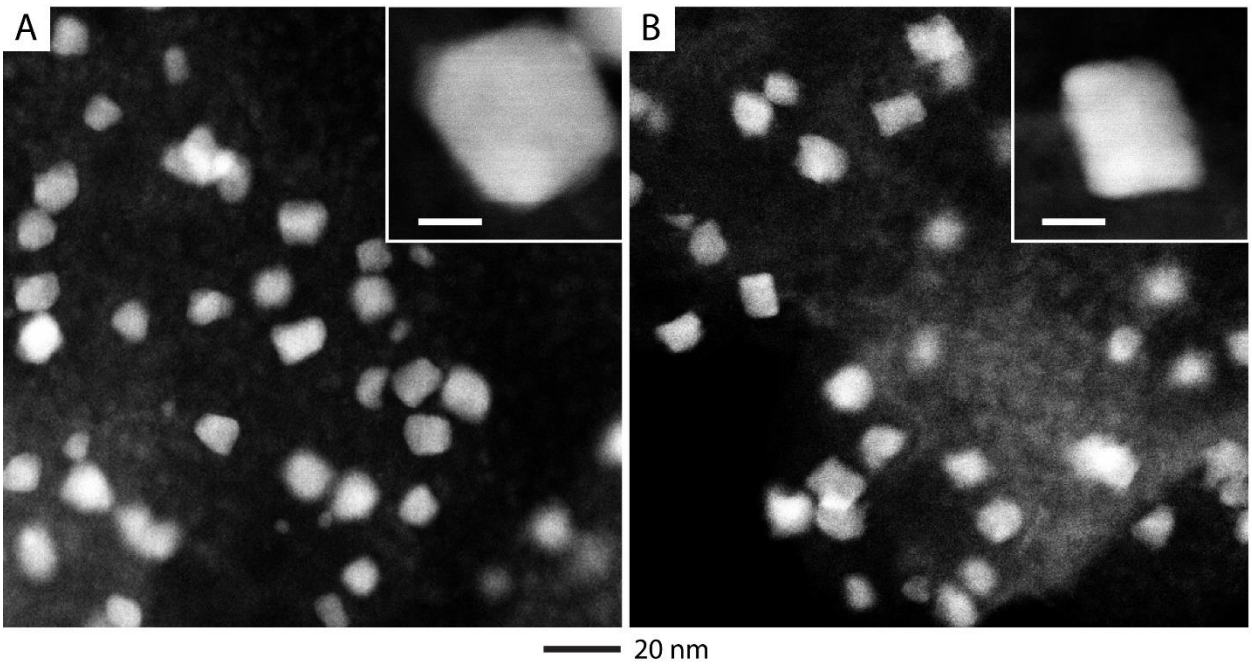

Figure 2.11. High-angle annular dark field scanning TEM (HAADF-STEM) images of Pd cubes from a typical photochemical synthesis loaded onto carbon support after having been (A) immersed into O_2-satured FAO electrolyte solution and kept saturated with O_2 gas for 1 h, and after (B) immersed into N_2-saturated FAO electrolyte solution and held at a potential of 0.45 V for 1 h. Notably, the irregular facets of the Pd nanocrystals appear preserved even after subjected to oxidation condition, rather than rounding or smoothing into low index facets. The high-resolution images of the nanocrystal in each inset possess a scale bar of 5 nm. (Reprinted with permission from [53]. Copyright 2016 American Chemical Society.)

2.3 Conclusion

In summary, I have successfully demonstrated a facile route to the photochemical synthesis of Pd nanocrystals at room temperature. The key to this synthesis was two-fold, relying on the use of a strongly irradiating light source as well as room temperature reaction conditions. The strong UV-vis irradiation from a Hg lamp was found to be critical to both the generation of seeds, as well as their subsequent growth at room temperature. Simultaneously, because of the inherently low surface diffusion rate of Pd adatoms at room temperature, the nanocrystals evolved into truncated cubes with an asymmetrical shape, naturally forming atomic steps and terraces on their faces rather than smooth {100} facets

as found at elevated reaction temperatures. This photochemical method opens an avenue toward the generation of Pd nanocrystals at room temperature, and the investigation of novel morphologies characterized by atomic steps and terraces rather than the low-index facets typically generated at elevated temperatures. Using formic acid oxidation as a model catalytic reaction, I compared the terraced nanocubes to the traditional nanocubes with smooth {100} facets. My results indicate a clear trend wherein the catalytic performance was enhanced by the presence of smooth {100} facets, but decreased with an increasing proportion of low-coordination surface atoms. This can be attributed to the overbinding of reactive species to the high energy sites. Contrary to prior reports on the benefits of high-index nanocrystals, my results highlight the importance of fully investigating the impact of low-coordination active sites on catalytic applications.

2.4 Experimental Section

Chemicals and Materials. Sodium tetrachloropalladate(II) (Na_2PdCl_4, 98%), potassium bromide (KBr, >99%), potassium chloride (KCl, >99%), L-ascorbic acid (AA, >99%), poly(vinyl pyrrolidone) (PVP, $M_w \approx 55{,}000$), and ethylene glycol (EG) were all purchased from Sigma-Aldrich and used as received. Ethanol (200 proof ACS grade) was obtained from VWR. All aqueous solutions were prepared using deionized (DI) water with a resistivity of 18.2 MΩ·cm. All syntheses were carried out in borosilicate vials (6 dram, VWR, transparent >300 nm) under vigorous magnetic stirring.

Photochemical Synthesis of Pd Nanocubes. For a typical synthesis, 57 mg of Na_2PdCl_4 was dissolved into 3 mL of water over 2 h of vigorous shaking or stirring. I chose to use Na_2PdCl_4 as my metal salt precursor for this reaction, as it can be readily obtained from commercial sources, and is substantially more cost effective to use than its bromo-substituted counterpart, K_2PdBr_4. The solution was added into a glass vial that already contained 8 mL of an aqueous solution of 105 mg of PVP, 60 mg of AA, 185 mg of KCl, and 400 mg of KBr. The vial was then sealed and placed against a double-walled quartz

immersion well in a water bath. The light source (medium pressure Hg vapor arc lamp, Ace Glass) was hosted inside the quartz immersion well. The distance between the light source and the reaction solution was approximately 2 cm. Temperatures of both the water bath and the circulating water from the immersing well were maintained at 23±3 ^{o}C throughout the synthesis by controlling the flow rate of water through the immersion well. The reaction was then magnetically stirred under UV-vis irradiation for 3 h. The final product was collected *via* centrifugation at 55,000 rpm for 30 min, washed three times with water to remove excess PVP, and then re-dispersed in 11 mL of water. A control reaction was also run under the same conditions except for the use of pure K_2PdBr_4 instead of Na_2PdCl_4 as the precursor, and the same experimental results were confirmed.

Thermal Transformation of the Pd Nanocubes. For a typical thermal transformation test conducted at 80 °C, the Pd nanocubes were heated under magnetic stirring at 80 °C for 3 h. The suspension was then cooled to room temperature, and centrifuged at 55,000 rpm for 30 min. The collected pellet was re-dispersed in 11 mL of water for further analysis.

For thermal transformation tests conducted at 130 °C, the Pd nanocubes were first transferred into 11 mL of EG. For experiments involving excess KBr, 400 mg of KBr was also added to the EG suspension and allowed to dissolve through sonication. The samples were then heated under magnetic stirring at 130 °C for 3 h. After cooling to room temperature, the final product was collected by centrifuging the sample at 55,000 rpm for 30 min, and washed twice with water. The pellet was collected and re-dispersed in 11 mL of water for further analysis.

Formic Acid Oxidation (FAO). To prepare nanocrystal samples for FAO measurements, samples were attached to a carbon support and the surfaces were cleaned of remnant PVP and Br^{-} through an acetic acid treatment. Ketjen black carbon support (EC-300J) was first suspended in water to a concentration of 1 mg mL^{-1} by sonicating in ice water for 3 h. To create the ink for electrocatalysis, the selected Pd nanocrystal sample was dropwise added into a carbon suspension to achieve 40% Pd loading by weight. The

ink was sonicated for 2 h on ice water. The suspension was then centrifuged at 12,000 rpm for 20 min to obtain a pellet. To clean the surface of the Pd nanocrystals attached to the carbon support, I suspended the pellet into acetic acid and heated the sample under magnetic stirring for 3 h at 60 °C. After the acetic acid treatment, the ink was centrifuged at 12,000 rpm for 20 min to collect a pellet, and washed seven times with ethanol, and three times with water. The pellet was dispersed in a mixture containing DI water, isopropanol (IPA), and Nafion (5%) (V_{water}:V_{IPA}:$V_{5\%Nafion}$ = 4:1:0.05) to form a 1 mg mL^{-1} ink under ultrasonication for 30 min. The concentration of Pd in the final ink dispersion was determined by ICP-MS. 10 μL of the suspension was then dropped onto a pre-cleaned glassy carbon electrode (Pine Research Instrumentation) and dried at room temperature and under ambient conditions. A Hydroflex hydrogen reference electrode (ET070, Edaq Inc.) and a Pt wire were used as the reference and counter electrodes, respectively. The potentials are given with reference to the reversible hydrogen electrode (RHE). In order to ensure full removal of any surfactants or capping agents that could adsorbed to the surface of the Pd catalyst (e.g. PVP or Br^-), the electrical potential was held at -0.05 V for 60 s. To obtain the FAO activity, the catalyst was cycled between 0.08 and 1.1 V (versus RHE) for two cycles in a N_2-saturated aqueous solution that contained $HClO_4$ (0.1 M) and HCOOH (2 M) at a scan rate of 50 mV s^{-1}. The Cu underpotential deposition (UPD) was conducted in an aqueous solution that contained H_2SO_4 (50 mM) and $CuSO_4$ (50 mM). The electrochemical surface areas (ECSAs) were obtained from the charges associated with the stripping of Cu_{UPD} on the Pd nanocrystals by assuming 420 μC cm^{-2} for a full monolayer coverage of Cu on Pd enclosed by {100} facets. For stability tests of the photochemically-synthesized Pd catalyst, the catalyst electrode was held at 0.45 V in an N_2-saturated solution containing $HClO_4$ (0.1 M) and HCOOH (2 M) for 1 h. For stability tests in an oxygen rich environment, the catalyst electrode was immersed into an O_2-saturated solution containing $HClO_4$ (0.1 M) and HCOOH (2 M) for 1 h. All the electrochemical measurements were conducted with a CHI600E potentiostat (CH Instrument).

Instrumentation. Samples for TEM were prepared by placing a drop of the nanocrystal sample (suspended in water) on a carbon-coated copper grid and drying under ambient conditions. TEM images were taken using a Hitachi HT 7700 microscope operated at 120 kV. Samples for HRTEM were prepared by further washing the sample with water another 5-7 times, and then drop casting the sample onto a holey carbon-coated copper grid with ultrathin carbon. HRTEM imaging was performed using a cold field-emission Hitachi HD 2700 aberration-corrected microscope operated at 200 kV. Atomic resolution image for supplemental information was acquired using cold field-emission JEOL 4000EX aberration-corrected microscope operated at 350 kV. The UV-vis spectra were obtained using a spectrometer from Perkin Elmer (Lambda 750). Inductively coupled plasma mass spectrometry (ICP-MS, NexION 300Q, Perkin Elmer) was used to determine the Pd content in each sample.

2.5 Notes to Chapter 2

Part of this chapter is adapted from the paper "A Photochemical, Room-temperature, and Aqueous Route to the Synthesis of Pd Nanocubes Enriched with Atomic Steps and Terraces on the Side Faces" published in the *Chemistry of Materials* [53].

2.6 References

[1] Shu, J.; Grandjean, B. P. A.; Neste, A. V.; Kaliaguine, S. *Can. J. Chem. Eng.* **1991,** *69*, 1036-1060.

[2] Miyaura, N.; Suzuki, A. *Chem. Rev.* **1995,** *95*, 2457-2483.

[3] Kwon, M. S.; Kim, N.; Park, C. M.; Lee, J. S.; Kang, K. Y.; Park, J. *Org. Lett.* **2005,** *7*, 1077-1079.

[4] Yun, S.; Ted Oyama, S. *J. Membr. Sci.* **2011,** *375*, 28-45.

[5] Kim, S.-W.; Park, J.; Jang, Y.; Chung, Y.; Hwang, S.; Hyeon, T.; Kim, Y. W. *Nano Lett.* **2003,** *3*, 1289-1291.

[6] Ramirez, E.; Jansat, S.; Philippot, K.; Lecante, P.; Gomez, M.; Masdeu-Bultó, A. M.; Chaudret, B. *J. Organomet. Chem.* **2004,** *689*, 4601-4610.

[7] Piao, Y.; Jang, Y.; Shokouhimehr, M.; Lee, I. S.; Hyeon, T. *Small* **2007,** *3*, 255-260.

[8] Xiong, Y.; Xia, Y. *Adv. Mater.* **2007,** *19*, 3385-3391.

[9] Niu, W.; Zhang, L.; Xu, G. *ACS Nano* **2010,** *4*, 1987-1996.

[10] Wang, Y.; Xie, S.; Liu, J.; Park, J.; Huang, C. Z.; Xia, Y. *Nano Lett.* **2013,** *13*, 2276-2281.

[11] Peng, H.-C.; Li, Z.; Aldahondo, G.; Huang, H.; Xia, Y. *J. Phys. Chem. C* **2016,** *120*, 11754-11761.

[12] Xia, Y.; Gilroy, K. D.; Peng, H.-C.; Xia, X. *Angew. Chem., Int. Ed.* **2017,** *56*, 60-95.

[13] Mu, X.-d.; Evans, D. G.; Kou, Y. *Cat. Lett.* **2004,** *97*, 151-154.

[14] Nadagouda, M. N.; Varma, R. S. *Green Chem.* **2008,** *10*, 859-862.

[15] Fan, F.-R.; Attia, A.; Sur, U. K.; Chen, J.-B.; Xie, Z.-X.; Li, J.-F.; Ren, B.; Tian, Z.-Q. *Crys. Growth Des.* **2009,** *9*, 2335-2340.

[16] Grzelczak, M.; Liz-Marzan, L. M. *Chem. Soc. Rev.* **2014,** *43*, 2089-2097.

[17] Sakamoto, M.; Fujistuka, M.; Majima, T. *J. Photochem. Photobiol. C: Photochem. Rev.* **2009,** *10*, 33-56.

[18] Kim, F.; Song, J. H.; Yang, P. *J. Am. Chem. Soc.* **2002,** *124*, 14316-14317.

[19] Callegari, A.; Tonti, D.; Chergui, M. *Nano Lett.* **2003,** *3*, 1565-1568.

[20] Millstone, J. E.; Hurst, S. J.; Métraux, G. S.; Cutler, J. I.; Mirkin, C. A. *Small* **2009,** *5*, 646-664.

[21] Borgarello, E.; Serpone, N.; Emo, G.; Harris, R.; Pelizzetti, E.; Minero, C. *Inorg. Chem.* **1986,** *25*, 4499-4503

[22] Boitsova, T. B.; Gorbunova, V. V.; Voronin, Y. M. *J. Opt. Technol.* **2001,** *68*, 789-793.

[23] Lifanova, E. A.; Gorbunova, V. V.; Boitsova, T. B. *Russ. J. Appl. Chem.* **2009,** *82*, 915-917.

[24] Chen, S. F.; Li, J. P.; Qian, K.; Xu, W. P.; Lu, Y.; Huang, W. X.; Yu, S. H. *Nano Res.* **2010,** *3*, 244-255.

[25] Kundu, S.; Wang, K.; Lau, S.; Liang, H. *J. Nanopart. Res.* **2010,** *12*, 2799-2811.

[26] McGilvray, K. L.; Decan, M. R.; Wang, D.; Scaiano, J. C. *J. Am. Chem. Soc.* **2006,** *128*, 15980-15981.

[27] Scaiano, J. C.; Stamplecoskie, K. G.; Hallett-Tapley, G. L. *Chem. Commun.* **2012,** *48*, 4798-4808.

[28] Tikekar, R. V.; Anantheswaran, R. C.; Elias, R. J.; LaBorde, L. F. *J. Agric. Food Chem.* **2011,** *59*, 8244-8248.

[29] Elding, L. I. **1975,** *15*, L9-L11

[30] Richens, D. T. *Chem. Rev.* **2005,** *105*, 1961-2002.

[31] Timoshkin, A. Y.; Kudrev, A. G. *Russ. J. Inorg. Chem.* **2012,** *57*, 1362-1370.

[32] Elding, L. I. *Inorg. Chim. Acta* **1972,** *6*, 647-651.

[33] Elding, L. I.; Olsson, L. F. *J. Phys. Chem.* **1978,** *82*, 69-74.

[34] Srivastava, S. C.; Newman, L. *Inorg. Chem.* **1966,** *5*, 1506-1510.

[35] Feldberg, S.; Klotz, P. *Inorg. Chem.* **1972,** *11*, 2860-2865.

[36] Lim, B.; Jiang, M.; Tao, J.; Camargo, P. H. C.; Zhu, Y.; Xia, Y. *Adv. Funct. Mater.* **2009,** *19*, 189-200.

[37] Xia, Y.; Xia, X.; Peng, H.-C. *J. Am. Chem. Soc.* **2015,** *137*, 7947-7966.

[38] Zhu, C.; Zeng, J.; Tao, J.; Johnson, M. C.; Schmidt-Krey, I.; Blubaugh, L.; Zhu, Y.; Gu, Z.; Xia, Y. *J. Am. Chem. Soc.* **2012,** *134*, 15822-15831.

[39] Biacchi, A. J.; Schaak, R. E. *ACS Nano* **2011,** *5*, 8089-8099.

[40] Xie, S.; Choi, S.-I.; Lu, N.; Roling, L. T.; Herron, J. A.; Zhang, L.; Park, J.; Wang, J.; Kim, M. J.; Xie, Z.; Mavrikakis, M.; Xia, Y. *Nano Lett.* **2014,** *14*, 3570-3576.

[41] Zhang, L.; Niu, W.; Xu, G. *Nano Today* **2012,** *7*, 586-605.

[42] Peng, H.-C.; Park, J.; Zhang, L.; Xia, Y. *J. Am. Chem. Soc.* **2015,** *137*, 6643-6652.

[43] Tian, N.; Zhou, Z.-Y.; Sun, S.-G.; Ding, Y.; Wang, Z. L. *Science* **2007,** *316*, 732-735.

[44] Tian, N.; Zhou, Z.-Y.; Yu, N.-F.; Wang, L.-Y.; Sun, S.-G. *J. Am. Chem. Soc.* **2010,** *132*, 7580-7581.

[45] Xie, X.; Gao, G.; Pan, Z.; Wang, T.; Meng, X.; Cai, L. *Sci. Rep.* **2015,** *5*, 8515.

[46] Falicov, L. M.; Somorjai, G. A. *Proc. Natl. Acad. Sci.* **1985,** *82*, 2207-2211.

[47] Greeley, J.; Nørskov, J. K.; Mavrikakis, M. *Ann. Rev. Phys. Chem.* **2002,** *53*, 319-348.

[48] Liu, C.; Cundari, T. R.; Wilson, A. K. *J. Phys. Chem. C* **2012,** *116*, 5681-5688.

[49] Holby, E. F.; Taylor, C. D. *Sci. Rep.* **2015,** *5*, 9286.

[50] Jin, M.; Zhang, H.; Xie, Z.; Xia, Y. *Energy Environ. Sci.* **2012,** *5*, 6352-6357.

[51] Hoshi, N.; Nakamura, M.; Kida, K. *Electrochem. Commun.* **2007,** *9*, 279-282.

[52] Jin, M.; Zhang, H.; Xie, Z.; Xia, Y. *Angew. Chem., Int. Ed.* **2011,** *50*, 7850-7854.

[53] Vara, M.; Lu, P.; Lee, C.-T.; Xia, Y. *Chem. Mat.* **2017,** *29*, 4563-4571.

CHAPTER 3

FACILE SYNTHESIS OF PALLADIUM CONCAVE NANOCUBES: FROM KINETIC ANALYSIS TO MECHANISTIC UNDERSTANDING AND RATIONALLY DESIGNED PROTOCOL

3.1 Introduction

Over the last two decades, tremendous progress has been made towards the facile and reliable synthesis of Pd nanocrystals as driven by their remarkable catalytic properties. In particular, recent advancements in mechanistic understandings have enabled the synthesis of Pd nanocrystals with a myriad of controlled shapes or morphologies, with notable examples including cubes, octahedra, decahedra, icosahedra, plates, dendrimers, and many derivatives thereof [1-7]. More recently, there has been a strong interest in Pd nanocrystals featuring high-index facets and/or symmetry-broken morphologies. Many preliminary studies have demonstrated that high-index facets could exhibit dramatically enhanced catalytic performance across a wide array of reactions [8-14]. However, the rational design of methods for generating such geometrically complex and thermodynamically unfavorable structures remains difficult and the protocols often involve multi-pot or multi-step reactions. The protocol most frequently reported in literature is through seed-mediated growth, in which an initial synthesis is employed to produce the intended colloidal nanocrystal seeds (*e.g.*, single-crystal, singly-twinned, multiply-twinned, or stacking-fault-lined), and the seeds are then collected and used for subsequent growth under substantially different reaction conditions to enable a kinetically-controlled product [15, 16]. The essence of seed-mediated growth is to isolate growth from nucleation, which are often directed by vastly different reaction kinetics in the cases of complex and thermodynamically unfavorable structures. Upon separation, the initial synthesis only targets the nucleation process with a focus on the internal twin structure of the seeds

whereas the second step tunes both the metal salt reduction kinetics and the surface adatom diffusion rate to obtain a kinetically controlled rather than a thermodynamically-driven product [17, 18]. An alternative approach reported in the literature is to couple reduction-based growth with oxidative etching [19-21]. In this case, reduction-based growth leads to the initial formation of nanocrystals but is followed by oxidative etching. Oxidative etching often selectively attacks and etches away certain high-energy sites or facets on the nanocrystal, leaving behind unique, high-index surfaces. In general, it is still difficult to tune oxidative etching in a controllable way across the entire population of noble-metal nanocrystals.

Both syntheses based on seed-mediated growth and oxidative etching often require multiple steps to generate the desired nanocrystals, leading to greater complexities and difficulties in fine tuning and controlling all the steps involved, lower total yield, and increased time and costs constraints. In addition, both methods are typically run at elevated temperatures, which can lead to additional complexities due to thermal inhomogeneity, which is not readily translatable when scaling-up the synthesis. Ideally, one would like to have a one-pot process that can generate metal nanocrystals covered by high-index facets at room temperature and under one single set of conditions. The key is to program the reduction kinetics to suit the nucleation and growth, respectively.

Here I introduce a rationally designed protocol for the one-pot, room-temperature synthesis of Pd concave nanocubes. In searching the literature, I mainly found seed-mediated, multi-pot methods for producing such nanocrystals enclosed by high-index facets [22-24]. While there were several reports on the use of a one-pot approach, the syntheses all involved the use of elevated temperatures, which are unfavorable for scale-up [25-27]. Additionally, many of these studies were focused on catalytic applications, only with limited investigations into the kinetic mechanisms that drive and control the formation of concave structures. I believe that the rational design of a one-pot, room-temperature protocol for such a synthesis will substantially expand the list of Pd concave

nanocrystals with high-index facets and enhance the scale-up potential for industrial application. The success of my synthesis relies on the following key mechanistic understandings: *i*) the use of room temperature, and its pronounced impact on both reduction and surface diffusion kinetics; and *ii*) the use of an appropriate reducing agent, sodium ascorbate, to pair with the metal precursor $PdBr_4^{2-}$. By harnessing the unique reduction features of this one-pot system, I was able to first generate single-crystal Pd seeds through a solution reduction pathway, followed by autocatalytic surface reduction for seed-mediated growth. The sluggish surface diffusion rates intrinsic to room temperature resulted in a symmetry-breaking growth mode and pile-up of new atoms at the corner and/or edge sites on the seeds, generating asymmetric Pd concave nanocubes with an average separation of 18 nm between adjacent corners. It is the two separate reduction regimes that allowed for the production of concave nanocubes through a one-pot, room-temperature protocol, which, to my knowledge, has not been reported in the literature.

3.2 Results and Discussion

Figure 3.1 shows a schematic illustration of my general strategy employed for the room-temperature synthesis of Pd concave cubes. The synthesis is built upon a modification to the conventional protocol used for the production of Pd nanocubes at an elevated temperature of 80 ºC [1], with the involvement of a Pd(II) precursor, a reducing agent, excess Br^- ions as a facet-selective capping agent, and a colloidal stabilizer. I believe both the nucleation and growth are critically dependent on the room-temperature conditions, which will strongly affect the reduction kinetics. First, a sufficiently strong reducing agent must be employed to induce the formation of single-crystal nuclei. Following seed formation, the reducing rate must be in the proper window so as to both avoid multiple nucleation events, and allow for controllable growth. By using excess Br^- in the reaction solution to passivate the {100} facets of the single-crystal seeds, I can promote growth in the ⟨111⟩ directions, which would normally generate cubes. However,

given the depressive effect of the room-temperature conditions on both adatom surface diffusion rates as well as activation of growth sites, it is expected that rather than growing into smooth, {100} facet decorated cubes, the seeds evolve into concave cubes.

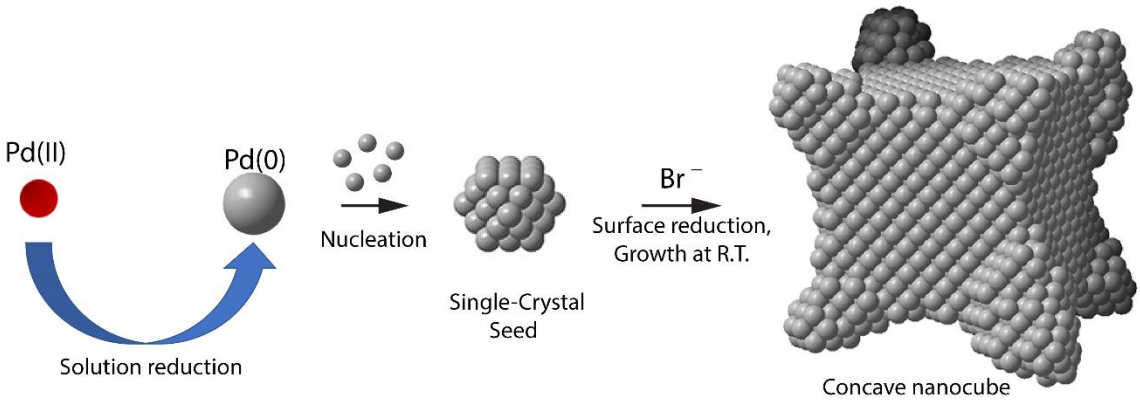

Figure 3.1. Schematic illustration of the proposed mechanism by which concave nanocubes are formed through a one-pot, two-step method. First, solution reduction occurs as the Pd(II) species are reduced to Pd atoms by NaAsc, which then nucleate at a fast rate to generate single-crystal seeds. In the next step, the involvement of Br^--capping and room-temperature conditions promotes the formation of Pd concave nanocubes

Figure 3.2A shows a transmission electron microscopy (TEM) image of the typical products of a standard one-pot synthesis. The Pd nanocubes formed through this method are concaved on the side faces, with protruding corners that interrupt the normal {100} facets. The concave nanocubes possess an average length (between two adjacent corners) of 18 nm, with some polydispersity observed, and a noticeable variation in terms of symmetry and protrusion length of the elongated corners from each nanocube. This unique structure can be more clearly discerned using atomic-resolution electron microscopy (Figure 3.2, B and C). From the high-angle annular dark field scanning TEM (HAADF-STEM) images, I can clearly see a nanocrystal that possesses almost no smooth {100} facets present on the surface, but a series of low-coordination atomic sites leading up to the corners.

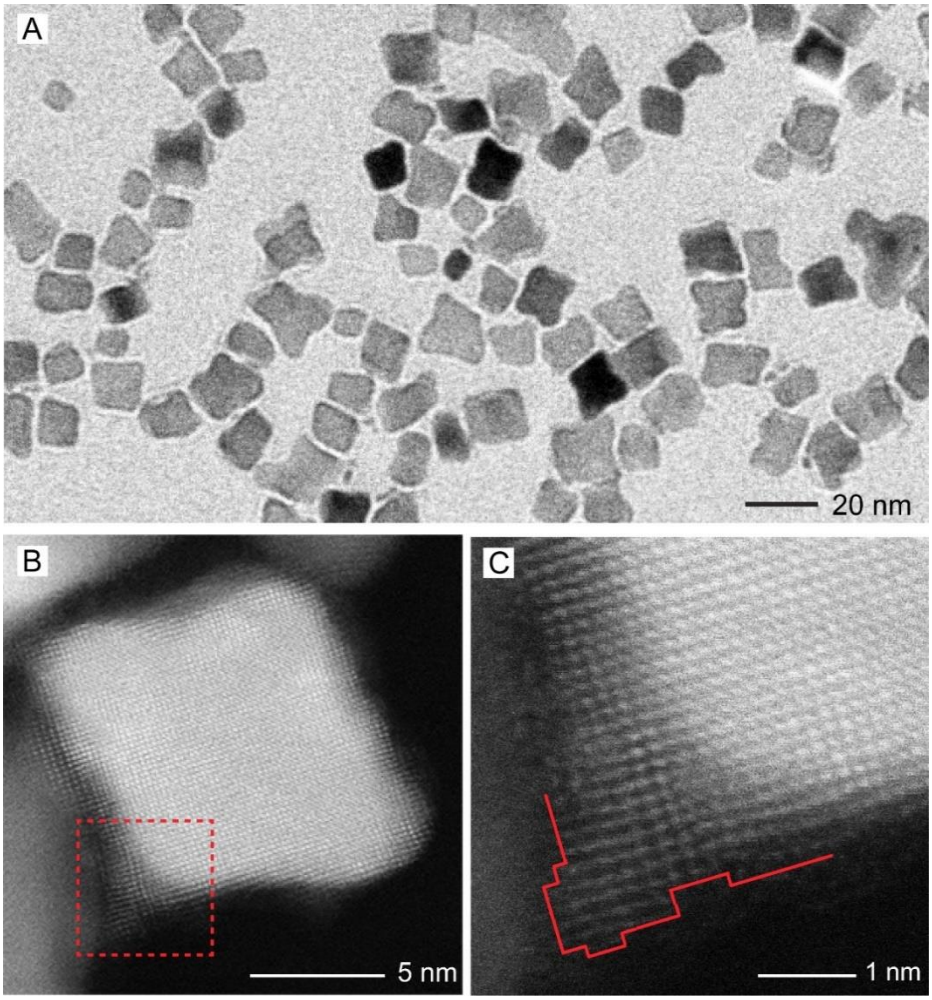

Figure 3.2. (A) TEM image of the Pd concave nanocubes prepared using the standard synthesis, with an average length of approximately 18 nm. (B) HAADF-STEM image of a Pd concave nanocube. (C) Atomic-resolution HAADF-STEM image of the region highlighted by the red box in (B), demonstrating the low-coordination atoms at the corner site (traced by the red outline).

It was of critical importance to establish the precursor species directly involved in the reduction, as prior studies have shown that the activation energy barrier to the reduction (and thus the reduction and nanocrystal growth pathways) are highly dependent on what species are present in the reaction solution. It is well-established in literature that $PdBr_4^{2-}$ has a much higher stability factor than chloro- and aqua-substituted Pd(II) complexes [28-30], which I have found to have a direct impact on the reduction kinetics of the room-temperature synthesis. The reaction solution has KBr at a relatively high concentration of

5.84 mM, which favors the formation of a fully brominated Pd(II) complex rather than any hydrated or partially hydrated species. By monitoring the distinct peaks of the Pd(II) species with UV-vis absorption spectroscopy, $PdBr_4^{2-}$ was confirmed as the major species present in the reaction solution (see Figure 3.3).

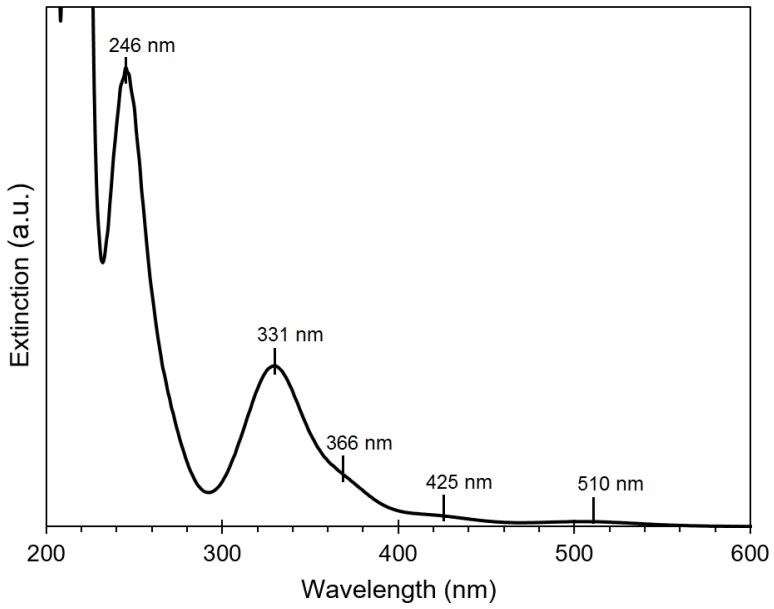

Figure 3.3. UV-vis spectrum of the aqueous Pd(II) precursor solution used for a standard synthesis. The solution was prepared with molar concentrations of 0.0019 mM and 5.84 mM for K_2PdBr_4 and KBr, respectively, the same as what was in a standard synthesis. The spectrum was acquired with a quartz cuvette. The absorption peaks at 246, 331, 366, 425, and 510 nm can all be assigned to $PdBr_4^{2-}$.

With the exact precursor information at hand, the choice of an appropriate reducing agent was critical to designing a successful synthesis. For the conventional synthesis conducted at an elevated temperature, relatively weak reducing agents such as ascorbic acid or formaldehyde are typically used. However, under the room-temperature conditions used for the current synthesis, ascorbic acid cannot overcome the activation energy barrier to reduce $PdBr_4^{2-}$. While $[PdCl_{4-x}(H_2O)_x]^{2-x}$ can be reduced within minutes even at room temperature, the high stability of $PdBr_4^{2-}$ renders the weak reducing agents ineffective at room temperature. Conversely, the use of very strong reducing agents such as $NaBH_4$ leads

to no control for the nucleation and growth processes. In a previous report, this limitation for ascorbic acid was overcome by employing a strong UV-vis light source to excite the Pd(II) species and thus lower the activation energy barrier to reduction [31]. However, this can lead to further complications associated with the penetration depth of UV light and the possible photothermal heating. Here, to initiate a controlled reduction at room temperature, I chose instead to use sodium ascorbate (NaAsc), which has stronger reducing power than ascorbic acid, but is still substantially weaker than conventional "strong" reducing agents such as $NaBH_4$ or hydrazine. Whereas AA showed no active reduction (monitored by the color change in solution from red-brown $PdBr_4^{2-}$ to black Pd^0_n) even over the course of 24 h at room temperature, the use of NaAsc effectively converted >99% of the Pd(II) available in the solution over the course of 3 h only, as confirmed by UV-vis, generating Pd concave nanocubes (see Figure 3.2).

As stated before, most prior reports of Pd concave cubes or octopods have relied on two-pot, seed-mediated growth, first synthesizing Pd cubes and then changing the reaction conditions to favor the growth along the corners. To reveal the one-pot nucleation and growth pathway, I withdrew aliquots from a standard reaction over various time points and monitored the nucleation and subsequent growth of nanocrystals into concave cubes using TEM analysis, shown in Figure 3.4. After 30 min into the reaction, I observed small, single-crystal seeds with an average size of 2-4 nm (Figure 3.4, A and B). At 60 min into the reaction, I could observe the beginning of some facet-directed growth for the seeds (Figure 3.4C). At this stage of the reaction, the nanocrystals approached 6-10 nm in size, and adopted partial cubic morphology, with smooth {100} facets visible on some of the particles, though a large degree of asymmetry and corner rounding was still apparent. As growth of the nanocrystals was continued further (Figure 3.4, D and E), rather than evolving into smooth or truncated cubes, the asymmetry became increasingly more pronounced, and the nanocrystals ultimately adopted the final concave cubic structure (Figure 3.4F).

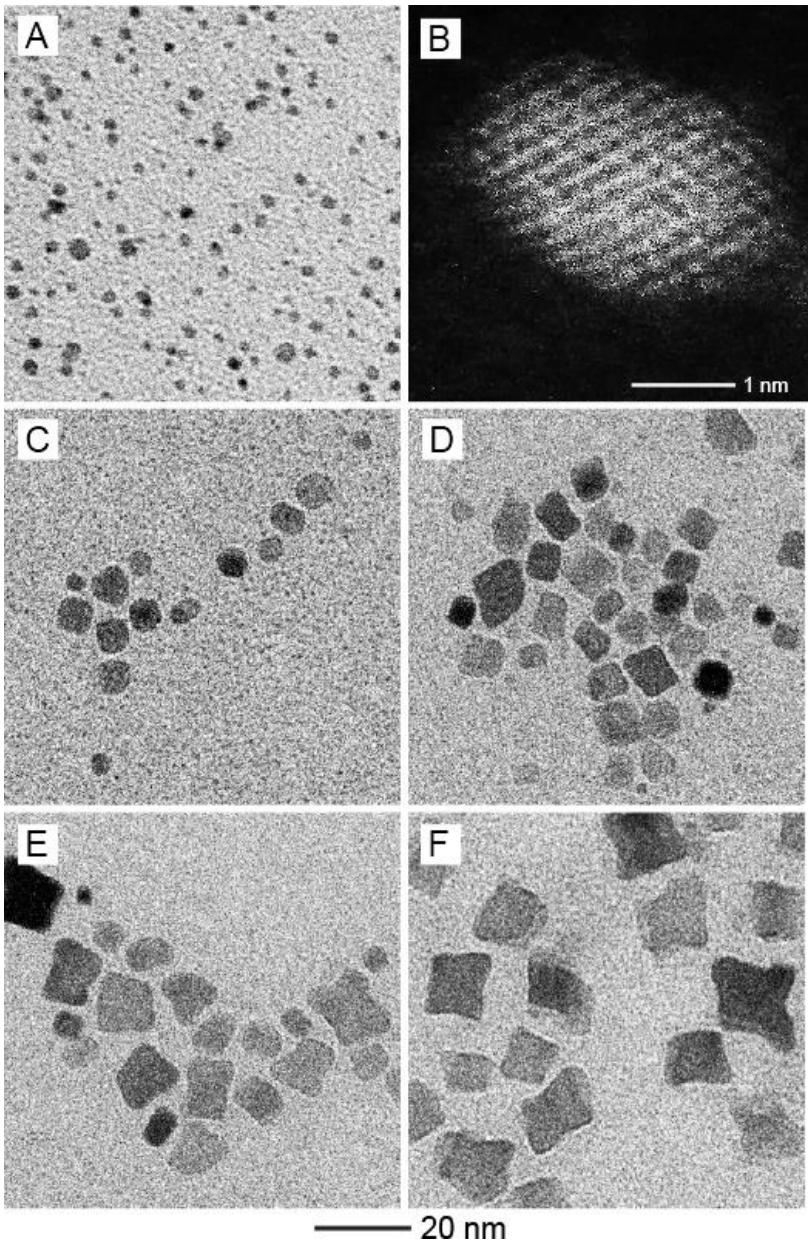

Figure 3.4. TEM images taken from the samples obtained at different time points of a standard synthesis: (A) 30, (C) 60, (D) 90, (E) 120, and (F) 180 min. At the early stage (30 min), single-crystal seeds of 2-4 nm in size were formed, as confirmed by the atomic-resolution HAADF-STEM image in (B), which then grow in size as a function of time. The scale bar at the bottom applies for (A) and (C-F).

As illustrated in Fig. 3.1, both the nucleation and growth are critically dependent on the room-temperature conditions, which will strongly affect the growth process and

reduction kinetics. As demonstrated through the monitoring of a typical reaction solution at varying time points, the metal salt must first undergo reduction and homogeneous nucleation. It is important to note the choice of an appropriate reductant paired to the $PdBr_4^{2-}$ is critical for promoting solution reduction and the initial formation of single-crystal seeds, as a weaker reducing agent would lead to no appreciable nucleation or the potential formation of twinned seeds due to a slow reduction rate. The selection of NaAsc promoted the reduction and nucleation of small, single-crystal seeds within the first 30 min of the reaction. From these initial seeds, an overgrowth process then proceeded over the remaining 150 min of the reaction. The single-crystal seeds gradually grew into larger, pseudo-cubic particles. However, as the remaining metal precursor was exhausted and the nanocrystals grew larger, the seeds ultimately formed asymmetric, concave cubes, with pronounced growth on the corners.

Again, I believe this growth pattern can be largely attributed to the room-temperature environment. Firstly, the generation of concave structures requires conditions wherein the addition of new atoms to the surface of the nanocrystals occurs at a faster rate than adatom diffusion. Using cubes as an example, the deposition of atoms can only occur at the corners and along the ⟨111⟩ directions, as the Br^- ions chemisorb to and block the {100} facets [32]. At elevated temperatures, the adatom surface diffusion rate (which is highly dependent on temperature) is high enough to allow the newly deposited atoms at the corners to diffuse across to the {100} faces, leading to conformal overgrowth and the generation of regular cubes. At room temperature, however, the surface diffusion rate is severely depressed, resulting in extremely sluggish diffusion of adatoms. Instead, new atoms are added to the corners at a rate faster than the existing adatoms can diffuse away, resulting in the formation of concave cubes. Additionally, the room-temperature conditions impact the asymmetric growth observed across the corners on the same nanocrystal. In a recent study by the Xia group on the seed-mediated growth of Pd cubes, it was found that room-temperature conditions favor an asymmetric growth mode too [33]. The limited

supply of atoms led to an inability to activate all eight corners equally for overgrowth, causing the formation of symmetry-broken structures, with only some corners active for continued atom deposition and subsequent growth. I believe the same principle can be applied here to my concave nanocubes, except that in my case, the nanocrystal seeds are formed *in situ* in the same reaction solution, rather than being added for a two-pot synthesis. The room-temperature condition therefore directs not only the growth into concave nanocubes, but also the observed asymmetry in the final Pd structures, which would not otherwise be obtainable at elevated temperatures.

To better understand and validate the kinetics of nucleation *versus* growth in my system, I conducted a series of measurements to monitor the conversion of $PdBr_4^{2-}$ precursor over the course of time. To measure the reduction kinetics of this synthesis, I used UV-vis spectroscopy. The fully bromo-substituted Pd(II) complex can be easily measured through UV-vis spectroscopy, with a major peak at 331 nm that decreases in intensity as it is reduced to Pd metal. During the course of a typical reaction, I sampled aliquots from the reaction solution and then quenched the reaction using cold, concentrated KBr solution, followed by acetone wash to precipitate out any nanocrystals from the solution. The results of the kinetic study can be found in Figure 3.5. A recent report from Xia and coworkers investigated the kinetics that dominate solution reduction *versus* autocatalytic, surface reduction, focusing on the seeded-growth of Pd nanocubes [34]. Through this study, it was feasible to fit the reduction curve of Pd(II) species to competing k_1 and k_2 values of solution reduction *versus* surface reduction (*e.g.*, autocatalytic reduction on the seeds), respectively. This was possible due to the extremely sluggish kinetics of reduction at room temperature for $PdCl_4^{2-}$ and $PdBr_4^{2-}$ by ascorbic acid, the reductant used for these experiments. However, in the case of my Pd concave cubes, I employ the much stronger reducing agent based on NaAsc, which leads to inherently different reduction kinetics.

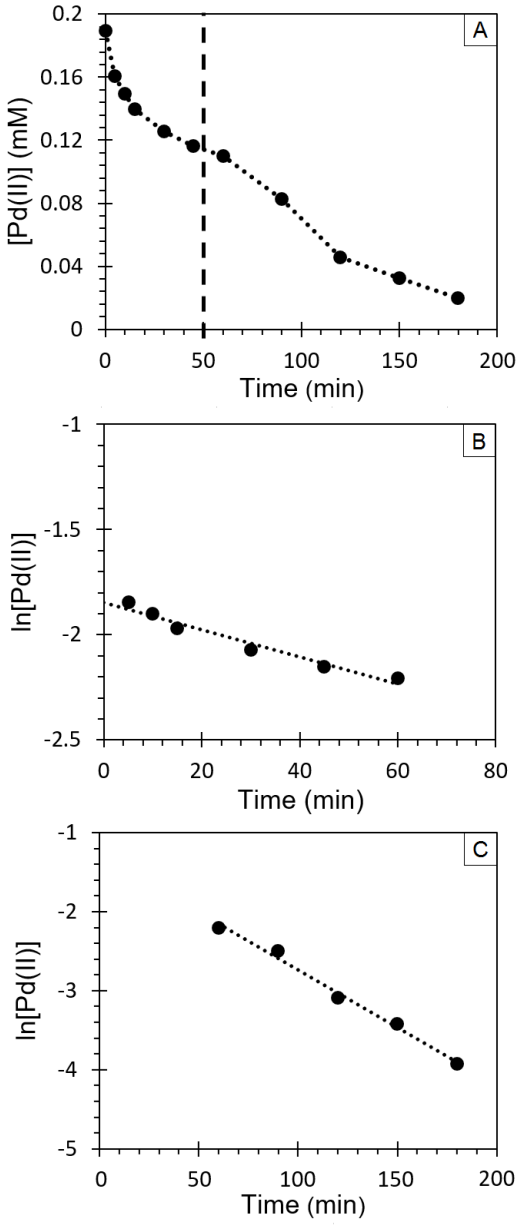

Figure 3.5. (A) Plot of the concentration of Pd(II) remaining in the reaction solution over time for a standard synthesis, derived from UV-vis measurements of the $PdBr_4^{2-}$ peak at 331 nm. The dotted line delineates two different trends. (B) First-order kinetic plot of ln[Pd(II)] over time, showing a linear function for the first apparent trend from 0 to 60 min of the reaction ($R^2 = 0.9613$). (C) First-order kinetic plot of ln[Pd(II)] over time, showing a linear function for second apparent trend from 60 to 180 min of the reaction ($R^2 = 0.9903$).

In the plot of Pd(II) concentration as a function of time shown in Figure 3.5A, I can clearly see two distinctive trends. The first trend extends from the start of the reaction until approximately 60 min, showcasing an initially sharp drop in Pd(II) precursor concentration,

followed by a gradual plateau. I then observe a second trend emerging from 60 min and throughout the remaining duration of the synthesis, again showing a sharper initial drop in Pd(II) concentration, followed by a gradual plateau as the precursor is fully depleted from the solution. These two trends across a single synthesis strongly indicate that two different modes of Pd(II) reduction are occurring, with one mode dominating the first hour of the synthesis before the second mode then directs the final two hours of the synthesis. Notably, both curves can be fitted to a linear first-order or pseudo first-order kinetic fit (*i.e.*, natural logarithm *versus* time, with $R^2 < 0.95$), as shown in Figure 3.5, B and C. The linear fit of both functions indicates that these two pseudo-first order systems are each dominated by a single *k* value, rather than a mixture of reduction pathways at the same time. In the case of any reaction where a salt precursor is being reduced into metal atoms, the reaction solution will always experience a drop in precursor concentration over time. The change in precursor concentration relative to reaction time (coupled with an increase in seed concentration) can therefore lead to switch in reduction pathway, as different reduction paths are more favorable dependent on changes in concentration and thus reduction rates.

Based on prior studies concerning seed-mediated growth, I believe that this two-phase kinetic system can be simplified into two main physical processes for reduction: *i*) solution reduction (Eq. 1), which produces Pd seeds; and *ii*) autocatalytic, surface reduction and growth on the surface of the seeds (Eq. 2), which dominates the growth of the initially formed Pd seeds into Pd concave cubes, as described by the following equations:

$$Pd^{2+} + 2e^- \overset{k_1}{\rightarrow} Pd^0 \qquad (1)$$

$$Pd^{2+} + Pd_n^0 + 2e^- \overset{k_2}{\rightarrow} Pd_{n+1}^0 \qquad (2)$$

For the initial reduction curve, because there are no pre-existing seeds in the solution, I can assume a solution-dominated reduction pathway, wherein the rate formula for solution reduction can therefore be simplified to $rate = k_1[Pd^{2+}]$, as the autocatalytic growth can be ignored. In this case, the reaction follows a classical nucleation process, possible even when using the $PdBr_4^{2-}$ precursor at room temperature due to the presence of NaAsc with a strong reducing power. Here, the concentrations of both Pd(II) and NaAsc are high enough to generate a burst nucleation event, overcoming the energy barrier to $PdBr_4^{2-}$ reduction and freely forming Pd(0) atoms that then nucleate into small seeds. By fitting this linear curve, I am able to obtain a value of $k_1 = 6.5 \times 10^{-3}$ min^{-1} mM^{-1}, and the associated initial reduction rate fits into the regime required for the nucleation of single-crystal seeds [33]. However, as the concentration of both reductant and precursor drops, and as the concentration of seeds dramatically increases, the apparent solution reduction rate drops dramatically (from an initial rate of 1.1×10^{-3} min^{-1} to 7.2×10^{-4} min^{-1} at 60 min into the synthesis). The reaction then switches to a more favorable, autocatalytic reduction mode. In this second pathway, the surface of the seeds simultaneously acts as both a deposition and reduction site, facilitating continued growth-based reduction through a lower energy barrier pathway. Here, the linear function suggests that essentially no solution reduction occurs, and the continued growth of the seeds into concave cubes can be largely attributed to surface reduction. The rate formula for surface reduction can be therefore simplified to $rate = k_2[Pd^{2+}][Pd^0_n]$, as the first-order fit allows the solution reduction to be excluded. From this fit, I obtained $k_2 = 1.45 \times 10^{-2}$ min^{-1} mM^{-1}. As expected, the surface reduction rate constant value k_2 is greater than the k_1 value obtained during solution reduction, as the activation energy barrier to solution reduction and nucleation should be substantially higher to overcome than that of surface reduction and autocatalytic growth.

Finally, to experimentally test my proposed mechanism, I conducted a control experiment in the setting of seed-mediated growth, in which I added Pd seeds to a standard protocol. First, I performed a typical synthesis, except that the synthesis was quenched at

45 min, and the nanocrystals produced at this point were collected *via* centrifugation. I then added these small seeds into a completely new standard synthesis while performing the same series of UV-vis measurements to track the reduction of Pd(II) over time. Given the expectation that autocatalytic growth should dominated the reduction when the seeds are present, it was expected to see a single trend for the concentration of Pd(II) over time. The inset in Figure 3.6 shows that this synthesis also led to the production of Pd concave nanocubes. Indeed, after calculating the natural logarithm of the concentration of Pd(II) against the duration of the synthesis, I obtained a highly linear plot (R^2 = 0.9955). This shows a very clear first-order reaction through the entire 3-h period, correlating with the second, seed-mediated growth kinetic regime observed in the standard synthesis with no seeds added.

Through these kinetic findings, I can therefore propose a two-step reduction mechanism for the nucleation and growth of Pd concave nanocubes. During the initial stages of the synthesis, the reduction of $PdBr_4^{2-}$ follows a classical nucleation scheme. The $PdBr_4^{2-}$ in solution is reduced at room temperature by the sufficiently strong reducing agent, NaAsc, with a high enough reduction rate and concentration as to generate single-crystal seeds. As the concentrations of $PdBr_4^{2-}$ and the reducing agent begin to decrease and the amount of seeds increase, the reduction pathway instead favors autocatalytic, surface reduction. As the excess Br^- ions added into the reaction effectively cap and block the {100} facets of the nanocrystal seeds, new Pd atoms are only deposited on the corner sites of the seeds. The inherently sluggish adatom surface diffusion rates at room temperature have a two-fold effect on the outcome of a synthesis: *i*) limited site activation results in asymmetric growth between the corners, and *ii*) pile-up of new atoms on the corners prevents conformal adatom surface diffusion from occurring. As a result, concave Pd cubes with a high degree of asymmetry are formed through a one-pot synthesis.

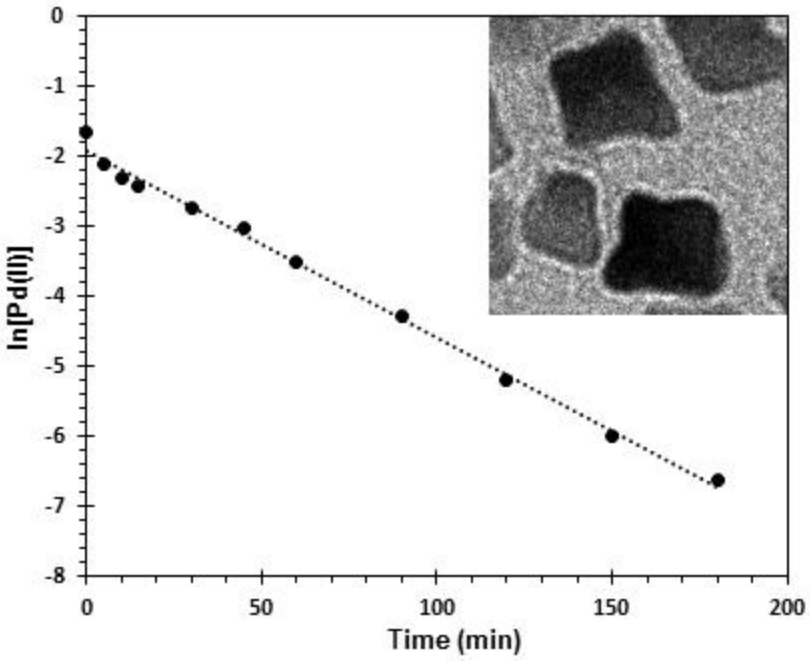

Figure 3.6. First-order kinetic plot of ln[Pd(II)] over time, taken from a standard synthesis except adding Pd seeds, showing a linear function for the entire 180 min duration of the reaction ($R^2 = 0.9955$). The inset TEM image in the upper right corner shows the concave cubes that were still formed through this seed-growth reaction.

3.3 Conclusion

In summary, I have designed a one-pot, room-temperature method for the facile synthesis of Pd concave nanocubes. The success to my synthesis was through the manipulation of reduction kinetics and thus the reduction pathway. Sodium ascorbate was sufficiently strong to quickly reduce $PdBr_4^{2-}$ into atoms in the solution for the generation of single-crystal seeds even at room temperature. Upon the formation of seeds, the reduction kinetics was greatly slowed down due to the depletion of both precursor and reducing agent in the reaction solution. This led to the switch from solution reduction to surface reduction, in which precursor reduction and atom deposition occurred simultaneously on the surface of the seeds instead of in the solution. The reduction kinetics was monitored and verified through a spectroscopic analysis, demonstrating the complete dominance of solution reduction (k_1) during the initial stage of a synthesis, and then the

dominance of surface reduction (k_2) during the later stage of a synthesis. Because of the selective capping of bromide ions towards the {100} facets, the autocatalytic growth could only occur at the corner and/or edge sites. When coupled with the inherently low surface diffusion rate of adatoms and the asymmetric activation pattern, both associated with room temperature conditions, the Pd seeds ultimately evolved into concave nanocubes, with an asymmetric pile up of atoms occurring along the corners and/or edges available for atom deposition. By rationally choosing the experimental conditions, I can program the reduction kinetics of a synthesis for the formation of nanocrystals with high-index facets and geometrically complex structures in one pot. This approach should be applicable across multiple metal nanocrystal materials and compositions.

3.4 Experimental Section

Chemicals and Materials. Sodium ascorbate (NaAsc, 99%), poly(vinyl pyrrolidone) (PVP, M_w≈55,000), potassium bromide (KBr, 98%), and potassium tetrabromopalladate(II) (K_2PdBr_4, 98%) were all purchased from Sigma-Aldrich. All chemicals were used as received. The water used for all the experiments was deionized (DI) to achieve a resistivity of 18.2 MΩ cm at room temperature.

Synthesis of Pd Concave Cubes. For a standard synthesis of the Pd concave nanocubes, 96 mg of K_2PdBr_4 was first dissolved in 3 mL of DI water. In a separate 6-dram vial, 105 mg of PVP, 67 mg of NaAsc, and 695 mg of KBr were dissolved in 8 mL of DI water. The K_2PdBr_4 salt solution was then quickly added to the vial in one shot, and the reaction mixture was capped and magnetically stirred at room temperature for 3 h. Afterwards, the Pd nanocrystals were collected *via* centrifugation at 55,000 rpm for 30 min. The product was washed and centrifuged twice with DI water, then re-dispersed in 11 mL of DI water for further use.

Instrumentation. All TEM images were obtained using a Hitachi HT 7700 microscope with an operating voltage of 120 kV. The HAADF-STEM images were collected using a

Hitachi HD 2700 operated at 200 kV. Samples were prepared for EM imaging by drop casting the colloidal suspension onto a carbon-coated copper grid, and allowing the sample to dry under ambient conditions. For HAADF-STEM imaging, the sample was cleaned of remnant surfactant by treating in a Hitachi Zone cleaner for 30 min each side at a pressure setting of 30. All UV-vis absorption spectra were recorded with a Lambda 750 spectrometer (PerkinElmer).

3.6 References

[1] Xiong, Y.; Xia, Y. *Adv. Mater.* **2007,** *19*, 3385-3391.

[2] Watt, J.; Young, N.; Haigh, S.; Kirkland, A.; Tilley, R. D. *Adv. Mater.* **2009,** *21*, 2288-2293.

[3] Niu, W.; Zhang, L.; Xu, G. *ACS Nano* **2010,** *4*, 1987-1996.

[4] Niu, Z.; Peng, Q.; Gong, M.; Rong, H.; Li, Y. *Angew. Chem. Int. Ed.* **2011,** *50*, 6315-6319.

[5] Wang, Y.; Xie, S.; Liu, J.; Park, J.; Huang, C. Z.; Xia, Y. *Nano Lett.* **2013,** *13*, 2276-2281.

[6] Huang, H.; Wang, Y.; Ruditskiy, A.; Peng, H.-C.; Zhao, X.; Zhang, L.; Liu, J.; Ye, Z.; Xia, Y. *ACS Nano* **2014,** *8*, 7041-7050.

[7] Lim, B.; Jiang, M.; Tao, J.; Camargo, P. H. C.; Zhu, Y.; Xia, Y. *Adv. Funct. Mater.* **2009,** *19*, 189-200.

[8] Cheong, S.; Watt, J. D.; Tilley, R. D. *Nanoscale* **2010,** *2*, 2045-2053.

[9] Tian, N.; Zhou, Z.-Y.; Yu, N.-F.; Wang, L.-Y.; Sun, S.-G. *J. Am. Chem. Soc.* **2010,** *132*, 7580-7581.

[10] Wang, F.; Li, C.; Sun, L.-D.; Wu, H.; Ming, T.; Wang, J.; Yu, J. C.; Yan, C.-H. *J. Am. Chem. Soc.* **2011,** *133*, 1106-1111.

[11] Deng, Y.-J.; Tian, N.; Zhou, Z.-Y.; Huang, R.; Liu, Z.-L.; Xiao, J.; Sun, S.-G. *Chem. Sci.* **2012,** *3*, 1157-1161.

[12] Wang, F.; Li, C.; Sun, L.-D.; Xu, C.-H.; Wang, J.; Yu, J. C.; Yan, C.-H. *Angew. Chem. Int. Ed.* **2012,** *51*, 4872-4876.

[13] Collins, G.; Schmidt, M.; O'Dwyer, C.; McGlacken, G.; Holmes, J. D. *ACS Catal.* **2014,** *4*, 3105-3111.

[14] Quan, Z.; Wang, Y.; Fang, J. *Acc. Chem. Res.* **2013,** *46*, 191-202.

[15] Xia, Y.; Gilroy, K. D.; Peng, H.-C.; Xia, X. *Angew. Chem. Int. Ed.* **2017,** *56*, 60-95.

[16] Habas, S. E.; Lee, H.; Radmilovic, V.; Somorjai, G. A.; Yang, P. *Nat. Mater.* **2007,** *6*, 692-697.

[17] Berhault, G.; Bausach, M.; Bisson, L.; Becerra, L.; Thomazeau, C.; Uzio, D. *J. Phys. Chem. C* **2007,** *111*, 5915-5925.

[18] Xia, Y.; Xia, X.; Peng, H.-C. *J. Am. Chem. Soc.* **2015,** *137*, 7947-7966.

[19] Wang, F.; Li, C.; Sun, L.-D.; Xu, C.-H.; Wang, J.; Yu, J. C.; Yan, C.-H. *Angew. Chem. Int. Ed.* **2012,** *51*, 4872-4876.

[20] Zhang, J.; Feng, C.; Deng, Y.; Liu, L.; Wu, Y.; Shen, B.; Zhong, C.; Hu, W. *Chem. Mater.* **2014,** *26*, 1213-1218.

[21] Ruditskiy, A.; Vara, M.; Huang, H.; Xia, Y. *Chemistry of Materials* **2017,** *29*, 5394-5400.

[22] Jin, M.; Zhang, H.; Xie, Z.; Xia, Y. *Angew. Chem. Int. Ed.* **2011,** *50*, 7850-7854.

[23] Niu, W.; Zhang, W.; Firdoz, S.; Lu, X. *Chem. Mater.* **2014,** *26*, 2180-2186.

[24] Sreedhala, S.; Sudheeshkumar, V.; Vinod, C. P. *Nanoscale* **2014,** *6*, 7496-7502.

[25] Zhang, J.; Zhang, L.; Xie, S.; Kuang, Q.; Han, X.; Xie, Z.; Zheng, L. *Chem. Eur. J.* **2011,** *17*, 9915-9919.

[26] Liu, S.-Y.; Shen, Y.-T.; Chiu, C.-Y.; Rej, S.; Lin, P.-H.; Tsao, Y.-C.; Huang, M. H. *Langmuir* **2015,** *31*, 6538-6545.

[27] Xie, X.; Gao, G.; Pan, Z.; Wang, T.; Meng, X.; Cai, L. *Sci. Rep.* **2015,** *5*, 8515.

[28] Elding, L. I. *Inorg. Chim. Acta.* **1972,** *6*, 647-651.

[29] Elding, L., *Inorg. Chim. Acta*. **1978,** *28*, 255-262.

[30] Elding, L. I.; Olsson, L. F. *J. Phys. Chem.* **1978,** *82*, 69-74.

[31] Vara, M.; Lu, P.; Yang, X.; Lee, C.-T.; Xia, Y. *Chem. Mater.* **2017,** *29* , 4563-4571.

[32] Peng, H.-C.; Li, Z.; Aldahondo, G.; Huang, H.; Xia, Y. *J. Phys. Chem. C* **2016,** *120*, 11754-11761.

[33] Wang, Y.; Peng, H.-C.; Liu, J.; Huang, C. Z.; Xia, Y. *Nano Lett.* **2015,** *15*, 1445-1450.

[34] Yang, T.-H.; Peng, H.-C.; Zhou, S.; Lee, C.-T.; Bao, S.; Lee, Y.-H.; Wu, J.-M.; Xia, Y. *Nano Lett.* **2017,** *17*, 334-340.

CHAPTER 4

EVALUATING THE THERMAL STABILITY OF SINGLE-CRYSTAL PALLADIUM@PLATINUM CORE-SHELL NANOCRYSTALS BY *IN SITU* ELECTRON MICROSCOPY

4.1 Introduction

In recent years, bimetallic core-shell nanocrystals have received considerable attention as a class of heterogeneous catalysts and electrocatalysts for a variety of applications. The bimetallic composition can often lead to improvement in catalytic activity, selectivity, and durability, while the use of two different metals can reduce the loading of the more expensive metal involved [1-6]. Additionally, the core-shell structure offers an easy access to diverse architectures by changing the metals involved or the conditions of synthesis. In generating such structures, the core metal is often synthesized as nanocrystals with the desired shape, and then conformally coated with a controlled amount of the second metal through a process such as seed-mediated growth [7-9]. Using this simple approach, a plethora of bimetallic core-shell nanocrystals has been successfully synthesized. Among them, Pd@Pt core-shell nanocrystals are of particular interest. Platinum has long been the material of choice for an ever-increasing number of catalytic reactions vital to the chemical and petroleum industries, as well as energy conversion and protection of the environment [10-14]. However, due to the extremely low abundance of Pt in nature and its rising demand from various applications, there is an urgent need to improve the activity and durability of Pt-based catalysts while simultaneously decreasing the loading of Pt in a catalyst. As a result, Pd@Pt core-shell nanocrystals have emerged as an effective route toward reducing the Pt loading (and thus materials cost) while still maintaining or even improving catalytic performance. This is due to the ability to both easily tune the shape (or the type of exposed crystal facet) of the Pd nanocrystal in the core and to controllably alter the number of Pt

atomic layers during conformal deposition. To this end, Pd nanoscale cubes, octahedra, decahedra, icosahedra, plates, and rods, among others, have all been successfully applied to the synthesis of Pd@Pt core-shell nanocrystals with enhanced catalytic properties [9, 15-19].

Despite the tremendous progress in controlling the synthesis of Pd@Pt nanocrystals, there is essentially no report on how these bimetallic nanostructures behave and ultimately degrade at the elevated temperatures typically associated with industrial catalytic processes. It is becoming increasingly critical to develop a comprehensive understanding of not only how these nanocatalysts initially perform, but also how they respond to thermal stress over time. Fundamental insights on this important question will ultimately enable us to rationally design nanocrystals with both enhanced activity and improved durability for various catalytic applications. It is therefore necessary to investigate the stability of bimetallic nanocatalysts in real time.

To this end, electron microscopy with *in situ* heating capability is emerging as a promising analytical technique. In particular, high-resolution scanning transmission electron microscopy (STEM) allows us to resolve the structure of metal nanocrystals down to the atomic level. When integrated with *in situ* heating, this imaging technique can be used to monitor the structural and compositional changes of bimetallic nanocrystals on a per-particle basis in real time as they are heated to the desired temperatures. For example, a recent study demonstrated that the thermal stability of Pd@Rh core-frame nanocubes could be increased relative to Pd nanocubes by retarding the diffusion of atoms from the corner and edge sites to the side faces at elevated temperatures [20]. The atomic-scale evolution of elemental diffusion and surface arrangements of Pt_3Co nanoparticles upon thermal annealing were investigated *in operando* using STEM [21]. In addition, *in situ* heating has also been used to directly observe and analyze the annealing of PtFe nanocrystals into ordered intermetallic structures, the alloying of Co@Ni core-shell particles, and the thermal stability of the corrugated Pt shell on a Pd icosahedron [19, 22,

23]. In all these cases, the integration of *in situ* heating with electron microscopy provided an invaluable tool for observing and understanding atomic level changes that occurred in real time during the course of heating. Nevertheless, most of these studies were focused on nanoparticles with a single shape or morphology, with limited or no comparison to other similar types of nanoparticles. It is critical to systematically investigate the shape-dependent structure-property relationship between core-shell nanocrystals and their thermal stability.

In this Chapter, I have chosen to focus on Pd@Pt_{4L} core-shell nanocrystals (where the Pt shells were controlled at a thickness of about four atomic layers) with cubic and octahedral shapes. They are enclosed largely by {100} and {111} facets, respectively, and represent two of the basic shape-controlled nanocrystals with a single-crystal structure. This feature makes them ideal candidates for *in situ* heating studies as even minor changes to their initial structure and morphology can be readily resolved, monitored, and analyzed. As the nanocrystals are heated, I am able to directly resolve changes to the shape or facet caused by surface diffusion, as well as the alloying between the core and the shell as a result of atomic inter-diffusion. Additionally, first-principles simulations provide important insights capable of rationalizing the experimentally observed behaviors. My *ex situ* heating experiments also demonstrate that the Pd@Pt_{4L} core-shell nanocrystals are stable at temperatures up to 400 °C.

4.2 Results and Discussion

Synthesis of Pd@Pt_{4L} Core-Shell Nanocrystals. The Pd@Pt_{4L} cubes and octahedra were prepared by following the methods reported in the literature. I first synthesized Pd nanocrystal templates with a cubic or octahedral shape, and then conformally coated their surfaces with Pt shells in an atomic layer-by-layer fashion [9, 16, 24]. The Pt deposition was conducted by slowly adding a Pt salt precursor with a syringe pump at an elevated temperature. This allowed adequate time for the Pt adatoms to diffuse across the surface of

each Pd template, eliminating island growth and resulting in the formation of Pt conformal shells with controllable thickness. I could directly tune the number of Pt overlayers in the shell by varying the amount of Pt salt precursor relative to the number of Pd templates involved.

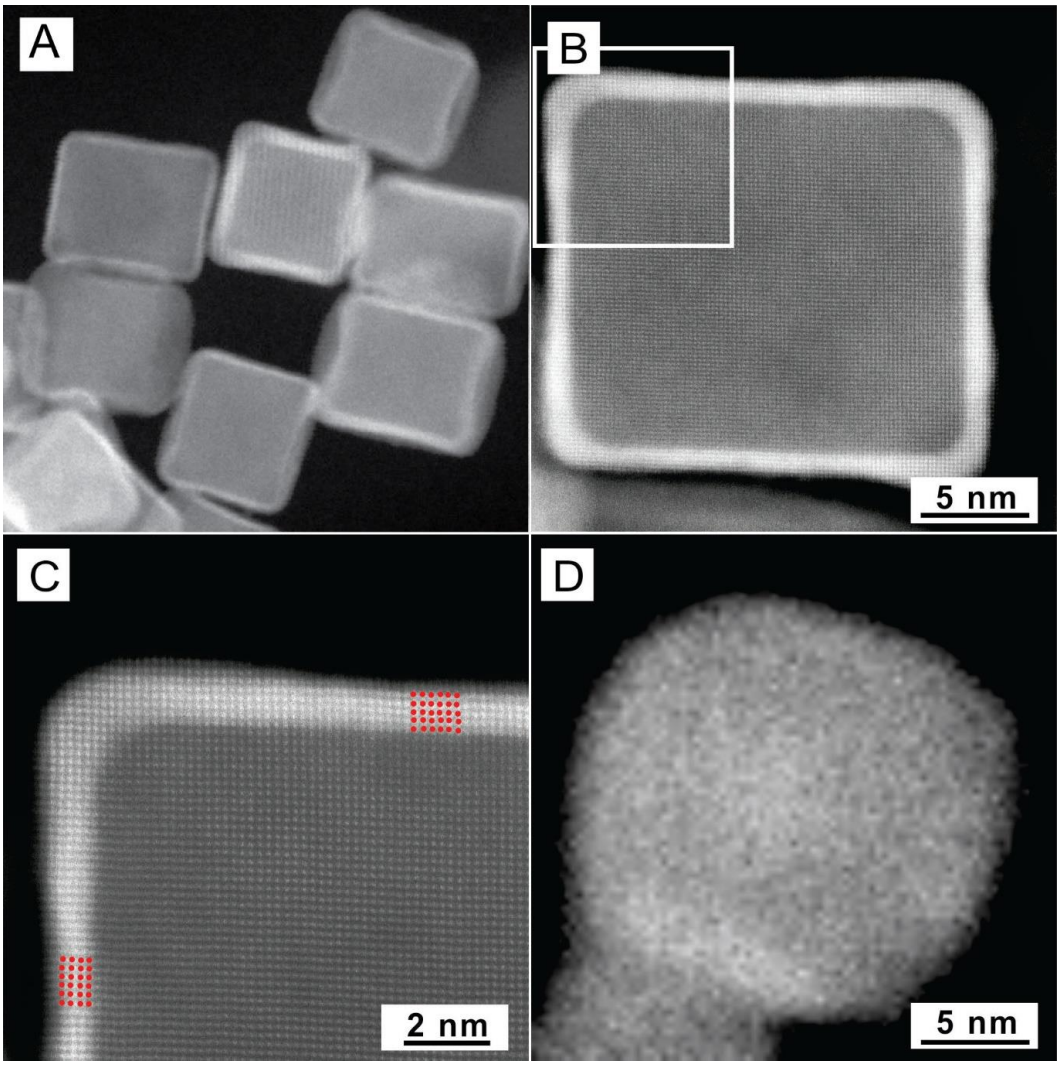

Figure 4.1. (A) HAADF-STEM image of a number of typical Pd@Pt_{4L} cubes at room temperature, all showing a clear core-shell structure. (B) HAADF-STEM image of an individual Pd@Pt_{4L} cube at room temperature, illustrating that the Pd cubic seed was coated by a Pt shell (brighter contrast from higher Pt atomic number). (C) High-resolution HAADF-STEM image taken from the region boxed in (B), showing a thickness of 4-5 atomic layers for the Pt shell. (D) *In situ* HAADF-STEM image of a Pd@Pt_{4L} cube upon quick heating to 800 °C. At 800 °C, the nanocrystal lost its obvious core-shell structure and deformed into a round particle lacking clear facet definition. (Reprinted with permission from [37]. Copyright 2016 American Chemical Society.)

Electron Microscopy Analysis of the Thermal Stability of the Core-shell Nanocrystals. For *in situ* heating studies, I used an Aduro (Protochips) holder and the corresponding silicon nitride Aduro thermal E-chips capable of uniformly heating samples up to 1200 °C at rates up to 1000 °C ms^{-1}. In order to directly monitor not only the changes in shape of the nanocrystals, but also any mixing between the Pd core and the Pt shell, the experiments were operated in the high-angle annular dark field scanning transmission electron microscopy (HAADF-STEM) mode. Under this imaging mode, elements with larger atomic numbers scatter electrons more effectively, resulting in a z-contrast image. This allows us to readily resolve the elemental distinction between the dimmer Pd core and the brighter Pt shell. Figure 4.1A shows a set of typical HAADF-STEM images of Pd@Pt_{4L} cubes at room temperature, clearly revealing the core-shell structure. Figure 4.1B shows the image taken from a single Pd@Pt_{4L} cube. The atomic-resolution image in Figure 4.1C further confirms the core-shell structure, with a shell containing 4-5 conformal overlayers of Pt deposited on the Pd cubic core. While bulk Pt has a melting point of 1772 °C, I was not certain about the melting point of Pt shells of only 4-5 atomic layers in thickness due to the melting-point depression phenomenon. In an initial test, I simply heated the sample to 800 °C. Upon elevation to this temperature, the nanocrystal deformed, almost instantaneously, to lose its cubic profile as its corners and edges were rounded (Figure 4.1D). The core-shell structure also disappeared as Pd and Pt inter-diffusion occurred. This observation suggests that the Pd@Pt_{4L} nanoscale cubes could not be held unaltered up to 800 °C.

In order to obtain a deeper understanding of the shape deformation and alloying processes and the respective threshold temperatures, I examined another sample of the Pd@Pt_{4L} cubes over a much more gradual and extended number of heating ramps (see Figure 4.2 and Figure 4.3). Figure 4.3 shows a set of HAADF-STEM images recorded from a single Pd@Pt_{4L} cube over a series of heating steps that were held for different intervals

of time at increasing temperatures. Figure 4.3A shows the cube after heating at 400 °C for 20 min. At this stage of heating, the particle did not show any significant change when compared with the sample at room temperature, except for some very mild rounding observed at the corner and edge sites.

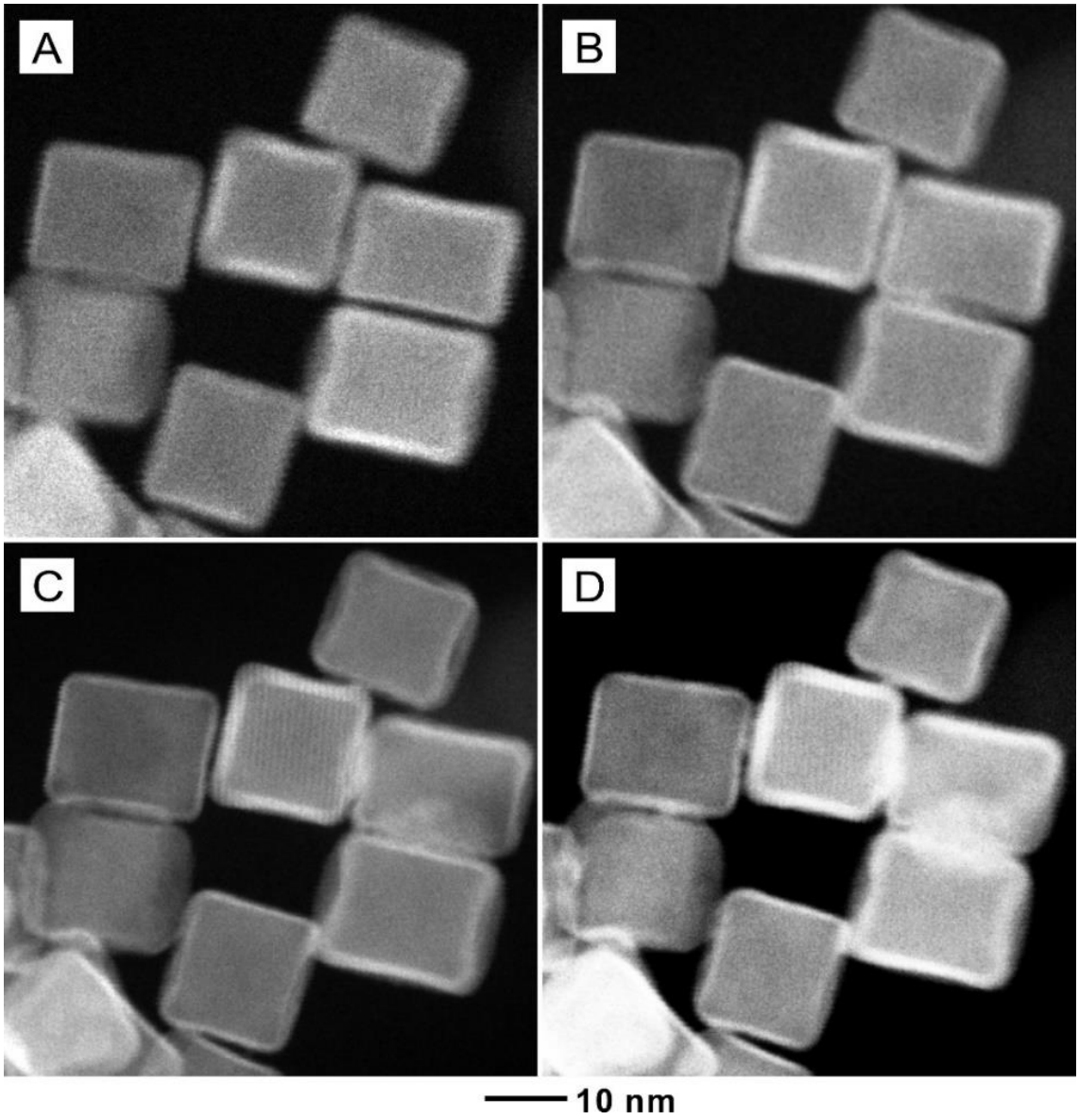

Figure 4.2. *In situ* HAADF-STEM images of Pd@Pt_{4L} nanocubes recorded from the same region after heating at different temperatures for varying periods of time: (A) 400 °C for 1 min, (B) 400 °C for 20 min, followed by (C) 500 °C for 20 min, and then (D) 600 °C for 40 min. (Reprinted with permission from [37]. Copyright 2016 American Chemical Society.)

The core-shell separation of Pd and Pt remained well defined under the HAADF-STEM mode, and the {100} side faces of the cube still appeared very smooth. Upon heating to 500 °C for 20 min (Figure 4.3B), no substantial changes were observed relative to the earlier sample heated to 400 °C. However, after heating at 500 °C for a total of 40 min (Figure 4.3C), I began to observe major changes to the particle. The core-shell structure remained clearly delineated, yet structural changes had started to occur. Interestingly, while the interior Pd core still appeared as a relatively sharp cube, the exterior Pt shell had clearly thinned along the directions of corners and edges. The Pt atoms diffused across the side faces, yielding a rounded profile. Upon extending the heating at 500 °C for another 20 min (to a total of 60 min, Figure 4.3D), no further significant changes were observed. After heating at 600 °C for 40 min (Figure 4.3E), the surface of the nanocrystal had completely deviated from a well-defined cube, with Pt atoms continuing the trend of diffusion onto the original {100} side faces from the corners and edges. At this high temperature, the core-shell structure began to blur, indicating alloying (Figure 4.3F). Indeed, further *ex situ* testing indicates the loss of core-shell structure alongside shape at this temperature (Figure 4.4). As shown in Figure 4.3D, the expressed facets were lost at 800 °C, accompanied by complete alloying between the Pd core and the Pt shell.

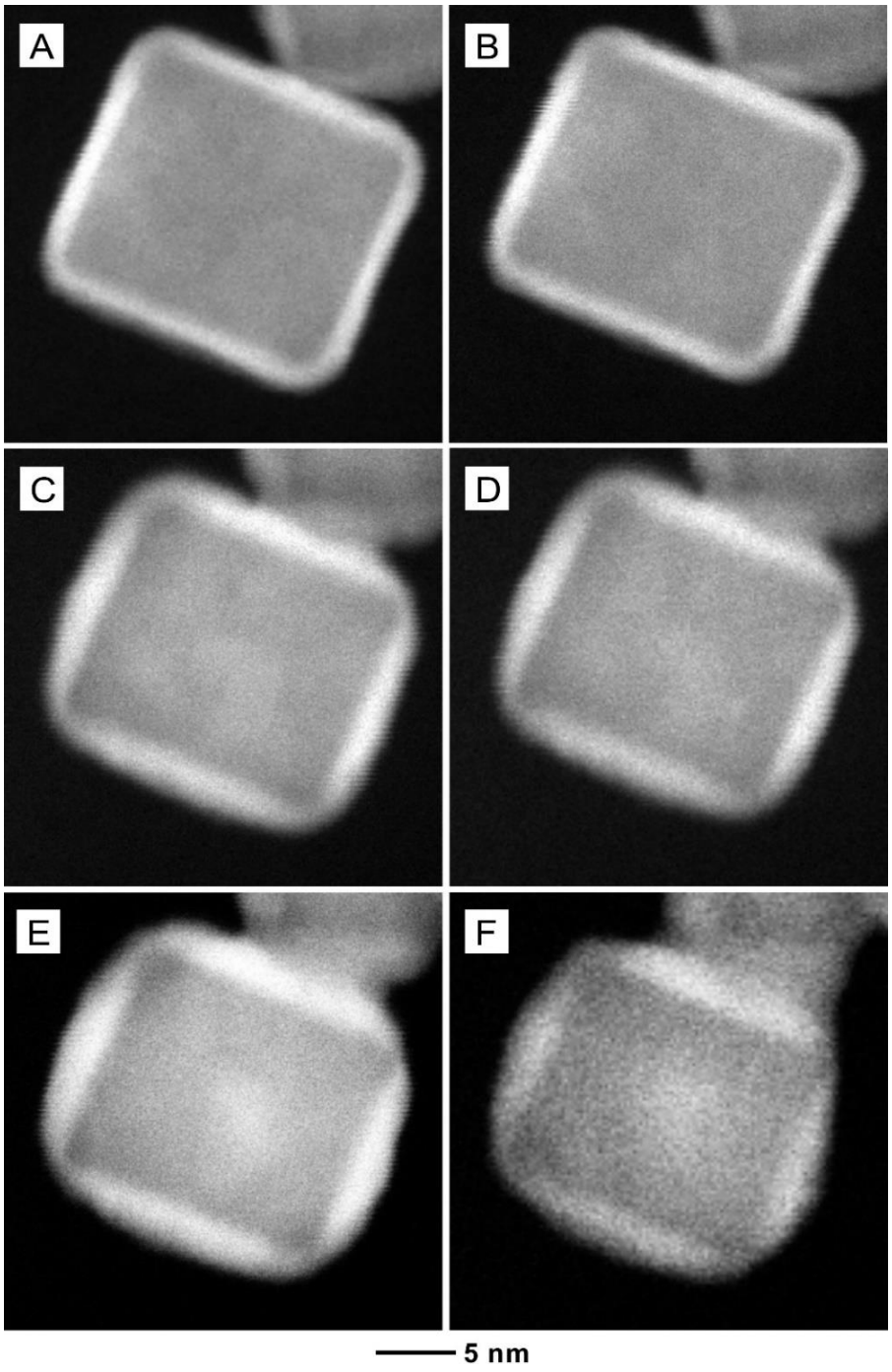

Figure 4.3. *In situ* HAADF-STEM images recorded from the same Pd@Pt_{4L} cube under different heating conditions: (A) 400 °C for 20 min; followed by heating at 500 °C for (B) 20 min, (C) 40 min, and (D) 60 min; and then heating at (E) 600 °C for 40 min and (F) 700 °C for 10 min. The core-shell structure was well retained even after heating at temperatures as high as 700 °C. For the Pd@Pt_{4L} cube, the cubic shape was lost after heating at 500 °C while the core-shell structure was lost after heating at 800 °C. (Reprinted with permission from [37]. Copyright 2016 American Chemical Society.)

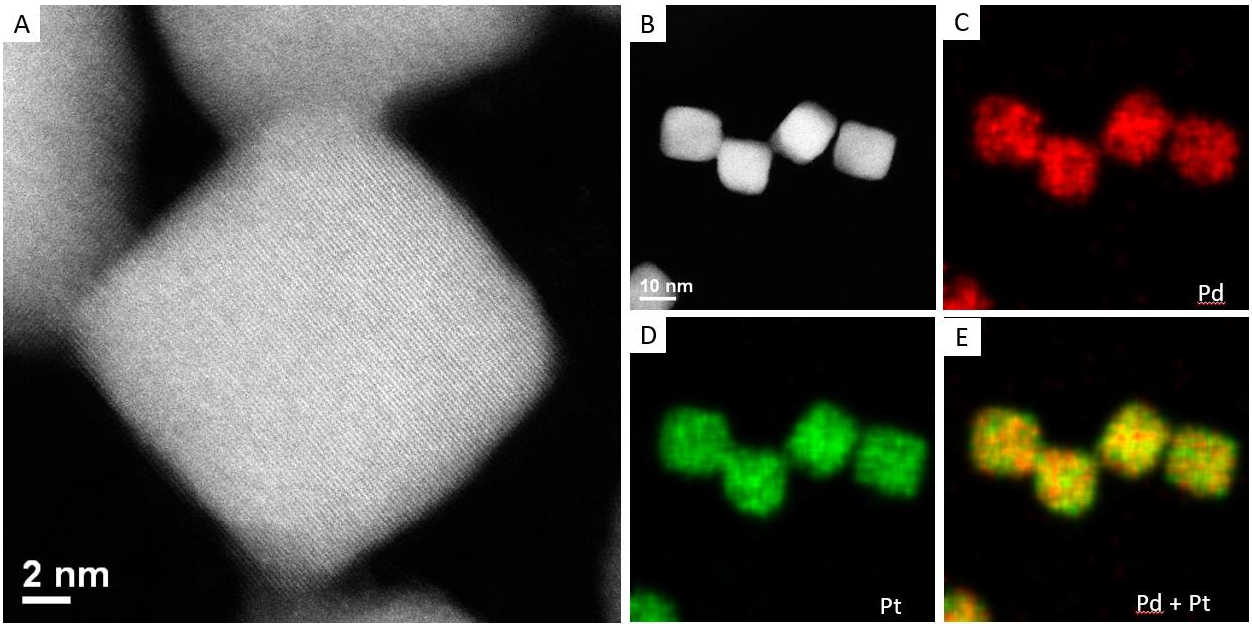

Figure 4.4. (A) *Ex situ* HAADF-STEM image of a Pd@Pt_{4L} nanocube after heating at 700 °C for 10 min. (B) HAADF-STEM images of several cubes. (C-D) EDX mapping data of the cubes imaged in (B), showing the loss of sharp core-shell structure. (Reprinted with permission from [37]. Copyright 2016 American Chemical Society.)

To investigate and compare the shape-dependence of the thermal stability, I then conducted a similar experiment of heating steps using the Pd@Pt_{4L} core-shell octahedra (Figure 4.5). Similar to the cube, after heating at 400 °C for 20 min (Figure 4.5A), no changes were observed in the core-shell nanocrystal. The octahedron maintained smooth {111} facet definition and a clear separation of the bright, conformal Pt coating from the dimmer Pd core. Whereas the core-shell cube began to show noticeable shape deformation upon heating to 500 °C, the octahedron exhibited no obvious change in the shape and facets even after heating at 500 °C for 60 min (Figure 4.5B). The octahedral shape remained stable up to this temperature, but some blurring of the Pd core and Pt shell boundary began to appear. Such atomic inter-diffusion became much clearer in Figure 4.5C, after the sample had been heated at 600 °C for 20 min. At this stage, all z-contrast distinction between the core and shell was lost, indicating full alloying between the core and the shell.

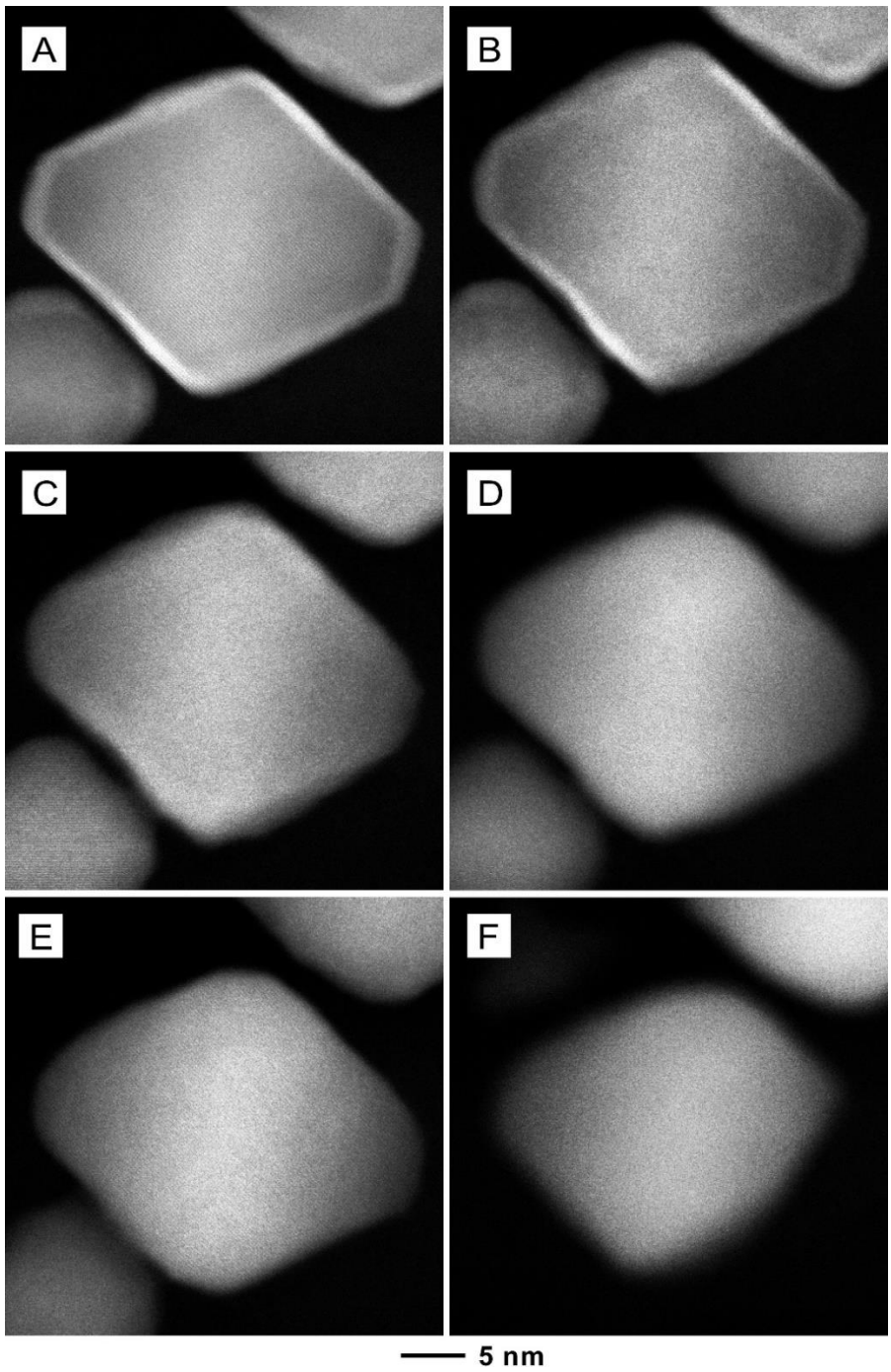

Figure 4.5. *In situ* HAADF-STEM images recorded from the same Pd@Pt_{4L} octahedron under different heating conditions: (A) 400 °C for 20 min; followed by heating (B) at 500 °C for 60 min, (C) 600 °C for 20 min, (D) 700 °C for 10 min, (E) 800 °C for 10 min, and then (F) 900 °C for 5 min. For the Pd@Pt_{4L} octahedron, the core-shell structure was lost after heating at 600 °C, while the octahedral shape was lost after heating at 900 °C. (Reprinted with permission from [37]. Copyright 2016 American Chemical Society.)

Interestingly, opposite to the trend observed in the cubes where the cubic shape was lost first and alloying occurred afterwards at higher temperatures, the octahedral shape remained fully intact even after alloying had occurred. The stability of facets in octahedra persisted upon heating at 700 °C (Figure 4.5D), and even after initial heating up to 800 °C (Figure 4.5E). Indeed, *ex situ* heating tests confirmed that at 700 °C, where the cube had lost shape, the octahedron still showed well-preserved {111} facets even though alloying had occurred (Figure 4.6). It was only when the temperature was elevated to 900 °C (Figure 4.5F) that the octahedral shape finally started to deform, nearly 400 °C higher than the point observed for the shape deformation of the Pd@Pt_{4L} cube. Notably, the stability trends for the Pd@Pt_{4L} octahedron *versus* the cube appear to be inverted. The cube lost shape stability around 500 °C, yet did not lose the core-shell structure until 800 °C. In contrast, the octahedron showed dramatically increased shape stability. However, it showed much reduced core-shell stability, alloying at closer to 600 °C, nearly 200 °C lower than that for the core-shell cube.

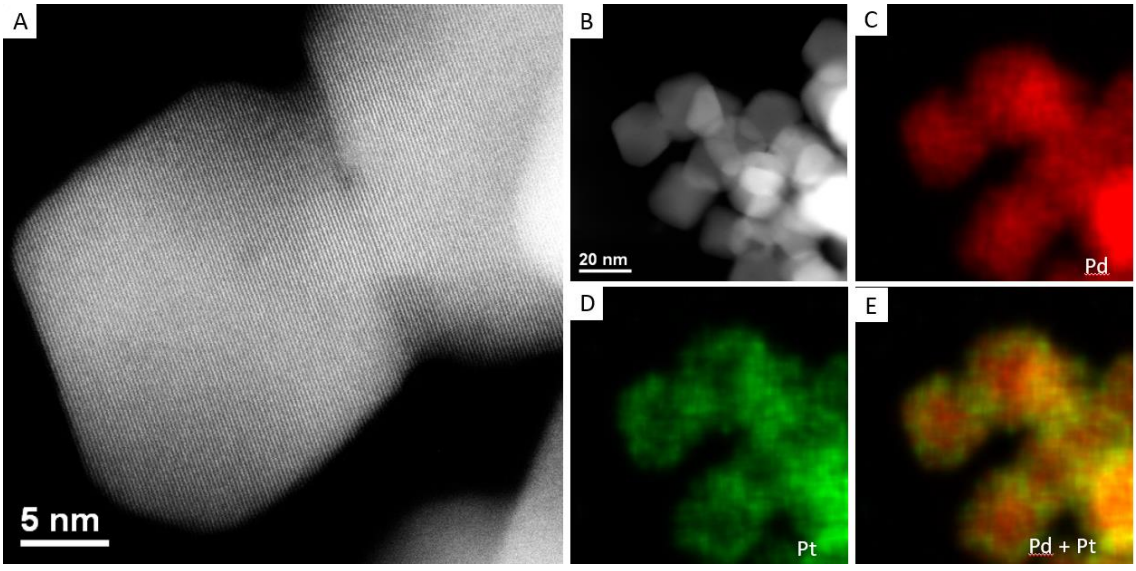

Figure 4.6. (A) *Ex situ* HAADF-STEM image of a Pd@Pt_{4L} octahedron after heating at 700 °C for 10 min. (B) HAADF-STEM images of several octahedra. (C-D) EDX mapping data of the octahedra imaged in (B), showing the loss of sharp core-shell structure. (Reprinted with permission from [37]. Copyright 2016 American Chemical Society.)

I also performed additional *ex situ* stability tests to confirm the increase in stability for the Pd@Pt core-sell nanocrystals relative to the pristine Pd cores. Whereas Pd cubes were found to readily deform and lose their {100} facets upon heating at 400 °C for less than 10 min [20], the Pd@Pt_{4L} cubes were thermally stable at the same temperature (Figure 4.7A). Even after holding at 400 °C for 1 h, the particle clearly maintained both the {100} facets (Figure 4.7B) and core-shell structure (Figure 4.7C-E). In parallel, *ex situ* heating and elemental mapping was conducted for the sample of core-shell octahedra after heating at 400 °C for 1 h (Figure 4.8A). As with the core-shell cubes, the core-shell octahedra also showed excellent stability at this temperature, preserving both the {111} facets (Figure 4.8B) and the core-shell structure (Figure 4.8C-E). Taken together, these results clearly demonstrate that the Pd@Pt_{4L} core-shell nanocrystals are promising for catalytic applications at temperatures up to 400 °C.

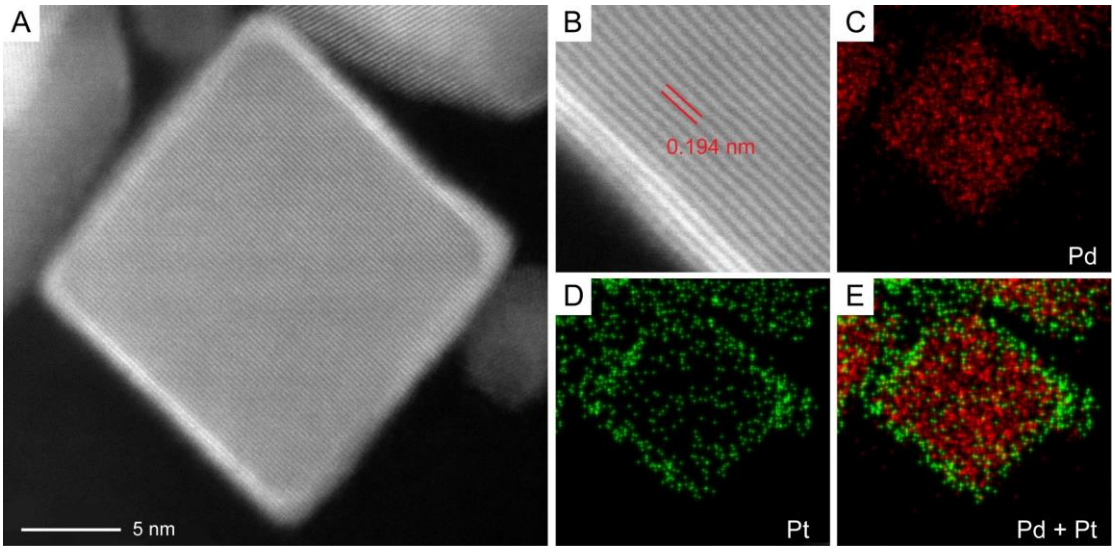

Figure 4.7. (A) *Ex situ* HAADF-STEM image of a Pd@Pt_{4L} nanocube after heating at 400 °C for 1 h. (B) Lattice image of a portion of the cube imaged in (A) with a corresponding *d*-spacing that matches the {100} facet of Pd. (C-E) EDX mapping data of the cube imaged in (A), showing preservation of the core-shell structure. (Reprinted with permission from [37]. Copyright 2016 American Chemical Society.)

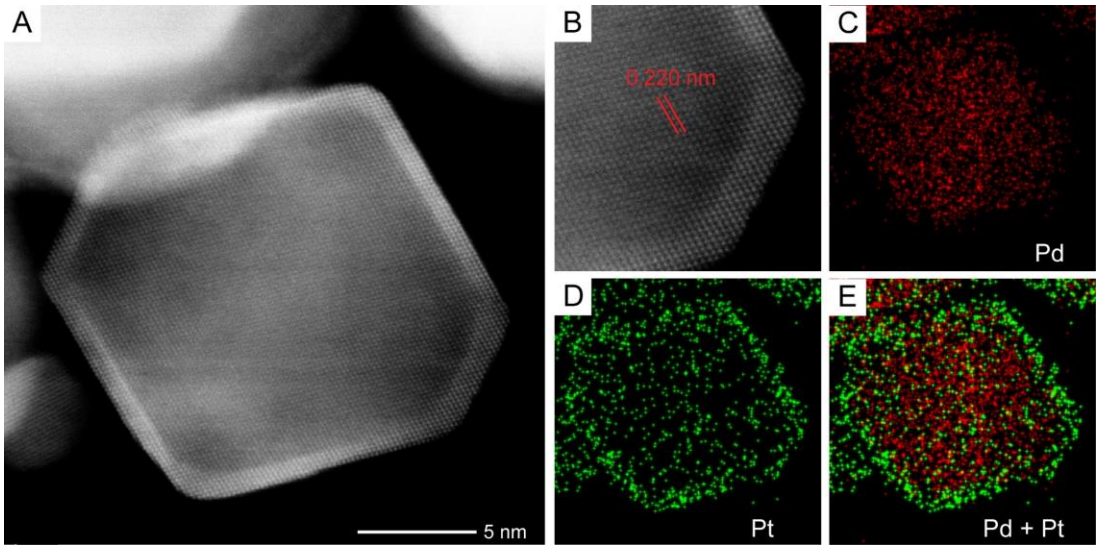

Figure 4.8. (A) *Ex situ* HAADF-STEM image of a Pd@Pt_{4L} octahedron after heating at 400 °C for 1 h. (B) Atomic resolution image of a portion of the particle imaged in (A) with a corresponding *d*-spacing that matches the {111} facet of Pd. (C-D) EDX mapping data of the particle imaged in (A), showing preservation of the core-shell structure. (Reprinted with permission from [37]. Copyright 2016 American Chemical Society.)

Computational Study of the Thermal Degradation Mechanisms. To elucidate the driving force behind these experimentally observed behaviors, my collaborators performed periodic self-consistent density functional theory (DFT) calculations (GGA-PW91, details in Methods section). They focused first on the observed change in nanocrystal shape with increasing temperature to determine why the cubic shape deformed at substantially lower temperatures than did the octahedral one. At first, this phenomenon was hypothesized to arise from the relative mobility of surface metal adatoms on the two nanocrystals. They constructed surface models in which four atomic layers of platinum were deposited atop a Pd(100) or Pd(111) slab, hereafter denoted as Pt_{4L}*/Pd(100) or Pt_{4L}*/Pd(111), to represent the cubic and octahedral systems respectively. They then investigated the diffusion of a Pt adatom across each of these surfaces. They considered mechanisms in which the adatom can "hop" across the surface, as well as surface exchange mechanisms similar to those suggested by Feibelman for Al adatoms on Al(100), through which an adatom replaces a surface atom by ejecting it to a neighboring surface site [35]. They found that the octahedral

(111) surface model strongly preferred diffusion *via* the hopping mechanism (with a barrier of 0.28 eV, compared to 1.41 eV for exchange), while the cubic (100) surface model preferred the exchange mechanism (0.48 eV, compared to 1.06 eV for hopping). Comparing the respective lower energy barrier on each surface, 0.28 eV for (111) *vs.* 0.48 eV for (100), these data suggest that Pt adatom movement on the (111) octahedral surfaces should be more facile than on the cubic (100) surfaces. However, the octahedral nanocrystals experimentally demonstrated a reduced tendency to restructure than did the cubic ones. These calculated diffusion barriers are also sufficiently low that adatom movement on either surface should readily occur at room temperature, let alone the higher temperatures at which shape deformation was observed. Together, these data suggest that a different phenomenon is likely responsible for restructuring the shape of the nanocrystals.

My collaborators therefore investigated the kinetics of cubic and octahedral nanocrystal edge reconstruction to seek an alternative explanation for the observed behaviors. Specifically, they calculated the activation energy barrier for removing one atom from the edge row in catalyst models representing perfect cubes and octahedra (Figure 4.9). They found that the energy barrier for moving an atom from the cubic edge to an adjacent face (which selectively exposes a (100) facet) is 0.60 eV; this event proceeded through one edge atom pushing an adjacent terrace atom onto the (100) surface, leaving behind a vacancy in the row of edge atoms. This process is exothermic ($\Delta E = -0.15$ eV). In contrast, the analogous event for moving an edge atom to an adjacent (111) surface of an octahedral model has a barrier of 1.99 eV, again proceeding through pushing an adjacent terrace atom onto the (111) surface. Moreover, this process is highly endothermic ($\Delta E = 1.64$ eV). The differences between the cubic and octahedral edge atom energetics stem from the geometric details of the two edge configurations: the edge atoms in the cubic geometry are bound to five neighboring atoms, while those in the octahedral edge are bound to seven. This corresponds to the sharper dihedral angle (90°) of the cubic geometry compared to that of the octahedral geometry (109.5°). The increased number of bonds to neighboring

atoms at the octahedral model increases the stability of the edge atoms. This subsequently reduces the edge atom mobility and makes reconstruction more difficult in octahedra than in the cubes. They also calculated the surface energies of the Pt_{4L}*/Pd(100) and Pt_{4L}*/Pd(111) surfaces, and found that the (111) surface is more stable by 0.03 eV $Å^{-2}$. This difference in energetics additionally drives the reconstruction of the cubes at lower temperatures than the octahedra.

Geometry	Initial State	Transition State	Final State
Cubic	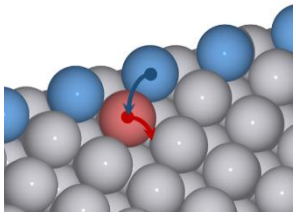 0.00	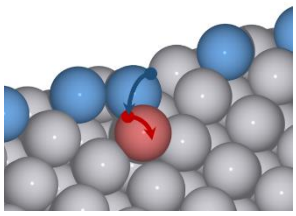 0.60	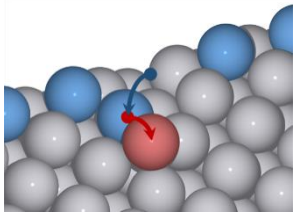 -0.15
Octahedral	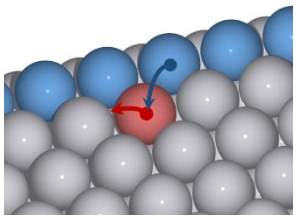 0.00	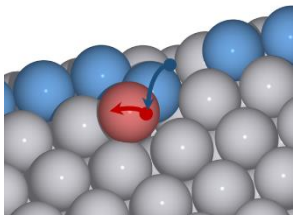 1.99	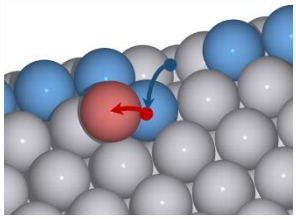 1.64

Figure 4.9. Mechanistic details of the process of moving an atom from the edge to the side face for nanocrystals with two different geometrical shapes. The associated energy required to remove an edge atom on a given nanocrystal is dependent on the particle facet, or interchangeably, shape (DFT-calculated energetics in eV are provided). Removal of an edge atom from the cubic geometry is exothermic and has a lower activation energy barrier than removal of an edge atom from the octahedral geometry, explaining the higher shape stability of octahedral Pd@Pt_{4L} nanocrystals *versus* cubic Pd@Pt_{4L} nanocrystals. All atoms shown are Pt; edge atoms are highlighted in blue and the displaced terrace atoms are shown in red. (Reprinted with permission from [37]. Copyright 2016 American Chemical Society.)

To understand the observed behavior in the core-shell degradation process, my collaborators performed a detailed study of adatom exchange at the Pt-Pd interface in the Pt_{4L}*/Pd(100) and Pt_{4L}*/Pd(111) models. Without the presence of vacancies, adatom

exchange deep within the slab model (*via* rotational mechanisms of atoms at the bimetallic interface) requires very high activation energy barriers (greater than 5 eV). Therefore, I concluded that Pt-Pd intermixing must be a vacancy-mediated process, similar to what was concluded previously for Pd diffusion through a Pt shell [24]. A detailed set of calculations of atomic movement through vacancies in the slab was conducted, finding greatly reduced barriers for atomic diffusion (<1.4 eV), as shown in Figure 4.10. These reduced energy barriers in the presence of vacancies are sufficient to allow for inter-diffusion of the core-shell morphology at the temperatures at which core-shell degradation was observed experimentally. The calculations suggest that these required subsurface vacancies are seeded in the nanoparticles during the deposition of Pt atoms atop the Pd surface. Since the Pt overlayers are formed layer-by-layer, there will be periods during nanoparticle formation in which the topmost layer is nearly, but not completely, full (*e.g.*, 0.9ML coverage). Under these conditions, the calculations show that an atom from the topmost complete layer can readily diffuse upward to fill a surface vacancy (Figure 7). Importantly, while the activation energy barriers for creating such a subsurface vacancy are relatively similar between the (100) and (111) surfaces (0.46 eV and 0.50 eV, respectively), the upward movement is far more exothermic on the (111) surface ($\Delta E = -0.88$ eV) than on the (100) surface (–0.14 eV). As a result, reverse (downward) diffusion of Pt atoms back into the subsurface vacancy is unlikely to occur on the (111) surface and therefore a much higher concentration of subsurface vacancies can be seeded in the {111} facets of the octahedra than in the {100} facets of the cubes. The vacancy-mediated activation energies for metal atom migration deeper in the subsurface layers are relatively similar between the (100) and (111) surfaces (as shown in Figure 4.10). Therefore, I propose that it is the higher concentration of subsurface vacancies favored in the (111) surface that allows the degradation of the Pd@Pt core-shell structure to occur at lower temperatures in the octahedra than in the cubes. Finally, in addition to the increased configurational entropy yielded by Pd and Pt mixing, I note that in both geometries intermixing between Pt and Pd

at the interface is an energetically favorable process. This provides a thermodynamic driving force for the observed complete alloying of the Pt shell with the Pd core.

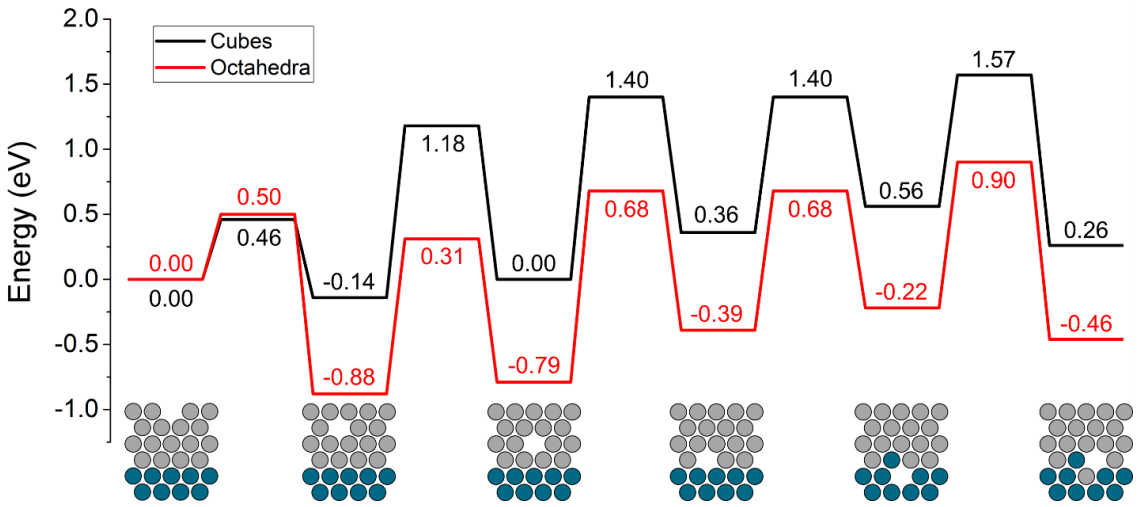

Figure 4.10. Energetics of subsurface vacancy in Pd@Pt_{4L} nanocrystal surface models. Provided are images and calculated energetics of vacancies in each of the first five layers of the Pt_{4L}*/Pd slab models (shown as minima in the energy surface) and the energies of the associated transition states (shown as maxima between images). All energies are provided in eV; the reference state has a vacancy in the topmost Pt layer in both geometries, and the respective energies are set to 0.00 eV for a more direct comparison of vacancy propagation energetics. The right-most image corresponds to an intermixed state formed from downward diffusion of Pt into a vacancy created by upward movement of Pd. The energetics of subsurface vacancy formation and subsequent metal atom diffusion are substantially more favorable on the octahedral models, leading to higher rates of atomic inter-diffusion and loss of the core-shell structure at lower temperatures. For brevity, only the (100) surface model is shown in the images. Pt atoms are shown in gray, and Pd atoms in blue. (Reprinted with permission from [37]. Copyright 2016 American Chemical Society.)

4.3 Conclusion

In conclusion, I have studied the thermal stability of Pd@Pt_{4L} core-shell nanoscale cubes and octahedra by HAADF-STEM integrated with *in situ* heating. My results indicate greater stability in shape for the octahedral nanocrystals, but better stability in core-shell structure for their cubic counterparts. The Pd@Pt_{4L} cubes enclosed by {100} facets began to deform and lose their smooth facets after extended heating at 500 °C. In comparison, the

Pd@Pt_{4L} octahedra enclosed by the relatively lower surface energy {111} facets did not lose their octahedral shape and smooth facets until 900 °C, 400 °C above what was observed for the cubic system. The DFT calculations of my collaborators rationalized this observed trend in shape stability by pointing to a much higher activation energy barrier associated with the removal of a surface atom from the edge to a side face for the octahedra. As a result, the octahedra maintained their shape and {111} facets to higher temperatures than the cubes and their {100} facets. While the {111} facets on octahedra were preserved at elevated temperatures, the core-shell structure of the Pd@Pt_{4L} octahedra was lost to inter-diffusion after heating at 600 °C, 300 °C below the temperature at which the octahedral shape started to deform. In contrast, alloying in the cubic system did not occur appreciably until heating at 800 °C, despite the fact that the cubic shape started to deform at 500 °C. The DFT models suggest a much lower energy associated with the generation of subsurface vacancies in {111} facets as compared to {100} facets. The higher propensity for the presence of subsurface vacancies in the {111} facets, which dominate the octahedral shape, can explain the lower temperature threshold toward atomic inter-diffusion that is experimentally observed. In addition, my *ex situ* heating experiments confirmed that both the facet and structure of the core-shell nanocrystals were stable at temperatures up to 400 °C. Taken together, this work offers fundamental insights for the rational design of core-shell nanocatalysts with improved and predictable thermal stability.

4.4 Experimental Section

Chemicals and Materials. L-ascorbic acid (AA, 99%), poly(vinyl pyrrolidone) (PVP, M_w≈55,000), potassium bromide (KBr, 98%), and sodium hexachloroplatinate(IV) hexahydrate (Na_2PtCl_6•$6H_2O$), 98%) were all purchased from Sigma-Aldrich. Formaldehyde (HCHO) was obtained from Fisher Scientific, ethylene glycol (EG, 99%) was obtained from J.T. Baker, ethanol (200 proof, KOPTEC) was obtained from VWR, and sodium tetrachloropalladate (Na_2PdCl_4, 36% Pd) was obtained from Acros Organics.

All chemicals were used as received. All water used for experiments was deionized (DI) water with a resistivity of 18.2 MΩ cm.

Synthesis of 10-nm and 18-nm Cubes. The Pd cubes used for Pt coating were synthesized following a previous report [26]. The 18-nm Pd cubes were used directly for Pt coating. The 10-nm Pd cubes were used as seeds for Pd overgrowth into Pd octahedra of 19 nm in edge length.

Synthesis of 19-nm Pd Octahedra. The Pd octahedra used for Pt coating were synthesized following a previously reported overgrowth protocol [27]. The 19-nm edge length Pd octahedra were then used directly for Pt coating.

Synthesis of Pd@Pt_{4L} Core-Shell Cubes and Octahedra. The Pd@Pt_{4L} core-shell nanocubes were prepared according to a previous report [24]. Pd@Pt_{4L} core-shell octahedra were prepared using the same protocol as for the for the Pd@Pt_{4L} core-shell cubes, except substituting the Pd cubic seeds with the 19-nm octahedral seeds (0.83 mg/mL) [9].

***In Situ* Scanning Transmission Electron Microscopy (STEM).** Electron microscopy imaging was carried out on a Cs-corrected FEI Titan 80/300 kV TEM/STEM microscope at Oak Ridge National Laboratory (ORNL). All STEM images were acquired using 300 kV and a beam size of ~0.7 Å with a convergence angle of 30 mrad and collection angles of 65-220 mrad using a HAADF detector. The *in situ* heating studies were conducted using a Protochips Aduro heating holder. Nanocrystal samples for the heating tests were prepared by drop casting liquid suspensions onto Aduro thermal devices, and then allowed to fully air dry before further use. All heating steps were conducted at the rate of 1000 °C ms^{-1} to raise the temperature instantaneously.

***Ex Situ* STEM and Elemental Mapping.** For *ex situ* heating at 400 °C for 1 h, samples were placed on TEM grids and heated under vacuum using a Gatan Hot Stage Power Supply, Model 628-0500. The samples were subsequently imaged and mapped using energy-dispersive X-ray spectroscopy (EDX) on a cold-field emission Hitachi HD-

2700 aberration-corrected STEM operated at 200 kV at the Institute for Electronics and Nanotechnology (IEN) on Georgia Tech campus. A Bruker Quantax 400/S -STEM with an XFlash 6T|60 silicon drift detector (SDD) was used for the EDX analysis. For *ex situ* heating tests at 700 °C, samples were heated on a Protochips Aduro heating holder, and then imaged and EDX mapped on a JEOL JEM 2200FS STEM/TEM equipped with a CEOS probe corrector operated at 200 kV at ORNL. A Bruker-AXS SDD was used for the EDX elemental analysis.

Computational Methods. All calculations were performed using periodic self-consistent density functional theory (DFT) as implemented in the VASP code [28,29]. The electron-ion interactions were described by projector augmented wave potentials [30,31], and the exchange-correlation functional was described self-consistently by the generalized gradient approximation (GGA-PW91) [32]. The Kohn-Sham electron wave function was expanded in a basis of plane waves with a kinetic energy cutoff of 400 eV. The surface Brillouin zone was sampled using a 4 x 4 x 1 Monkhorst-Pack *k*-point mesh for all models [33]. All geometry optimizations were performed until the Hellmann-Feynman forces on atoms were less than 0.01 eV $Å^{-1}$. The dipole correction to the electrostatic potential was included [34]. Minimum energy paths and activation energy barriers were calculated using the climbing-image nudged elastic band (CI-NEB) method [35]. Seven intermediate images were interpolated between the initial and final configurations. All surface models were constructed using the optimized lattice constant of Pd, calculated to be 3.96 Å, in good agreement with the experimental value of 3.89 Å [36].

Surface Diffusion Calculations. Using a model similar to that of previous work [9,16], my collaborators modeled the faces of the cubic and octahedral core-shell nanocrystals with (100) and (111) facets, respectively. Both lattices were constructed using a 3 x 3 surface unit cell and ten total layers of metal atoms, with five equivalent layers of vacuum separating successive slabs. The top four layers were composed of Pt atoms, to model the four Pt-overlayers deposited experimentally, and the remaining six layers

comprised Pd atoms. They denote these model systems as Pt_{4L}*/Pd(100) for cubes and Pt_{4L}*/Pd(111) for octahedra. The bottom two layers were fixed, and all other layers were fully relaxed.

Edge Reconstruction Calculations. To model the edges of the cubes and of the octahedra, my collaborators first constructed a (110) slab of eight atomic layers thick. A 3 x 5 surface unit cell was used for the cubic model, and a 5 x 4 surface unit cell was used for the octahedral model; these unit cells were selected to maintain a relatively consistent edge length and slab depth between the two geometries modeled. Atoms from these slabs were then removed from the upper slab layers to render a 90.0° dihedral angle and a 109.5° dihedral angle between the resulting (100) and (111) facets of the cubic and octahedral models, respectively. Accordingly, the surface models accurately represent idealized edge geometries for both the cubes and the octahedra. They note that this construction yields adjacent edge atoms that are nearest neighbors in the octahedral crystal structure, while edge atoms in the cubic geometry are not nearest-neighbors. As a result, edge atoms in the octahedral geometry have seven nearest neighbors while those in the cubic geometry have only five. The bottom two layers of the original (110) slab were left uncleaved by the edge construction and were fixed at their lattice positions; all other atoms were allowed to fully relax. Note that the nanocrystals modeled in this study have four layers of platinum deposited atop the (111) or (100) facets. In this edge model, all atoms considered are within the four-layer depth of the exposed (100) or (111) surfaces. My collaborators therefore only explicitly use Pt atoms in these models, ignoring the negligible ligand effect from the deeper Pd atoms, although the fixed atoms are compressed to the lattice constant of Pd to account for the lattice strain effect.

Surface Energy Calculations. The surface energies of slabs were calculated as the difference between the energy of an 18-layer slab and the corresponding number of Pt and Pd atoms in bulk Pt and bulk Pd, *i.e.*, $E_{surf} = E_{slab} - m * E_{Pt} - n * E_{Pd}$, where m and n are the number of Pt and Pd atoms, respectively, in the slab. The slab was constructed with

a 1x1 surface unit cell, and terminated on both side with 4 Pt layers (10 Pd layers in the center of the slab). The calculated surface energies were normalized to the exposed surface areas of the slab. A 12 x 12 x 1 *k*-point mesh was used for these calculations. The calculated surface energy for the cubic models (constructed as a (100) surface) was 0.104 eV $Å^{-2}$; the surface energy for the octahedral models (using a (111) surface) was 0.079 eV $Å^{-2}$.

Vacancy Formation and Subsurface Atom Diffusion Calculations. My collaborators performed a comprehensive set of calculations to determine the thermodynamics and kinetics associated with vacancy formation and subsurface atom diffusion as a function of depth in the model systems: Pt_{4L}*/Pd(100) for cubes, and Pt_{4L}*/Pd(111) for octahedra (identical model slabs to those used for the surface diffusion calculations described previously). They first considered diffusion mechanisms in perfect slab models (no vacancies) through all combinations of three-body and four-body rotations of Pt and Pd atoms at the Pt/Pd interface, finding that these barriers all exceeded 5 eV. They then considered the energetics of vacancy-mediated mechanisms for subsurface atom diffusion. In particular, they considered two categories of such processes: (1) diffusion of Pt through Pt layers, and (2) intermixing at the Pt/Pd interface. Activation energy barriers for category (1) were calculated for movement of a Pt atom from an adjacent layer into a vacancy. As shown in Figure 5, activation energy barriers for category (2) were calculated for upward movement of a Pd atom into a vacancy in the Pt layer of the Pt/Pd interface, as well as for subsequent movement of Pt into the newly-generated vacancy in the Pd layer. These processes are intended to model the initial stages of mixing, and are admittedly not representative of later-stage mixing in which considerable intermixing of Pt and Pd has already occurred. Still, I believe that these phenomena provide general insight into the relevant differences between intermixing in the cubic and octahedral geometries. Also note that my collaborators performed a non-exhaustive study to calculate the energetics of well-mixed Pt and Pd (relative to perfect core-shell models), and found that the intermixed structure is energetically preferred by at least 0.02 eV per metal atom (in addition to any

entropic preference for a well-mixed Pt-Pd structure). This provides sufficient evidence that the core-shell structures have a thermodynamic preference for continued intermixing after vacancy propagation to the Pt-Pd interface.

4.5 Notes to Chapter 2

Part of this chapter is adapted from the paper "Understanding the Thermal Stability of Palladium-Platinum Core-Shell Nanocrystals by *in situ* Transmission Electron Microscopy and Density Functional Theory" published in *ACS Nano* [37].

4.6 References

[1] Wang, D.; Xin, H. L.; Hovden, R.; Wang, H.; Yu, Y.; Muller, D. A.; DiSalvo, F. J.; Abruña, H. D. *Nat. Mater.* **2013,** *12*, 81-87.

[2] Chen, C.; Kang, Y.; Huo, Z.; Zhu, Z.; Huang, W.; Xin, H. L.; Snyder, J. D.; Li, D.; Herron, J. A.; Mavrikakis, M.; Chi, M.; More, K. L.; Li, Y.; Markovic, N. M.; Somorjai, G. A.; Yang, P.; Stamenkovic, V. R. *Science* **2014,** *343*, 1339-1343.

[3] Oezaslan, M.; Hasché, F.; Strasser, P. *J. Phys. Chem. Lett.* **2013,** *4*, 3273-3291.

[4] Silva, D. O.; Luza, L.; Gual, A.; Baptista, D. L.; Bernardi, F.; Zapata, M. J. M.; Morais, J.; Dupont, J. *Nanoscale* **2014,** *6*, 9085-9092.

[5] Kitchin, J. R.; Nørskov, J. K.; Barteau, M. A.; Chen, J. G. *Phys. Rev. Lett.* **2004,** *93*, 156801.

[6] Yu, W.; Porosoff, M. D.; Chen, J. G. *Chem. Rev.* **2012,** *112*, 5780-5817.

[7] Zhang, J.; Lima, F. H. B.; Shao, M. H.; Sasaki, K.; Wang, J. X.; Hanson, J.; Adzic, R. R. *J. Phys. Chem. B* **2005,** *109*, 22701-22704.

[8] Toyoda, E.; Jinnouchi, R.; Ohsuna, T.; Hatanaka, T.; Aizawa, T.; Otani, S.; Kido, Y.; Morimoto, Y. *Angew. Chem., Int. Ed.* **2013,** *52*, 4137-4140.

[9] Xie, S.; Choi, S.-I.; Lu, N.; Roling, L. T.; Herron, J. A.; Zhang, L.; Park, J.; Wang,

J.; Kim, M. J.; Xie, Z.; Mavrikakis, M.; Xia, Y. *Nano Lett.* **2014,** *14*, 3570-3576.

[10] Marković, N. M.; Schmidt, T. J.; Stamenković, V.; Ross, P. N. *Fuel Cells* **2001,** *1*, 105-116.

[11] Rylander, P. *Catalytic Hydrogenation over Platinum Metals*. Academic Press Inc: New York, NY, 1967.

[12] Furstner, A. *Chem. Soc. Rev.* **2009,** *38*, 3208-3221.

[13] Fouladvand, S.; Skoglundh, M.; Carlsson, P.-A. *Chem. Eng. J.* **2016,** *292*, 321-325.

[14] Joo, S. H.; Park, J. Y.; Tsung, C.-K.; Yamada, Y.; Yang, P.; Somorjai, G. A. *Nat. Mater.* **2009,** *8*, 126-131.

[15] Xiong, Y.; Xia, Y. *Adv. Mater.* **2007,** *19*, 3385-3391.

[16] Park, J.; Zhang, L.; Choi, S.-I.; Roling, L. T.; Lu, N.; Herron, J. A.; Xie, S.; Wang, J.; Kim, M. J.; Mavrikakis, M.; Xia, Y. *ACS Nano* **2015,** *9*, 2635-2647.

[17] Wang, X.; Vara, M.; Luo, M.; Huang, H.; Ruditskiy, A.; Park, J.; Bao, S.; Liu, J.; Howe, J.; Chi, M.; Xie, Z.; Xia, Y. *J. Am. Chem. Soc.* **2015,** *137*, 15036-15042.

[18] Zhang, P.; Hu, Y.; Li, B.; Zhang, Q.; Zhou, C.; Yu, H.; Zhang, X.; Chen, L.; Eichhorn, B.; Zhou, S. *ACS Catal.* **2015,** *5*, 1335-1343.

[19] Wang, X.; Choi, S.-I.; Roling, L. T.; Luo, M.; Ma, C.; Zhang, L.; Chi, M.; Liu, J.; Xie, Z.; Herron, J. A.; Mavrikakis, M.; Xia, Y. *Nat. Commun.* **2015,** *6*.

[20] Lu, N.; Wang, J.; Xie, S.; Xia, Y.; Kim, M. J. *Chem. Commun.* **2013,** *49*, 11806-11808.

[21] Chi, M.; Wang, C.; Lei, Y.; Wang, G.; Li, D.; More, K. L.; Lupini, A.; Allard, L. F.; Markovic, N. M.; Stamenkovic, V. R. *Nat. Commun.* **2015,** *6*.

[22] Chen, H.; Yu, Y.; Xin, H. L.; Newton, K. A.; Holtz, M. E.; Wang, D.; Muller, D. A.; Abruña, H. D.; DiSalvo, F. J. *Chem. Mater.* **2013,** *25*, 1436-1442.

[23] Bonifacio, C. S.; Carenco, S.; Wu, C. H.; House, S. D.; Bluhm, H.; Yang, J. C. *Chem. Mater.* **2015,** *27*, 6960-6968.

[24] Zhang, L.; Roling, L. T.; Wang, X.; Vara, M.; Chi, M.; Liu, J.; Choi, S.-I.; Park, J.;

Herron, J. A.; Xie, Z.; Mavrikakis, M.; Xia, Y. *Science* **2015,** *349*, 412-416.

[25] Feibelman, P. J. *Phys. Rev. Lett.* **1990,** *65*, 729-732.

[26] Jin, M.; Liu, H.; Zhang, H.; Xie, Z.; Liu, J.; Xia, Y. *Nano Res.* **2010,** *4*, 83-91.

[27] Jin, M.; Zhang, H.; Xie, Z.; Xia, Y. *Energy Environ. Sci.* **2012,** *5*, 6352-6357.

[28] Kresse, G.; Furthmüller, J. *Phys. Rev. B* **1996,** *54*, 11169-11186.

[29] Kresse, G.; Furthmüller, J. *Comp. Mater. Sci.* **1996,** *6*, 15-50.

[30] Blöchl, P. E. *Phys. Rev. B* **1994,** *50*, 17953-17979.

[31] Kresse, G.; Joubert D. *Phys. Rev. B* **1999,** *59*, 1758-1775.

[32] Perdew, J. P.; Wang, Y. *Phys. Rev. B* **1992,** *45*, 13244-13249.

[33] Monkhorst, H. J.; Pack, J. D. *Phys. Rev. B* **1976,** *13*, 5188-5192.

[34] Neugebauer, J.; Scheffler, M. *Phys. Rev. B* **1992,** *46*, 16067-16080.

[35] Henkelman, G.; Uberuaga, B. P. *J. Chem. Phys.* **2000,** *113*, 9901-9904.

[36] Haynes, W. *CRC Handbook of Chemistry and Physics*. 95th ed.; CRC Press: New York, 2016.

[37] Vara, M.; Roling, L. T.; Wang, X.; Elnabawy, A. O.; Hood, Z. D.; Chi, M.; Mavrikakis, M.; Xia, Y. *ACS Nano* **2017**, *11*, 4571-4581

CHAPTER 5

UNDERSTANDING THE STABILITY OF PLATINUM-BASED NANOCAGES UNDER THERMAL STRESS USING *IN SITU* ELECTRON MICROSCOPY

5.1 Introduction

Nanocages made of precious metals are attractive for a variety of catalytic applications owing to their well-defined facets and ultrathin walls, as well as the highly open structure and thus accessibility of interior surface sites to the reactants [1, 2]. Many preliminary studies with this new class of catalytic materials have shown enhanced performance in terms of mass activity when compared with the conventional solid nanocrystals [3-6]. Despite the desirable increase in specific surface area and thereby reduced metal loading, there is still not have a good understanding of the thermal stability of such hollow and porous nanostructures relative to their solid counterparts, particularly at the elevated temperatures often required for the operation of various catalytic reactions. To better design future catalysts based on nanocages that possess not only enhanced activity but also good durability, it is therefore imperative to conduct a fundamental investigation into the stability of such hollow and porous nanostructures when subjected to thermal stress.

For this work, I chose to focus on Pt nanocages. Platinum is prized not only for its robust catalytic performance in a myriad of applications, but also for its marked thermal durability relative to other precious metals such as Au, Ag, or Pd. Additionally, many Pt-based catalytic applications are operated at elevated temperatures [7-12], which can range from slightly elevated (*e.g.*, *ca.* 80 °C for polymer electrolyte membrane fuel cells) to moderately elevated (*e.g.*, *ca.* 200 °C for phosphoric acid fuel cells) and highly elevated temperatures (*e.g.*, >300 °C for hydrogenation or dehydrogenation reactors and automotive mufflers). Given the broad range of potential uses for catalysts based on Pt nanocages, it is

of critical importance to systematically evaluate their stability under different levels of thermal stress.

To study the response of Pt nanocages under increasing thermal stress, I employed high-resolution electron microscopy integrated with *in situ* heating. This integration offers an incredibly powerful tool for monitoring the nanocrystals of interest in real time under heating up to hundreds of degrees, while maintaining the atomic-resolution capability. To this end, both high-resolution transmission electron microscopy (HRTEM) and high-angle annular dark-field scanning TEM (HAADF-STEM) have been coupled with *in situ* heating to directly image and scrutinize a myriad of catalytic nanomaterials under different conditions. For example, *in situ* microscopy was used to directly image the changes in both internal structure and morphology of Pd concave icosahedra, revealing a transformation to regular icosahedra before transitioning from a multiply-twinned into a single-crystal structure [13]. A similar technique was also employed to monitor changes to surface structure and internal crystal structure (*e.g.*, the formation of an ordered intermetallic compound for $PtCo_3$ nanocrystals within a specific temperature window) under elevated temperatures, as well as the relative thermal stability of Pd@Pt core-shell cubes *vs.* octahedra [14, 15]. Often, both surface reconstruction and subsurface alloying or structure transformation can be tracked simultaneously, and further coupled with energetic models such as density functional theory to provide more enlightening and comprehensive insights into the potential use of various complex nanostructures as viable catalysts. However, most *in situ* studies thus far have focused on solid nanocrystals, with limited investigation into or insight on the behavior of hollow nanocrystals such as nanocages. In conducting *in situ* heating studies on Pt nanocages, I aim to develop a fundamental understanding of the thermal durability of this new class of catalytic nanomaterials. By identifying both the temperature stability thresholds of Pt nanocages and the associated structural changes, I hope to not only determine the suitable operating temperatures for this new class of

catalytic nanomaterials but also offer insights for the future design of even more durable catalysts.

5.2 Results and Discussion

I chose to start with cubic nanocages. The cubic shape is particularly well-suited for *in situ* imaging as the {100} facets naturally fall directly in line with the zone axis. This makes it easy to monitor not only changes to faceting or shape but also variations in wall thickness and pore size. The cubic nanocages were synthesized from Pd@Pt core-shell templates according to a method previously reported in the literature, with an average wall thickness of six atomic layers, and small pores randomly left in the {100} side faces from the Pd etching process, as shown by the HRTEM image in Figure 5.1A [5]. To survey the breakdown mechanism or pathway that these nanocages would undertake, I heated the sample *in situ* to 400 °C in a microscope. After 20 min at this temperature, obvious changes could be observed in the cubic nanocage (Figure 5.1B). Large, window-like pores had formed over the {100} side faces, resulting in a frame-like architecture rather than a cubic cage. This effect became more pronounced after 60 min of heating (Figure 5.1C), at which point two distinct changes could be observed from the original structure: *i*) the particle had fully evolved into a nanoframe lacking the {100} side faces; and *ii*) the ridges of the particle had noticeably increased in thickness. Upon further heating up to 500 °C, the Pt nanoframe broke apart, generating into two smaller particles, and completely losing any recognizable cubic shape (Figure 5.1D).

Figure 5.2 shows atomic-resolution HAADF-STEM images of two Pt cubic nanocages upon heating to 450 °C for a much shorter period of time than in Figure 5.1, making it possible to capture the mechanism by which the nanocages changed the shape and structure. Figure 5.2A shows the two nanocages, while Figure 5.2, B-E, shows images of the lower left corner of the right nanocage over a period of 30 s. I could observe atom migration occurring in real time. Initially, I observed a bridge of atoms still connecting the

edges across the {100} side face (Figure 5.2B, denoted by the red arrow). Over the next 10 s (Figure 5.2C), the bridge became thinner as the atoms actively moved away from the side face and toward the edges and corner. After just another 5 s, enough atoms had migrated away, breaking this bridge and generating a frame structure (Figure 5.2D). The effect continued upon further heating (Figure 5.2E), clearly demonstrating the mechanistic details involved in the breakdown of a cubic nanocage.

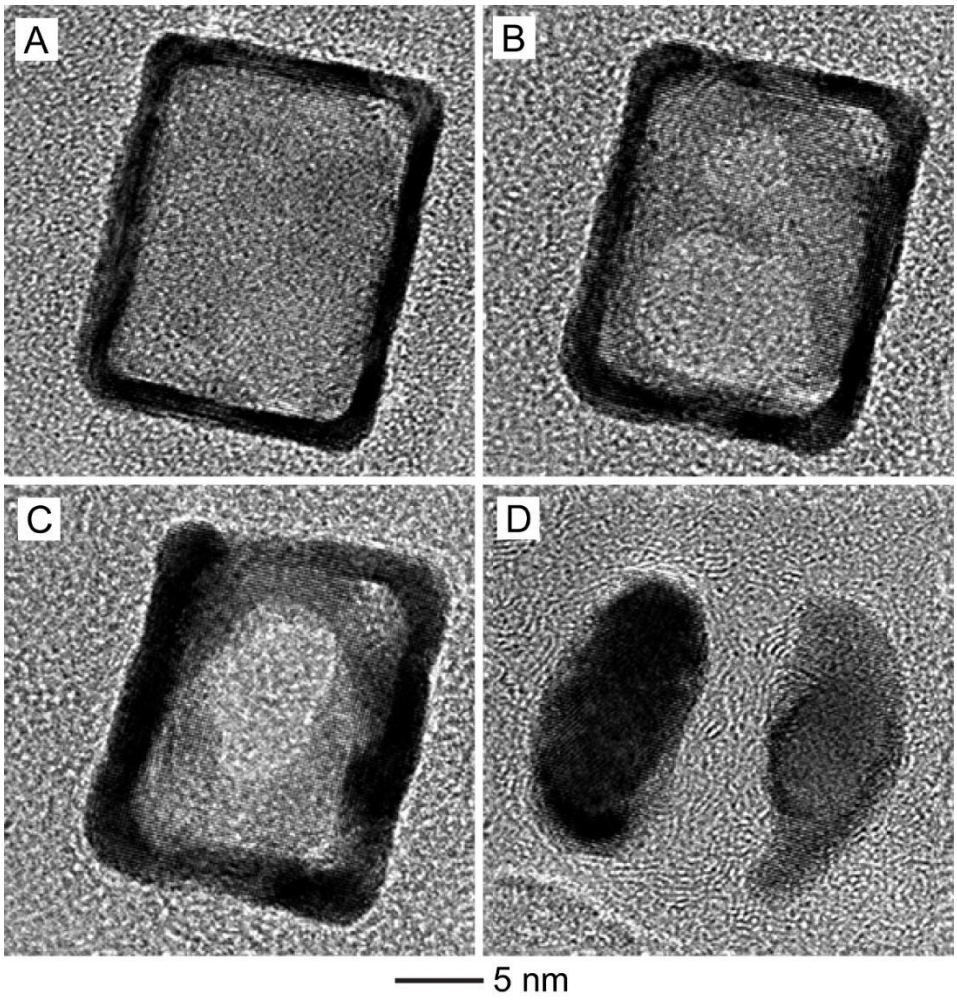

Figure 5.1. *In situ* HRTEM images of the same Pt cubic nanocage (A) before and (B-D) after different stages of heating: (B) 400 °C for 20 min, (C) 400 °C for 60 min, and (D) 500 °C for 30 min. (Reprinted with permission from [40]. Copyright 2017 Wiley-VCH.)

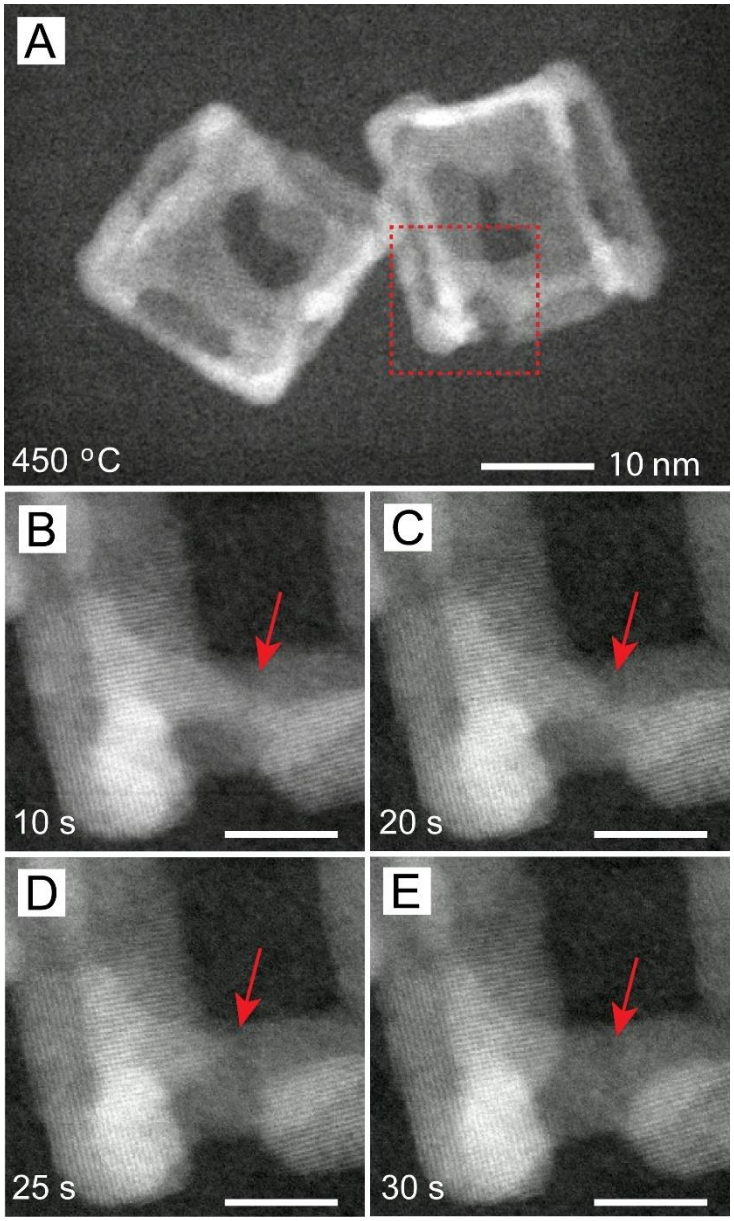

Figure 5.2. (A) HAADF-STEM image extracted from a video of two Pt cubic nanocages upon heating to 450 °C. (B, C) Atomic-resolution images recorded from the corner region of the particle marked by a red square in (A) upon heating at 450 °C for 10 and 20 s, respectively. The images clearly show the movement of surface atoms on the face of the particle that connect the edges. The atoms actively migrate away from the side face and toward the edges and corner, ultimately resulting in disappearance of the connecting layer of atoms, as denoted by the red arrows. The scale bars in (B-E) are 2 nm. (Reprinted with permission from [40]. Copyright 2017 Wiley-VCH.)

I believe that this transformation process is driven largely by thermodynamic constraints, and can be explained using an energetic consideration [16-20]. For the

formation of a nanoframe from a nanocage upon heating while supported on a substrate, the total free energy (ΔG_{total}) driving the process can generally be defined as the sum of the following two major contributions, the surface free energy ($\varepsilon_{surface}$) and the volumetric free energy (ε_{volume}):

$$\Delta G_{total} = \varepsilon_{surface} + \varepsilon_{volume} \quad (1)$$

Here, the volumetric free energy term is dependent on the bulk volume of atoms in the particle, which remains the same during this process. Therefore, to obtain a more thermodynamically favorable ΔG_{total}, the nanocage will therefore trend toward structural changes that can decrease the surface-area-to-volume ratio and thus reduce the contribution from $\varepsilon_{surface}$. From the Gibbs-Wulff theorem, I can simplify the term for the surface free energy of a nanocrystal as the following:

$$\varepsilon_{surface} = \sum_n \gamma_n A_n = \gamma_{(100)} A_{(100)} + \gamma_{(110)} A_{(110)} + \gamma_{(111)} A_{(111)} + \cdots \quad (2)$$

Wherein γ_n is the specific surface energy term for an expressed facet on the nanocrystal surface, and A_n is the total surface area for that given crystal facet. Because the Pt nanocages possess a tremendously large surface area for their expressed facets (possessing both interior and exterior surfaces), the total surface free energy of a nanocage is much higher than that of a solid counterpart of the same dimensions [21, 22]. In order to decrease the total energy of the system, the nanocages therefore follow a thermodynamically favorable pathway of both trying to minimize A_n (to lower $\varepsilon_{surface}$), which can be understood as trying to decrease the surface-area-to-volume ratio. Through the migration of atoms from side faces to edges, the nanocages substantially lower the A_n, leading to a favorable ΔG_{total} for nanoframe formation. Finally, due to the tremendous thermal energy in the system, the frames fracture into smaller particles, likely because of a substrate-pinning

process similar to the Rayleigh instability observed in the melting of supported nanowires [23].

Figure 5.3 shows a schematic illustration of the pathway that transforms the original cubic nanocage into a nanoframe and then two smaller particles. Using the cubic nanocage as an example, I can conclude that the initial pores left behind on the surface of the nanocage from Pd etching first grow together into a larger single pore in an effort to decrease A_n upon extensive heating. Subsequently, further atom migration continues as atoms move away from faces and toward the edges and corners of the nanocage, transforming the particle into a nanoframe with a substantially lower surface area (approximately 4-5 times lower). At this point, the edges of the particle are noticeably thickened due to the migration of atoms. Under continuous thermal stress, the nanoframe then fragments and loses its initial shape entirely, breaking apart into smaller pieces. After this point, the particles will eventually become molten and aggregate into large particles to further thermodynamic stabilization.

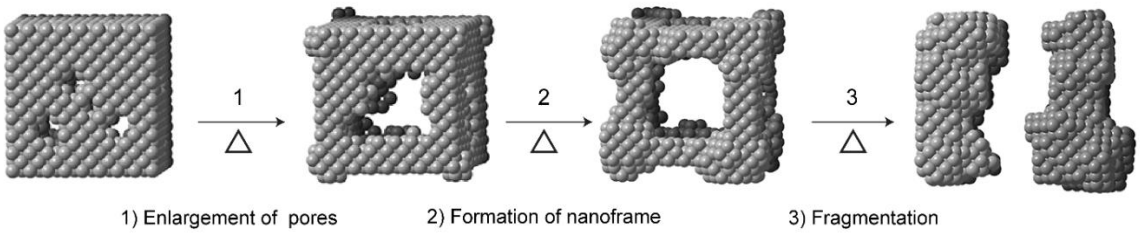

Figure 5.3. Schematic illustration of the process by which a Pt nanocage breaks down under thermal stress, using a cubic nanocage as an example. In the first step, pre-existing pores on the surface of the nanocage are enlarged. In the second step, the edges and corners are thickened due to the migration of atoms away from the pore-decorated side faces. This results in the formation of a nanoframe with open side faces. Finally, under further heating, the frame fractures and breaks apart into smaller pieces. (Reprinted with permission from [40]. Copyright 2017 Wiley-VCH.)

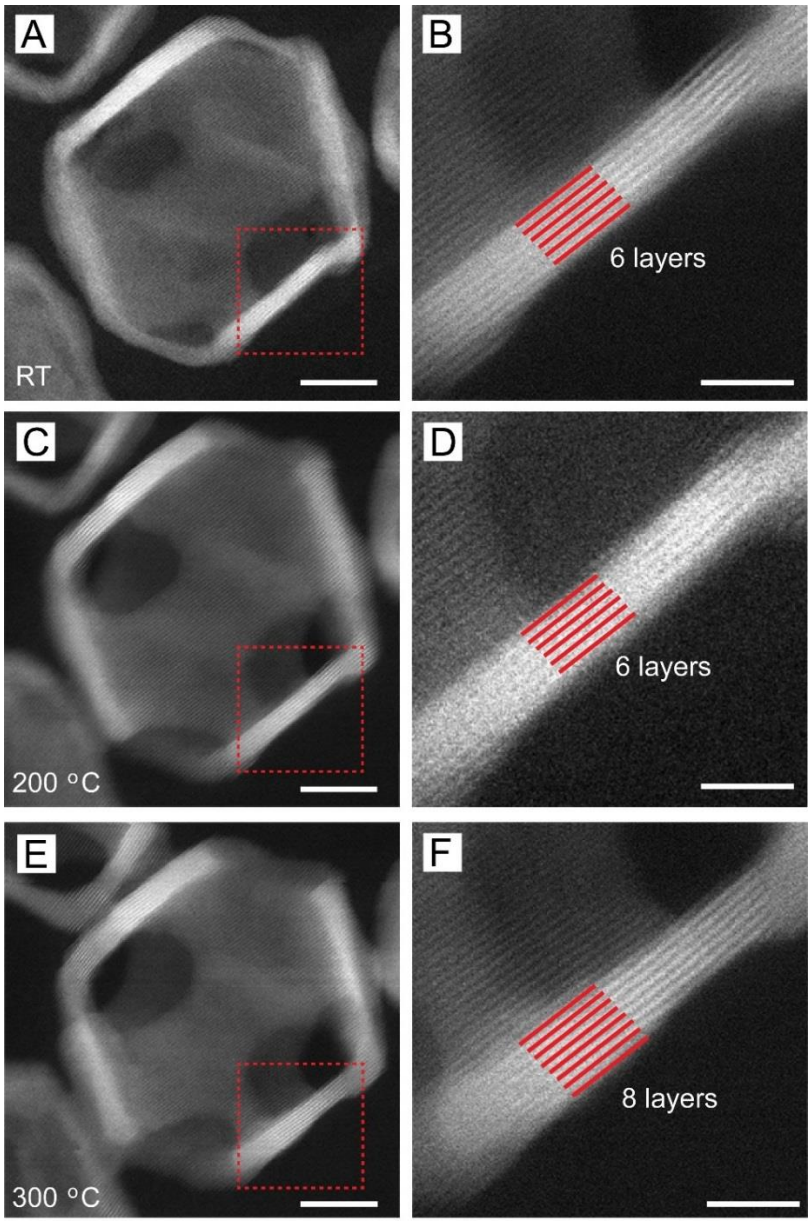

Figure 5.4. HAADF-STEM images of the same Pt octahedral nanocage (A, B) before and (C-F) after various stages of heating: (C, D) 200 ºC for 4 h and (E, F) 300 ºC for another 1 h. The magnified images in (B, D, F) were taken from the areas marked by the red square in (A, C, E), respectively. The images in (B) and (D) clearly display an edge thickness of six atomic layers while the image in (F) displays an edge thickness of eight atomic layers. The scale bars in (A, C, E) are 5 nm while the scale bars in (B, D, F) are 2 nm. (Reprinted with permission from [40]. Copyright 2017 Wiley-VCH.)

With the above pathway in mind, I also decided to conduct an extended study by focusing on Pt octahedral and icosahedral nanocages. It has been shown in the literature

that Pt nanocrystals enclosed by {111} facets have markedly enhanced activity toward a variety of catalytic reactions, making octahedral and icosahedral nanocages much more attractive candidates for investigating thermal stability [24-27]. The surfaces of both nanocages are predominantly covered by {111} facets. However, the octahedron is a single-crystal structure bound with eight {111} side faces and six vertices, whereas the icosahedron is a multiply-twinned structure bound by twenty {111} side faces, twelve vertices, and thirty twin boundaries. Prior testing has confirmed greater catalytic activities for multiply-twinned structures such as icosahedra relative to single-crystal counterparts, but the strain from twin boundaries may compromise the thermal stability.

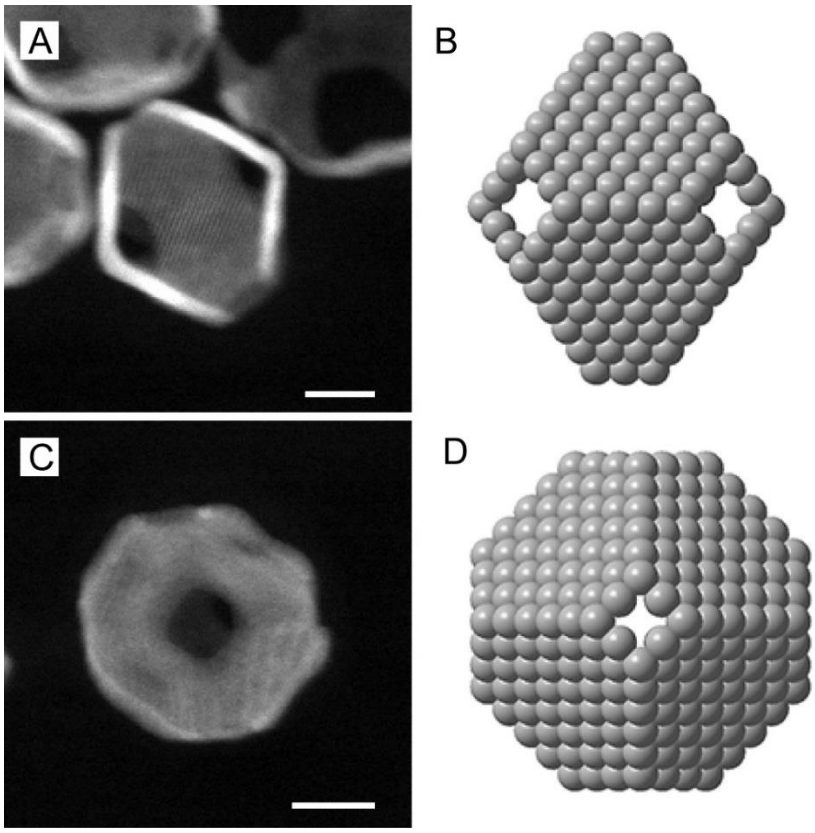

Figure 5.5. HAADF-STEM images and the corresponding three-dimensional projection models of a Pt octahedral nanocage with all the vertices etched away: (A, B) the projection of an octahedral nanocage when it is laying along one of the equatorial edges, and (C, D) the projection of an octahedral nanocage when it is laying on one of the etched away vertices. These images and models confirm that all the six vertices were etched away to form holes in the octahedral nanocages. The scale bars in (A) and (C) are both 10 nm. (Reprinted with permission from [40]. Copyright 2017 Wiley-VCH.)

At room temperature, I could easily resolve the atomic structure of the octahedral nanocage with an edge length of about 18 nm (Figure 5.4A). Six large pores were left behind from the Pd etching process, located on each of the original {100} vertices (Figure 5.5). The edges of the octahedral nanocage were measured to be approximately six atomic layers thick (Figure 5.4B), and the {111} facets of the particle remained largely intact. A quick heating test of the octahedral cage sample to 400 °C showed a markedly faster breakdown of the octahedra compared to the cubes, so I therefore decided to do a more gradual series of heating steps to evaluate the octahedra (Figure 5.6). I first heated the octahedral nanocage to 200 °C (Figure 5.4C). Even after 4 h, no substantial changes was discerned, with the edge thickness remaining at six atomic layers (Figure 5.4D). As the octahedra appeared to be stable at this operating temperature, I then increased the temperature to 300 °C. Upon heating at 300 °C for one hour, changes began to appear (Figure 5.4E). At this point, enlargement of pores seemed to have occurred. Indeed, upon imaging one of the edges of the nanocage (Figure 5.4F), I found that its thickness had increased from an average of six to eight atomic layers, indicating active atom migration during the heating process. As expected, further increasing the temperature and heating then led to fracturing and collapse of the hollow frames into smaller pieces (Figure 5.7). Notably, while the octahedral shape and the expressed facets were both kept intact even upon heating at 300 °C, I still consider this a point of deformation as changes in edge thickness and pore size (and thus A_n) are clearly recorded. This indicates not only loss of the nanocage structure (as it then continues to transform into a nanoframe), but also potential loss of activity with this small change to the surface structure. Nonetheless, it should be pointed out that while thickening was observed at 300 °C, the active {111} facets were still largely preserved, suggesting that the catalyst could be used up to this temperature.

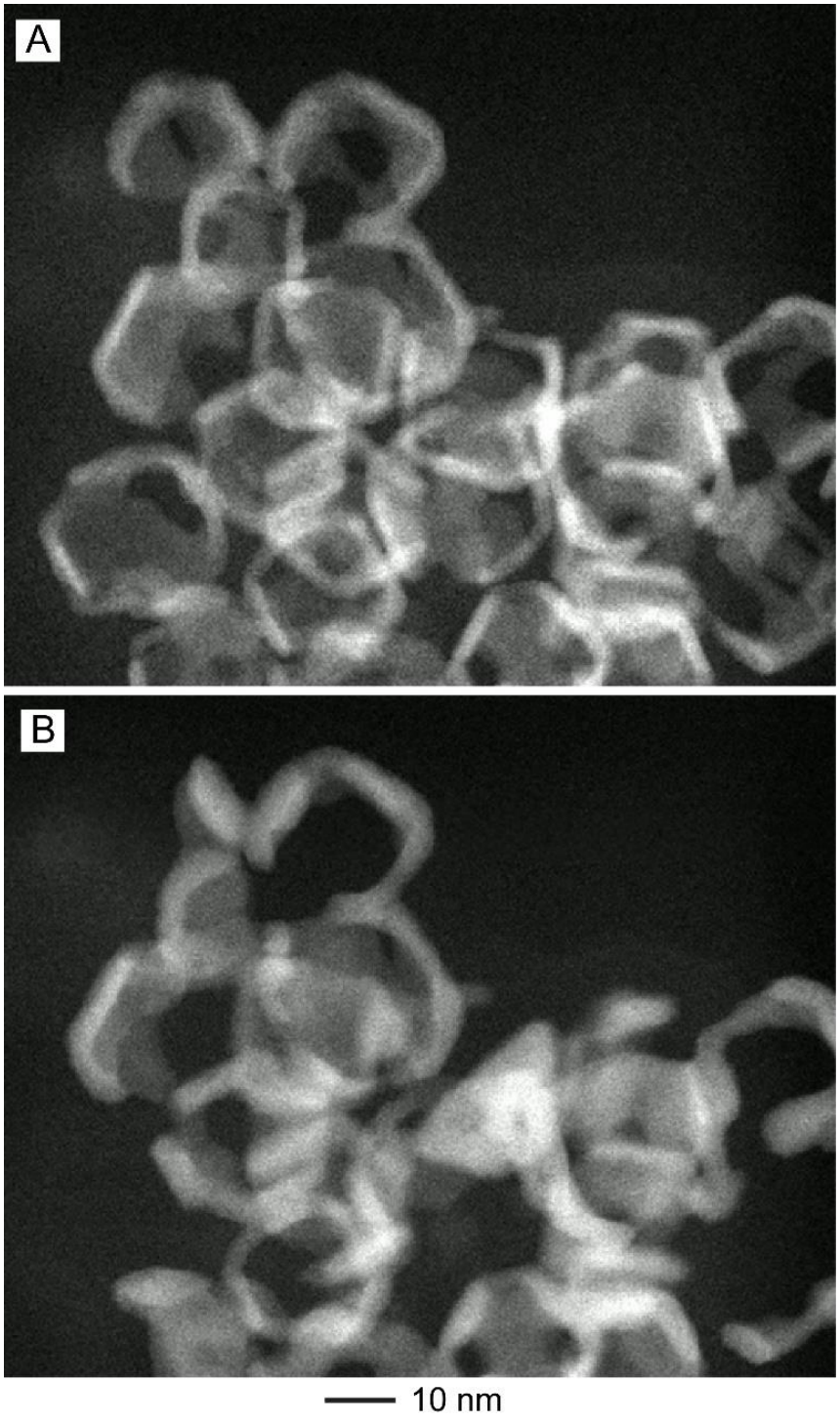

Figure 5.6. HAADF-STEM images of octahedral nanocages at (A) room temperature, and (B) after heating at 400 °C for only 10 min. This demonstrates the lower stability of the octahedra *versus* the cubes (Reprinted with permission from [40]. Copyright 2017 Wiley-VCH.)

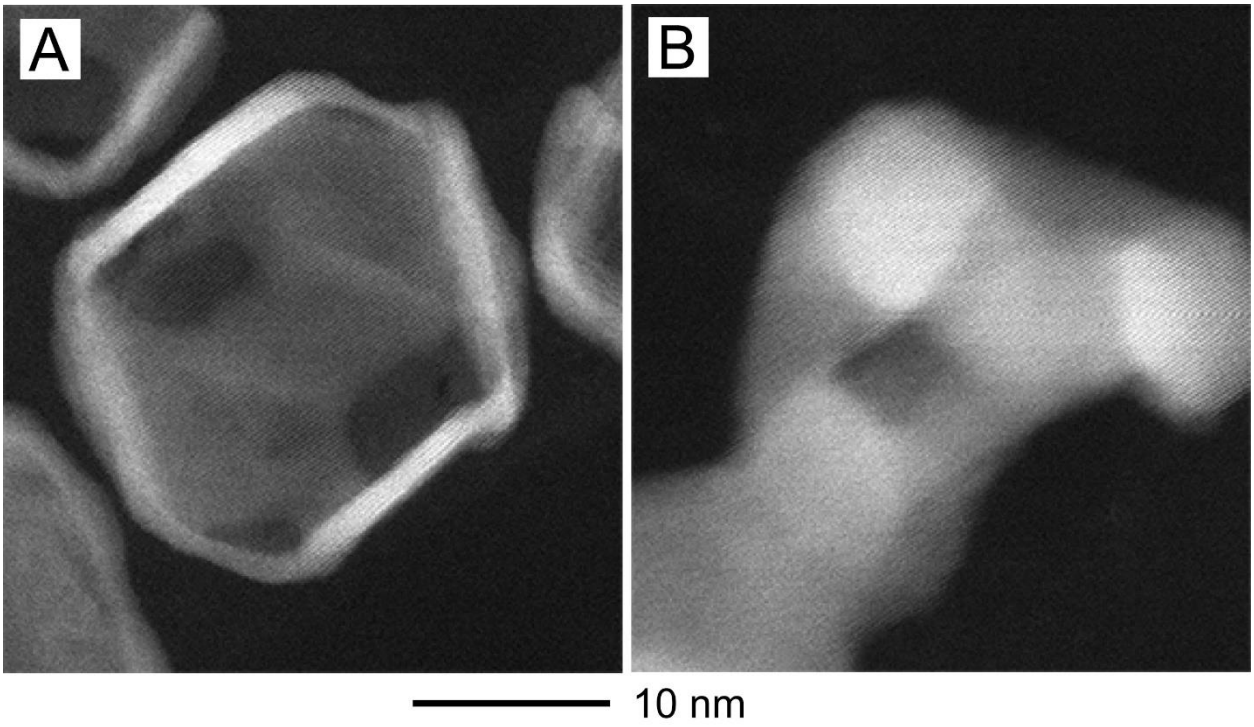

Figure 5.7. HAADF-STEM images of a Pt octahedral nanocage at (A) room temperature and (B) after heating at 500 °C for 10 min. During the heating process, the hollow structure began to break into smaller particles. (Reprinted with permission from [40]. Copyright 2017 Wiley-VCH.)

Interestingly, in a prior thermal stability study between Pd@Pt core-shell octahedra and cubes, the {111}-enclosed octahedra were found to have substantially increased facet and shape stability compared to the {100} enclosed cubes [15]. For the case of nanocages, I believe that the octahedra possess lower stability as compared to the cubes due to the location of pores derived from the etching process used to generate Pt nanocages from the Pd@Pt core-shell nanocrystals. For the etching of the Pd core, I typically employ a chemical etchant based on $FeCl_3$ under acidic conditions, wherein Fe(III) selectively etches the Pd core through a redox reaction, leaving the Pt shell intact. This process, however, does not appreciably occur without the addition of excess Br^- into the etchant mixture. It has been well established in the literature that Br^- binds very strongly to Pd(II) to form $[PdBr_x]^{2-x}$ complexes with high stability factors [28-30]. While Br^- does not directly act as

an etchant, it helps to initiate and promote the etching process by forming $[PdBr_x]^{2-x}$ with the newly oxidized Pd, thus accelerating the etching process. It is important to note that Br^- is known to selectively cap the {100} facets of both Pd and Pt [31-32]. In the case of Pd@Pt cubes and octahedra, the selective adsorption leads to the accumulation of Br^- ions on the six faces of a Pd@Pt cube and the six vertices of a Pd@Pt octahedron. As a result of the selective {100} capping associated with the role of Br^- in etching, the holes tend to appear on the side faces of a cube or the vertices of an octahedron, likely initiated from localized high-energy surface defect sites such as kinks, steps, or vacancies, or at locations of substitution between Pd and Pt [5]. Some of the Br^- ions could possibly remain on the {100} facets of a Pt cubic nanocage, playing a certain role in affecting its thermal stability. Recently, an *in situ* TEM study on Pt nanoparticles demonstrated that the reconstruction of the crystal surface had a dependence on adsorbed CO [33]. However, it is very difficult to quantify, or just identify, the Br^- ions adsorbed on the surface of Pt nanocages, making it almost impossible to elucidate their possible impact on the thermal stability of the nanocages.

Importantly, studies in crystal film heating and dewetting have shown a strong dependence of hole growth and hole edge atom retraction rates on the localized strain energy and thus the location of the holes [16]. This results in a hole curvature-driven growth that accelerates diffusion of atoms and subsequent growth of holes when the pores are present along crystal edges, corners, or other strain boundaries. For the case of octahedra, the pores are generated at the vertices instead of faces, leading to the observed thickening and pore growth at temperatures lower than the case of cubes. In turn, this observation suggests that the thermal stability of resultant hollow structures can be enhanced by controlling where the pores from Pd etching are formed. For example, in the case of octahedra, developing a Pd etchant that instead targets pore formation over the {111} facets rather than the {100} facets (thus leaving small pores on the faces rather than large ones at the corners) would lead to a more stable structure that may be durable up to higher

temperatures [34]. In the case of twinned structures such as Pt icosahedral nanocages, the impact of twin boundaries and strain on pore formation is less well understood, and it is unclear what controls the positions of the etching pores on the surface. However, the additional surface strain associated with twin defects (which also contributes to the surface free energy, $A_t\gamma_t$) for hole growth and edge retraction will therefore likely contribute to a lower hole stability than with single-crystal nanocages [16, 20, 35].

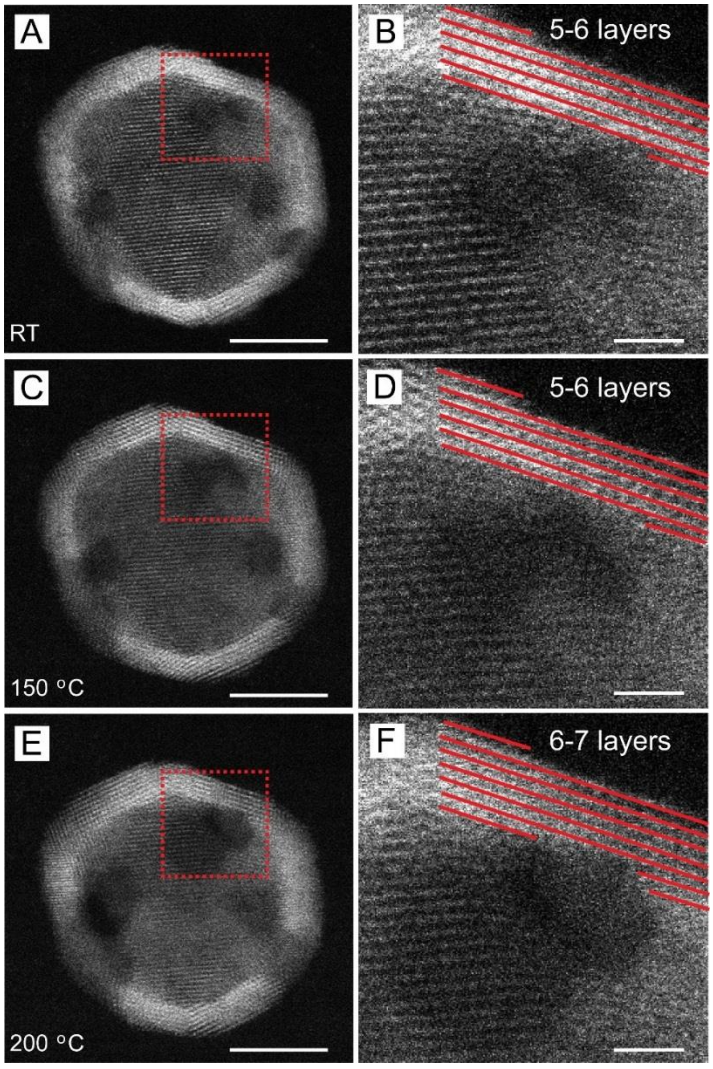

Figure 5.8. HAADF-STEM images of the same Pt icosahedral nanocage (A, B) before and (C-F) after various stages of heating: (C, D) 150 ºC for 4 h and (E, F) 200 ºC for another 4 h. The magnified images in (B, D, F) were taken from the areas marked by the red square in (A, C, E), respectively. The images in (B) and (D) clearly display an edge thickness of 5-6 atomic layers while the image in (F) displays an edge thickness of 6-7 atomic layers.

The scale bars in (A, C, E) are 5 nm while the scale bars in (B, D, F) are 1 nm. (Reprinted with permission from [40]. Copyright 2017 Wiley-VCH.)

Figure 5.8 shows a typical Pt icosahedral nanocage at room temperature, with an average diameter of 12 nm and an average edge thickness of 5−6 atomic layers (Figure 5.8B). Several small pores from Pd etching could be seen across the surface of the particle. As stated previously, the icosahedral nanocages possess a high surface strain energy from the multiple twin boundaries, and are also substantially smaller than their octahedral counterpart (12 nm in size *vs.* 19 nm in edge length). As such, I expected to observe depressed thermal stability and enhanced hole growth relative to the larger, single-crystal octahedra. For that reason, I heated first at 150 °C. After 4 h (Figure 5.8C), no substantial change was detected in the original Pt icosahedral structure, with the edge thickness remaining at 5−6 layers (Figure 5.8D). I then heated the sample at 200 °C for 4 h, where the icosahedral nanocage appeared to stay intact at low magnification (Figure 5.8E). However, atomic resolution analysis revealed that morphological changes had begun to occur in this time period. The pores present on the surface of the nanocage were enlarged, indicating that atomic migration and hole growth had occurred. Indeed, further examination of the edges of the icosahedron showed an increase in atomic layer thickness, suggesting a mechanistic change similar to what was seen in the octahedral sample (Figure 5.8F). As predicted, atoms began to migrate from pores and toward the edges of the particle to lower the surface free energy, before ultimately breaking apart into smaller Pt particles upon more extensive heating (Figure 5.9). Clearly, the smaller, multiply-twinned particles were less stable than the larger, single-crystal octahedral nanocages, and therefore began to experience active atom migration at an even lower temperature. While icosahedral nanocages have demonstrated markedly improved activity toward several catalytic reactions, my observations indicate that their durability will be more compromised by thermal stress compared to other morphologies [36-39]. These results provide critical information in designing future catalysts with not only enhanced reactivity but also better

durability and further highlight the importance of evaluating the thermal stability whenever new nanomaterials are developed for enhanced catalytic applications. Going forward, I believe if the pore location can be more finely tuned and the atom migration process subsequently minimized, I can vastly improve and expand upon the potential reactions for this promising class of Pt-based nanocatalysts.

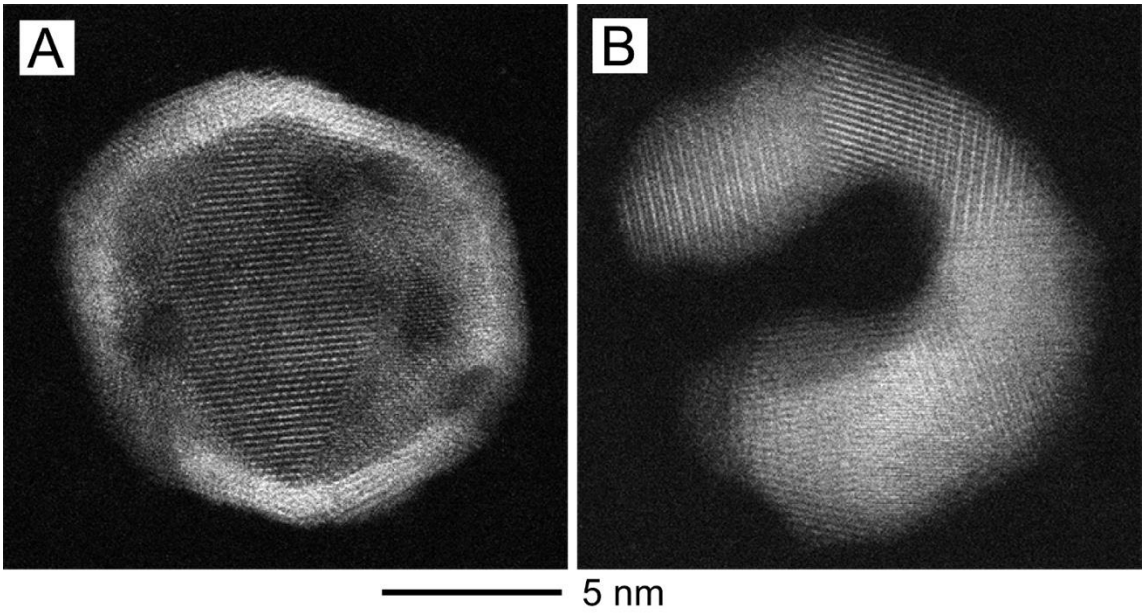

Figure 5.9. HAADF-STEM images of a Pt icosahedral nanocage at (A) room temperature and (B) after heating at 500 °C for 10 min. During the heating process, the hollow structure began to break apart into smaller particles. (Reprinted with permission from [40]. Copyright 2017 Wiley-VCH.)

5.3 Conclusion

I have systematically evaluated the thermal stability and structural behavior of Pt-based nanocages with three different shapes. Their thermal durability was observed to increase in the order of icosahedra < octahedra < cubes, wherein the more stable structures tend to maintain their ultrathin wall thickness and facets under greater thermal stress. All these nanocages underwent the same thermodynamic process that enlarged the pores to form nanoframes when subjected to thermal stress in an effort to minimize the surface free

energy. This transformation will limit the usage of such catalysts in applications involving elevated temperatures. Nevertheless, my studies prove their excellent thermal stability for a multitude of catalytic reactions that are operated at moderate temperatures, such as polymer electrolyte membrane fuel cells (typically run at ~80 °C). For reactions where the nanoframe derivatives of the nanocages are still highly active, the change in shape may still lend itself toward enhanced durability. If control can be developed over not only the size, shape, and wall thickness of such hollow nanostructures, but also the etching process and thus the locations of the pores, it may be possible to further expand the range of temperatures this class of catalytic nanomaterials can be effectively used for.

5.4 Experimental Section

Chemicals and Materials. L-ascorbic acid (AA, 99%), poly(vinyl pyrrolidone) (PVP, M_w≈55,000), potassium bromide (KBr, 98%), iron chloride (Fe(III)Cl_3, 97%), hydrochloric acid (HCl, 37%), and sodium hexachloroplatinate(IV) hexahydrate (Na_2PtCl_6•$6H_2O$), 98%) were all purchased from Sigma-Aldrich. Formaldehyde (HCHO) was obtained from Fisher Scientific, ethylene glycol (EG, 99%) was obtained from J.T. Baker, ethanol (200 proof, KOPTEC) was obtained from VWR, and sodium tetrachloropalladate (Na_2PdCl_4, 36% Pd) was obtained from Acros Organics. All chemicals were used as received. Deionized (DI) water with a resistivity of 18.2 MΩ cm at room temperature was used throughout the experiments.

Synthesis of Pt Nanocages. The Pt nanocages with cubic [5], octahedral [5], and icosahedral shapes [38], respectively, were all synthesized from Pd@Pt core-shell nanocrystals according to previously published literature. All of them had a wall thickness of approximately six atomic layers.

***In situ* Electron Microscopy Studies.** The HRTEM images shown in Figure 1 for the cubic nanocages were captured on a Cs-corrected FEI Titan 80/300 kV TEM/STEM microscope at Oak Ridge National Laboratory (ORNL), using a Protochips Aduro heating

holder. The HAADF-STEM images in all other figures were acquired using a cold-field emission Hitachi HD2700 aberration-corrected STEM operated at 200 kV, using the Hitachi Blaze heating holder. Prior to electron microscopy imaging, all samples were treated in the Hitachi ZONE cleaner for 30 min each side at a pressure setting of 70 to remove any PVP adsorbed on the nanocages.

5.5 Notes

Part of this chapter is adapted from the paper "Understanding the Stability of Pt-based Nanocages under Thermal Stress Using *in situ* Electron Microscopy" published in *ChemNanoMat* [40].

5.5 References

[1] Prieto, G.; Tüysüz, H.; Duyckaerts, N.; Knossalla, J.; Wang, G.-H.; Schüth, F. *Chem. Rev.* **2016,** *116*, 14056-14119.

[2] Yu, L.; Hu, H.; Wu, H. B.; Lou, X. W. *Adv. Mater.* **2017,** *29*, 1604563

[3] Zeng, J.; Zhang, Q.; Chen, J.; Xia, Y. *Nano Lett.* **2010,** *10*, 30-35.

[4] Hong, J. W.; Kang, S. W.; Choi, B.-S.; Kim, D.; Lee, S. B.; Han, S. W. *ACS Nano* **2012,** *6*, 2410-2419.

[5] Zhang, L.; Roling, L. T.; Wang, X.; Vara, M.; Chi, M.; Liu, J.; Choi, S.-I.; Park, J.; Herron, J. A.; Xie, Z.; Mavrikakis, M.; Xia, Y. *Science* **2015,** *349*, 412-416.

[6] Shao, F.-Q.; Feng, J.-J.; Yang, Z.-Z.; Chen, S.-S.; Yuan, J.; Wang, A.-J. *Int. J. Hydrog. Energy* **2017**.

[7] Rylander, P., *Catalytic Hydrogenation over Platinum Metals*. Academic Press Inc: New York, NY, 1967.

[8] Joo, S. H.; Park, J. Y.; Tsung, C.-K.; Yamada, Y.; Yang, P.; Somorjai, G. A. *Nat. Mater.* **2009,** *8*, 126-131.

[9] Fouladvand, S.; Skoglundh, M.; Carlsson, P.-A. *Chem. Eng. J.* **2016,** *292*, 321-325.

[10] Marković, N. M.; Schmidt, T. J.; Stamenković, V.; Ross, P. N. *Fuel Cells* **2001,** *1*, 105-116.

[11] Martin, S.; Li, Q.; Jensen, J. O. *J. Power Sources* **2015,** *293* (Supplement C), 51-56.

[12] Celik, M.; Genc, G.; Elden, G.; Yapici, H. *EPJ Web of Conferences* **2016,** *114*, 02010.

[13] Gilroy, K. D.; Elnabawy, A. O.; Yang, T.-H.; Roling, L. T.; Howe, J.; Mavrikakis, M.; Xia, Y. *Nano Lett.* **2017,** *17*, 3655-3661.

[14] Chi, M.; Wang, C.; Lei, Y.; Wang, G.; Li, D.; More, K. L.; Lupini, A.; Allard, L. F.; Markovic, N. M.; Stamenkovic, V. R. *Nat. Commun.* **2015,** *6*, 8925.

[15] Vara, M.; Roling, L. T.; Wang, X.; Elnabawy, A. O.; Hood, Z. D.; Chi, M.; Mavrikakis, M.; Xia, Y. *ACS Nano* **2017,** *11*, 4571-4581.

[16] Thompson, C. V. *Annu. Rev. Mater. Res.* **2012,** *42*, 399-434.

[17] Thanh, N. T. K.; Maclean, N.; Mahiddine, S. *Chem. Rev.* **2014,** *114*, 7610-7630.

[18] Tran, R.; Xu, Z.; Radhakrishnan, B.; Winston, D.; Sun, W.; Persson, K. A.; Ong, S. P. *Sci. Data* **2016,** *3*, 160080.

[19] Somorjai, G. A.; Li, Y., *Introduction to Surface Chemistry and Catalysis*. 2nd ed.; John Wiley & Sons, Inc.: Hoboken, NJ, **2010**.

[20] Patala, S.; Marks, L. D.; Olvera de la Cruz, M. *J. Phys. Chem. Lett.* **2013,** *4*, 3089-3091.

[21] Lu, H. M.; Jiang, Q. *J. Phys. Chem. B* **2004,** *108*, 5617-5619.

[22] Holec, D.; D. Fischer, F.; Vollath, D. *arXiv* 2014.

[23] Molares, M. E. T.; Balogh, A. G.; Cornelius, T. W.; Neumann, R.; Trautmann, C. *Appl. Phys. Lett.* **2004,** *85*, 5337-5339.

[24] Somorjai, G. A.; Zaera, F. *J. Phys. Chem.* **1982,** *86*, 3070-3078.

[25] Marković, N. M.; Adžić, R. R.; Cahan, B. D.; Yeager, E. B. *J. Electroanal. Chem.* **1994,** *377*, 249-259.

[26] Narayanan, R.; El-Sayed, M. A. *J. Am. Chem. Soc.* **2004,** *126*, 7194-7195.

[27] Narayanan, R.; El-Sayed, M. A. *Nano Lett.* **2004,** *4*, 1343-1348.

[28] Elding, L. *Inorg. Chim. Acta* **1978**, *28*, 55-262.

[29] Richens, D. T. *Chem. Rev.* **2005,** *105*, 1961-2002.

[30] Timoshkin, A. Y.; Kudrev, A. G. *Russ. J. Inorg. Chem.* **2012,** *57*, 1362-1370.

[31] Lee, H.; Habas, S. E.; Kweskin, S.; Butcher, D.; Somorjai, G. A.; Yang, P. *Angew. Chem. Int. Ed.* **2006,** *45*, 7824-7828.

[32] Xiong, Y.; Xia, Y. *Adv. Mater/* **2007,** *19*, 3385-3391.

[33] Avanesian, T.; Dai, S.; Kale, M. J.; Graham, G. W.; Pan, X.; Christopher, P. *J. Am. Chem. Soc.* **2017,** *139*, 4551-4558.

[34] Chen, J.; McLellan, J. M.; Siekkinen, A.; Xiong, Y.; Li, Z.-Y.; Xia, Y. *J. Am. Chem. Soc.* **2006,** *128*, 14776-14777.

[35] Srolovitz, D. J.; Goldiner, M. G. *JOM* **1995,** *47*, 31-36.

[36] Wu, J.; Qi, L.; You, H.; Gross, A.; Li, J.; Yang, H. *J. Am. Chem. Soc.* **2012,** *134* (29), 11880-11883.

[37] Wang, X.; Choi, S.-I.; Roling, L. T.; Luo, M.; Ma, C.; Zhang, L.; Chi, M.; Liu, J.; Xie, Z.; Herron, J. A.; Mavrikakis, M.; Xia, Y. *Nat. Commun.* **2015,** *6*, 7594.

[38] He, D. S.; He, D.; Wang, J.; Lin, Y.; Yin, P.; Hong, X.; Wu, Y.; Li, Y. *J. Am. Chem. Soc.* **2016,** *138*, 1494-1497.

[39] Wang, X.; Figueroa-Cosme, L.; Yang, X.; Luo, M.; Liu, J.; Xie, Z.; Xia, Y. *Nano Lett.* **2016,** *16*, 1467-1471.

[40] Vara, M.; Wang, X.; Howe, J.; Chi, M.; Xia, Y. *ChemNanoMat* **2017,** *just accepted*

CHAPTER 6

CONCLUSIONS AND FUTURE DIRECTIONS

6.1 Conclusions

This dissertation covers a number of approaches toward not only the controlled synthesis of metal-based nanocrystals, but also a systematic evaluation of their potential for industrial applications. I began by developing a room-temperature, photochemical method for the synthesis for Pd cubic nanocrystals. The success of this method relied on utilizing UV-vis light to promote the reduction of $[PdBr_4]^{2-}$ by AA even at room temperature, whereas the reduction would otherwise not appreciably occur. The excess Br^- ions present in solution resulted in the coverage of {100} facets and thus the formation of 12-nm Pd cubes. Atomic-resolution electron microscopy revealed the presence of steps and terraces across the side faces of the Pd cubes produced through this method. As the surface adatom diffusion rate is directly controlled by the reaction temperature, the newly deposited atoms had substantially reduced surface diffusion in my synthesis, resulting in the formation of cube-like Pd nanocrystals with highly terraced faces. By subjecting the Pd cube-like nanocrystals to a thermal treatment post-synthesis, I could transform them into Pd nanocubes with smooth faces and truncated corners without atomic steps and terraces. In evaluating the Pd nanocrystals for FAO, I found that the transformed cubes with truncated corners performed better that the terraced cube-liked nanocrystals, and that regular Pd cubes with sharp corners performed the best. This suggested that the low-coordinated surface atoms present on the terraced faces of the photochemically-synthesized nanocubes may be detrimental to catalysis due to overbinding with reactants or intermediate species.

Continuing to investigate Pd nanocrystal synthesis, I designed a room-temperature method for the production of Pd concave nanocubes, with an average edge length (from

corner to adjacent corner) of 18 nm. By utilizing a reductant of the appropriate reducing power (sodium ascorbate) and manipulating the kinetics at room temperature, I was able to generate highly concave nanocubes, a synthesis that has previously only been reported through two-pot, seed-mediated growth. Analysis of the reduction kinetics revealed a two-step reduction regime that was critical to the formation of the final product. First, the sodium ascorbate was sufficiently strong to induce the reduction of $[PdBr_4]^{2-}$ into the appropriate regime for the formation of single-crystal seeds. As seed concentration increased and metal precursor concentration decreased, the kinetics switched from solution reduction and nucleation to autocatalytic surface reduction, and naturally enabled a seed-mediated growth mechanism. The {100} selective capping by excess Br^- blocked the addition of new atoms onto the cubic faces of the seeds, promoting growth in the ⟨111⟩ direction. However, the sluggish adatom surface diffusion rates at room temperature favored the pile-up of new atoms at the corners before they could diffuse across the faces, leading to the production of concave Pd cubes. Additionally, the low energy at room-temperature favored a symmetry-breaking growth mode, resulting in asymmetric corner growth across the Pd concave cubes. The kinetic considerations of room-temperature conditions combined with appropriate precursor choices open the pathway toward the one-port synthesis of more complex nanocrystals geometries going forward.

Next, I chose to systematically investigate the behavior of Pt-based nanocatalysts using *in situ* high-resolution electron microscopy. Specifically, I synthesized Pd@Pt_{4L} core-shell cubic and octahedral nanocrystals, which are of intense interest for ORR and many other catalytic reactions at elevated temperatures. My study indicated that both nanocrystal morphologies are stable for usage up to 400 °C. I found that the Pd@Pt_{4L} octahedra enclosed by {111} facets maintained their shape stability up to 900 °C, whereas the Pd@Pt_{4L} cubes enclosed by {100} facets began to round and lose their expressed facet definition at 500 °C. Conversely, the cubes maintained the core-shell distinction up to 800 °C, a higher temperature than cubic shape deformation, whereas the octahedra underwent

interdiffusion and alloying at 600 °C (at a lower temperature than octahedral shape deformation, at 900 °C). I was able to rationalize these shape-dependent trends through the DFT calculations by my collaborators. Analysis showed more favorable formation of subsurface vacancies in {111} facets *versus* {100} facets, leading to alloying at lower temperatures for the case of octahedra. Conversely, modelling indicated a much higher activation energy barrier to moving a surface edge atom to the side face for the {111} facet enclosed octahedra compared to the {100} cubes, leading to the higher expressed facet stability for the case of octahedra.

Finally, I performed a similar evaluation of Pt-based nanocages to study their thermal stability and breakdown behavior. I studied Pt cubic, octahedral, and icosahedral nanocages, with an average edge length of 18 nm, 19 nm, and a diameter of 12 nm, respectively. The nanocages were synthesized by etching away Pd from Pd@$Pt_{5\text{-}6L}$ templates, leaving an average wall thickness of 6 atomic layers of Pt, and making them highly attractive candidates for Pt-based catalytic reactions due to the high surface area (from the interior and exterior surfaces) and the low mass loading (from the high Pt dispersion). *In situ* electron microscopy analysis revealed that the nanocrystal stability increased in the following order: icosahedra < octahedra < cubes. I found that the nanocages all underwent the same transformation into nanoframes under thermal stress, which can be explained using thermodynamic considerations. Pores left over from etching favored hole enlargement and atom migration toward the edges, lowering the surface free energy contribution and creating a more favorable total free energy change. The lower thermal stability of octahedra *versus* cubes may also be impacted by initial pore location from Pd etching. The octahedra possessed pores on the vertices rather than faces, which may impact the hole enlargement rate from localized strain. Development of a better control over the location of pores left from Pd etching could vastly improve the thermal stability of these hollow structures and expand their usage for elevated temperature reactions.

My research is multifold, and has served to advance the general understanding of the following points critical to the advancement of nanotechnology: *i*) synthesis of metal-based nanocrystals with controlled shapes, sizes, and compositions; and *ii*) characterization and understanding of the behavior of these nanocrystals relative to catalytic and industrial application *via* high-resolution and atomic-resolution *in situ* microscopy techniques. The results herein contribute toward the rational design of future nanocrystals with tailored and enhanced structure-property functionality for industrial application and usage.

6.2 Future Directions

The strategies described in this dissertation seek to guide the rational design of metal-based nanocrystals as well as their evaluation for catalytic applications at elevated temperatures. Nonetheless, a number of issues remain to be investigated and optimized.

The understanding of reduction kinetics that can direct crystal growth and final morphology has advanced tremendously, leading to the design and synthesis of a myriad of well-controlled shapes for colloidal nanocrystals [1, 2]. Many of these more complex geometries require two or more syntheses to effectively generate the desired nanocrystal structures. While this has been very effective in opening a range of new morphologies for a variety of noble metals, the inclusion of multiple reactions introduces more complexities and margins for failure, as well as increasing reaction time and costs. Ideally, new methods should be developed for facile, one-pot reactions to synthesize high-index and other complex geometries. Further investigations into the kinetics that drive the nucleation and growth processes may be able to yield substantial progress in this area. For example, by leveraging kinetic controls between nucleation and growth reduction pathways, Huang and coworkers to develop a one-pot synthesis of Pd penta-twinned nanowires, rather than having to separately synthesize decahedral seeds first [3].

In situ electron microscopy has emerged as one of the most powerful tools for understanding and analyzing the behavior of nanostructured catalysts down to an atomistic

scale. However, it also suffers from multiple limitations. While *in situ* heating has allowed me to readily investigate the response of nanocatalysts to heat, the *in vacuo* environment of the microscope is not truly representative of a catalytic system, wherein the nanocrystals will undergo not only thermal stress, but chemical and atmospheric stress as well. Using ORR as an example, while my studies in Chapter 4 and 5 on both Pd@Pd core-shell nanocrystals and Pt nanocages showed that all examined structures would be stable at the temperatures used for commercial PEMFC (80 °C), studies have shown that particle deformation still occurs in test catalytic cells. To fully understand the effects of the true catalytic environment on durability would require designing an *in situ* cell that can accommodate both heating and chemical environments. Cuenya *et al* investigated the sintering behavior of Pt nanoparticles on thin SiO_2 films via TEM, but conducted experiments in the microscope under H_2 or O_2 atmospheric cells, respectively, to determine the thermal and chemical stability dependence on the gaseous atmosphere [4]. Similarly, Pan and coworkers were able to observe the precipitation-dissolution process of Rh-doped $CaTiO_3$ catalysts using in situ STEM at elevated temperatures under alternating oxidative and reducing gas environments [5]. However, such setups are still sharply limited, often using reactant concentrations and atmospheric pressures far below the amounts present in working catalytic reactors. Additionally, the effect of the electron beam (often varying from 200-300kV) on sample studies is not well quantified, and could have further impacts on the observed behavior noted in the microscope [6]. Ideally, future work would enhance the comprehensive design of such *in situ* high resolution work, moving toward systems that can directly mimic real catalytic cells while minimizing e-beam effects.

Finally, one of the greatest struggles in rationally designing new classes of nanocrystals for enhanced catalytic activity and durability is the lack of a predictive model. Currently, much of new nanocatalyst design relies on trial-and-error basis: developing a synthesis for new materials and structures, systematically testing the nanocatalysts for the desired reaction, and finally verifying energetics of the best performing samples through

extensive computational modelling. To better optimize and select nanocrystals with specific shapes, sizes, and compositions requires the development of a comprehensive theory. For example, Stamenkovic and coworkers predicted high activity of Pt_3Ni substrates for ORR catalysis in 2007, and from that Yang *et al* were able to derive corresponding Pt_3Ni nanocatalysts with tremendously improved activity compared to commercial Pt/C catalyst [7, 8]. More predictive models are needed to direct and narrow research toward the most promising candidates for catalytic application going forward.

6.3 References

[1] Gilroy, K. D.; Ruditskiy, A.; Peng, H.-C.; Qin, D.; Xia, Y. *Chem. Rev.* **2016,** *116*, 10414-10472.

[2] Xia, Y.; Gilroy, K. D.; Peng, H.-C.; Xia, X. *Angew. Chem. Int. Ed.* **2017,** *56*, 60-95.

[3] Huang, H.; Ruditskiy, A.; Choi, S.-I.; Zhang, L.; Liu, J.; Ye, Z.; Xia, Y. *ACS Appl. Mater. Interfaces*, **2017,** *9*, 31203-31212.

[4] Behafarid, F.; Pandey, S.; Diaz, R. E.; Stach, E. A.; Cuenya, B. R. *Phys. Chem. Chem. Phys.* **2014,** *16*, 18176-18184.

[5] Dai, S.; Zhang, S.; Katz, M. B.; Graham, G. W.; Pan, X. *ACS Catal.* **2017,** *7*, 1579-1582.

[6] Egerton, R. F.; Li, P.; Malac, M., Radiation damage in the TEM and SEM. *Micron* **2004,** *35* (6), 399-409.

[7] Stamenkovic, V. R.; Fowler, B.; Mun, B. S.; Wang, G.; Ross, P. N.; Lucas, C. A.; Marković, N. M. *Science* **2007,** *315*, 493-497.

[8] Chen, C.; Kang, Y.; Huo, Z.; Zhu, Z.; Huang, W.; Xin, H. L.; Snyder, J. D.; Li, D.; Herron, J. A.; Mavrikakis, M.; Chi, M.; More, K. L.; Li, Y.; Markovic, N. M.; Somorjai, G. A.; Yang, P.; Stamenkovic, V. R. *Science* **2014,** *343*, 1339-1343.